Department of Precision and Microsystems Engineering

A novel suspended microchannel resonator design with a high Qf product

D. S. van Dam

Report no : 2021.046
Coach : Dr. R. A. Norte and Dr. D. Shin
Professor : Dr. M. A. Bessa
Specialisation : Mechatronics
Type of report : Master thesis
Date : 27 July 2021

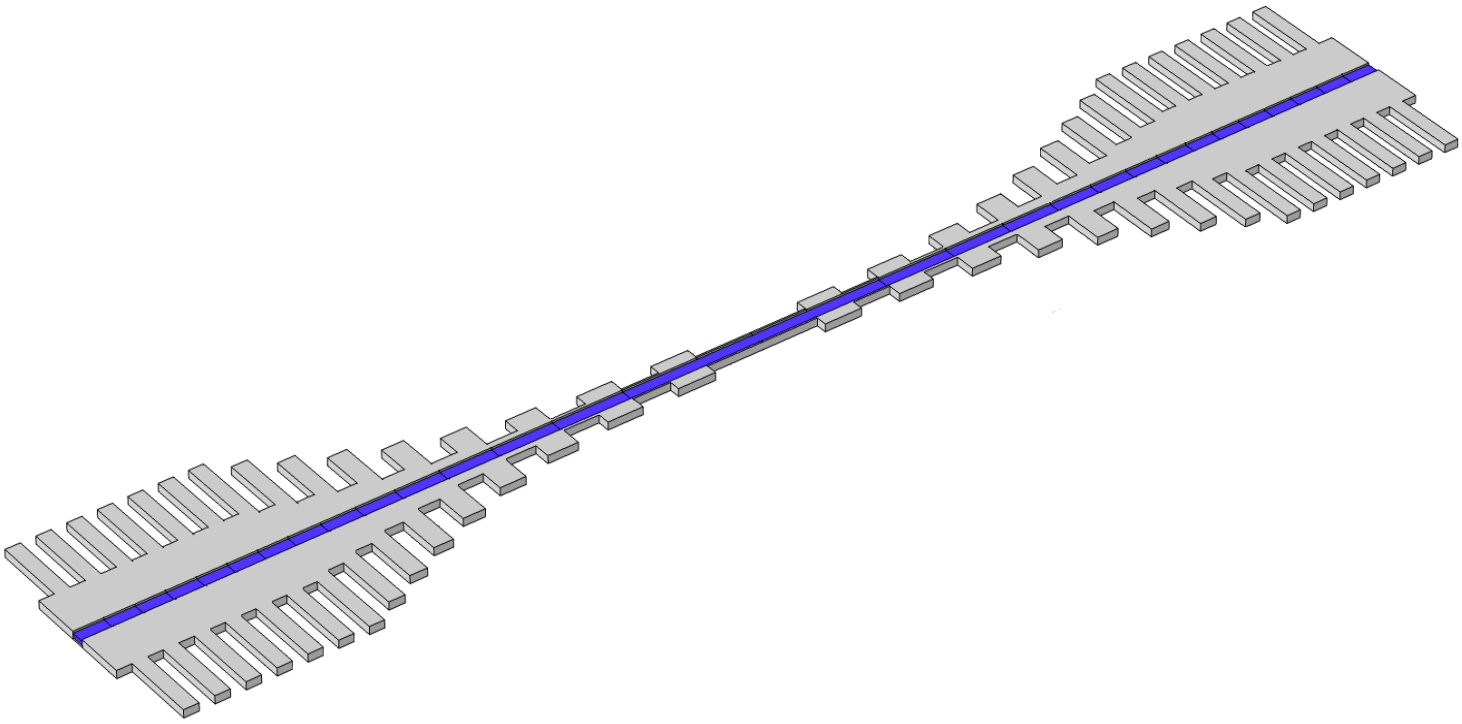

TU Delft Delft University of Technology

Challenge the future

A novel suspended microchannel resonator design with a high Qf product

by

Daniël Sebastiaan van Dam

to obtain the degree of Master of Science

at the Delft University of Technology,

to be defended publicly on Tuesday August 3, 2021 at 3:00 PM.

Student number:	4454723	
Project duration:	October 1, 2020 – August 3, 2021	
Thesis committee:	Dr. R. A. Norte,	Supervisor
	Dr. M. A. Bessa,	Supervisor and chair of the committee
	Dr. D. Shin,	Daily supervisor
	Dr. ir. W. J. Westerveld	

An electronic version of this thesis is available at http://repository.tudelft.nl/.

TU Delft

Preface

This thesis marks the final step in obtaining a Master of Science degree in mechanical engineering at the University of Technology Delft. It also marks the end as my time as a student, after studying at the university for six years. Early on during my time as a Bachelor student, I discovered that I liked CAD modeling in particular and found that I have a certain affinity for it. I still fondly remember how I was responsible for the modelling and the fluid simulation of a centrifugal pump during my first year and how we were able to fabricate it as well. I think it is then fitting to finish my formal education with modelling project as well.

The project was initially an idea by Richard Norte, who had the idea to use these nanomechanical resonators that have a very high Qf product and try to embed a microfluidic channel inside them. This with the express purpose to enable quantum mechanical experiments on biological samples. During the project it also became clear that these new suspended microchannel resonators could potentially also offer increased mass sensitivity. As such, the project has changed slightly to incorporate this as well. Although this thesis is only FEM based, I do sincerely hope that someday these designs can be realized as well. I think it would be amazing if they could be used for the purpose they were initially intended for. This preface would not be complete without thanking my two supervisors, Richard Norte and Miguel Bessa and my daily supervisor, Dongil Shin. I would like to take this opportunity to thank them for their help and invaluable advise throughout this project and for guiding it in the right direction.

Daniël Sebastiaan van Dam
Delft, July 2021

Contents

Abstract

This thesis, as part of the final step to obtain a Master of Science degree in mechanical engineering, details the Master thesis project. it introduces a new kind of suspended microchannel resonator with a very high Qf product compared to conventional designs and an order of magnitude improvement in mass sensitivity. Suspended microchannel resonators are a kind of mechanical resonator with an embedded microchannel inside. This is done as for some samples it is convenient or even necessary to put the sample into a fluid. The sample can then travel through the channel and its mass can be determined. The channel also simplifies placement of the samples compared to regular nanomechanical resonators. By having this channel embedded within the resonator, it is then possible to place the resonator as a whole in a vacuum and so eliminate medium losses. The main purpose of these suspended microchannel resonators is mass spectrometry which has already been performed on viruses and biological cells and so could potentially be very useful for the medical field as well. Especially if suspended microchannel resonators can be used to measure individual proteins which has not been done before with these resonators. It would also be interesting to use these kinds of resonators in quantum mechanical experiments. This means that the performance of these suspended microchannel resonators needs to be improved.

In order to accomplish this, a new kind of suspended microchannel resonator is introduced. The designs, and so also the master thesis project as a whole, is strictly FEM based. The new resonator design, which is a doubly clamped beam, is made from pre-stressed silicon nitride which enables high Q-factors caused by an effect known as dissipation dilution. Dissipation dilution means diluting the energy losses of the system by increasing the stored energy which is increased by the initial stress in the silicon nitride. This gives rise to the dissipation dilution factor, which is the stored energy of the system over the energy losses to the system. To increase this effect, the resonator is tapered towards the center. This is called strain engineering. Silicon nitride has been used in suspended microchannel resonators before but it did not result in higher Q-factors. This was possibly due to clamping losses. The designs presented in this thesis offer a solution to that in the form of soft-clamping. Soft-clamping consists of phononic crystals which prevent elastic waves from moving through the resonator when excited in the phononic band-gap. Vibration is therefore only possible near the center defect which is a break in the periodic structure of the phononic crystals. This reduces the curvature near the boundaries to a minimum which means that the clamping losses are also reduced or eliminated. The combined effect of these features results in very high Q-factors as has already been reported for nanomechanical resonators.

Before the designs can be simulated, the geometry of the unit cells, which are single phononic crystals, need to be determined first. This is done with the help of phononic band-gap diagrams which provide an indication as to how the model will perform. In contrast to earlier pre-stressed silicon nitride resonators, the channel also needs to be accounted for when the mechanical Q-factor is calculated. This is means that the full three dimensional stress-strain relationship will be considered whereas before one dimensional Euler-Bernoulli beam theory or two dimensional plate theory sufficed. The intrinsic Q-factor is also discussed at length which is the Q-factor inherent to the material. Multiplying this is Q-factor with the dissipation dilution factor is the definition of the mechanical Q-factor. The $Q_{surface}$, which is part of the intrinsic Q-factor is especially of concern as a new equation needs to be used to account for the channel of the resonator as under the commonly used definition the $Q_{surface}$ is dependent on the thickness of the resonator which is not the same throughout due to the channel. Finally, the fluidic loss Q-factor or Q_{fluid} is also discussed as in suspended microchannel resonators the fluid inside the channel can also cause losses to the system. An equation is found in the literature to calculate this energy loss with the help of COMSOL.

Finally, the new designs are optimized through machine learning by Bayesian optimization. There are two main models, the tapered beam model and the multi design variable model or MDV model for short. Both the tapered beam model and the MDV model have been optimized for the Qf product and the MDV model has also been optimized for the mass sensitivity. The result is that for both models the minimum Qf product necessary to perform quantum mechanical experiments at room temperature, $6 \cdot 10^{12}$ Hz is reached. When optimized for mass sensitivity, the MDV model also offers more than one order of magnitude improvement in mass sensitivity compared to the best performing suspended microchannel resonator to date. The downside is however that for the optimized models both can't be achieved at the same time. The answer to that issue could present itself in the smaller 200 nm thickness variant of the MDV model as opposed to the 1 um thickness variant considered before. The 200 nm thickness variant of the MDV model optimized for mass sensitivity then provides almost three orders of magnitude improvement in Qf product and more than 20 times improvement in mass sensitivity. The improvement in mass sensitivity means that measuring of individual proteins could possibly be achieved with these resonator designs.

Introduction

Suspended microchannel resonators (SMRs) have found great application as mass spectrometers on the micro and nanoscale. Before their introduction, nanomechanical resonators were placed in a fluid to measure a sample for which it was necessary to put them inside a fluid. This caused a lot of losses due to the fluid. Suspended microchannel resonators don't have this problem as a fluidic microchannel is embedded within the resonator which has allowed for greatly increased Q-factors and improved mass sensitivity by virtually eliminating medium losses as the resonator can now be placed in a vacuum. [44] An example of one such suspended microchannel resonator is shown in figure 1, which is the cantilever design by Manalis et al. who designed the first SMR. The channel is indicated in blue and the figure also shows how these resonators measure the mass of a sample by the frequency shift that occurs when the sample is moving through the resonator due to the mass. Suspended microchannel resonators have been used to measure nanoparticles such as exosomes with a SMR that has a mass sensitivity of less than a attogram. [37] This is the current best performing suspended microchannel resonator. They've also been used to measure bacteria, viruses and fluid density directly with the possibility of measuring quantum dots and protein strands with improved technology.[4][27] Some forms of mass spectrometry, which have already been performed with regular nanomechanical resonators, highlight the potential use of the microchannel as placement of the particle onto the resonator is difficult. This can be seen in a study which measured single proteins where the placement of the proteins is described as random in place and time as the samples are essentially dropped onto the resonator. [32] For SMRs, this problem doesn't exist as particles simply travel through the channel and particle throughput will also be a lot higher as a result.

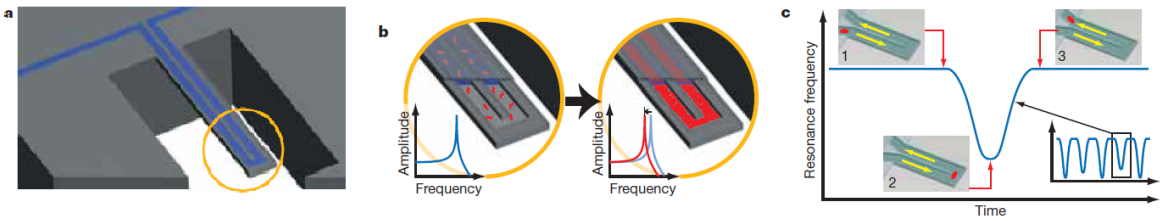

Figure 1: A figure showing the microchannel within a cantilever beam. It also shows how the frequency shifts as the sample moves through the liquid. Obtained from [44]

The potential of these devices could also have interesting applications in the medical field. They could for example perform cell counts of CD4 cells which is done to determine the progression of AIDS in a patient.[44] Another potential application is the detection of cancer cells in a patient based on the stiffness of these cells as the stiffness has shown to be considerably lower for cancer cells than for healthy cells. This has already been done with the use of atomic force microscopy.[36] Proteins are also used as biomarkers to diagnose diseases like cancer by sensing them through mass spectrometry. [40] The use of these proteins as biomarkers could allow for noninvasive detection of the disease by for example sensing the proteins in blood. SMRs could potentially simplify these processes due to the channel and make it cheaper to perform, //if// these proteins can be detected directly and individually. Furthermore, SMRs might also allow quantum mechanical experiments to be performed on biological samples at room temperature by providing a convenient container while the sample is for example placed in superposition. All of these potential applications hinge on the need to improve the performance of suspended microchannel resonators, specifically the Qf product and the mass sensitivity, far beyond what current designs allow for.

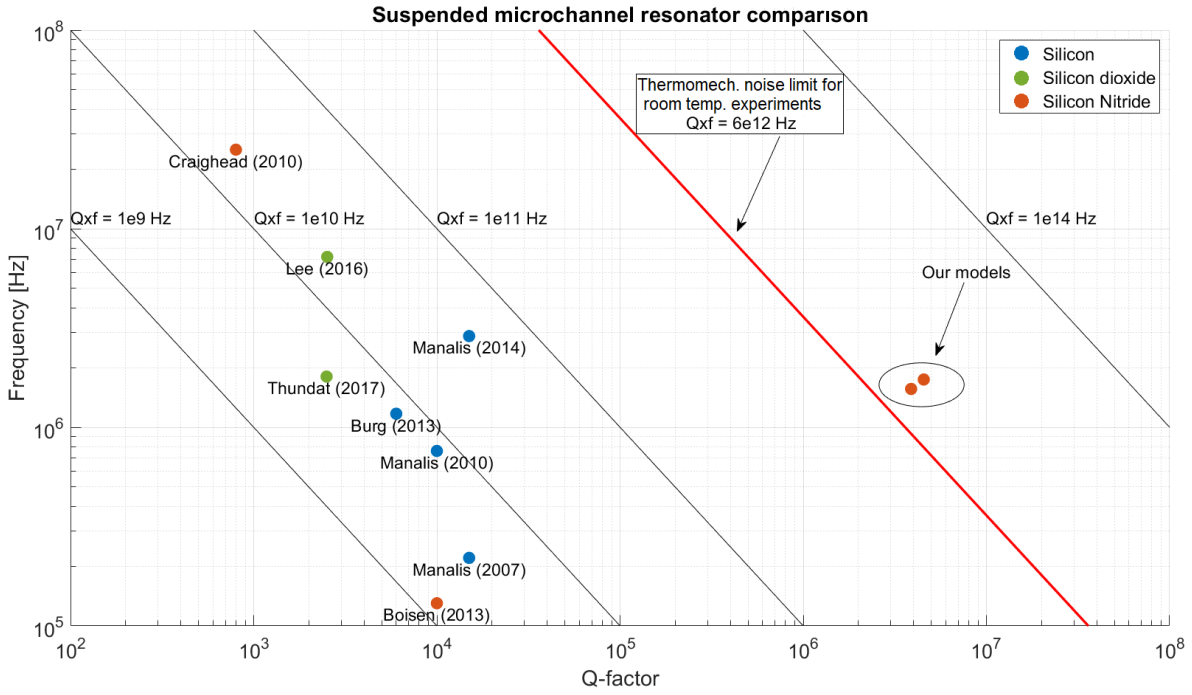

Figure 2: A figure which compares conventional SMR designs with the new designs from this thesis, optimized for the Qf product. The x-axis displays the Q-factor and the y-axis the resonance frequency. The diagonal lines indicate the Qf product with the Qf product necessary to perform quantum mechanical experiments at room temperature indicated in red. The different materials of the resonators are indicated by color. The values of the models were obtained from [4]

To enable quantum mechanics at room temperature, the Qf product, which is a measure of performance, needs to be higher than $6 \cdot 10^{12}$ Hz to decouple the resonator from the surrounding noise. [29] To date, no suspended microchannel resonator has been able to achieve this. The best performing design currently has a Qf product of about $4.3 \cdot 10^{10}$ Hz which misses the goal of reaching $6 \cdot 10^{12}$ Hz by more than two orders of magnitude. The suspended microchannel resonator designs proposed in this thesis, which are purely based on FEM analysis, aim to address that. This is best shown through figure 2 which maps the resonance frequency and the Q-factor of some current SMR designs. The diagonal lines indicate the Qf product with the Qf product required to be able to perform quantum mechanical experiments at room temperature indicated in red. As can be seen, even though conventional suspended microchannel resonators can have a wide range of frequencies, none of these resonators come close to reaching $6 \cdot 10^{12}$ Hz due to a low Q-factor which ultimately limits the Qf product. According to the literature, no suspended microchannel resonator design has been able to achieve a Q-factor of exceeding 10^5 with most designs having a Q-factor of about 10000. The designs shown in this thesis are also indicated in this graph on the right and do exceed the quantum mechanical limit. These designs have a Qf product and Q-factor of more than two orders of magnitude higher than current designs. In concrete terms, the Q-factor has been increased from about 15000 to about 4 million for both of the models shown.

In the study that measured single human Immunoglobulin M (IgM) proteins, a mass sensitivity of about 100 kDa, or 0.166 attograms ($1.66 \cdot 10^{-19}$ grams), was required to properly detect the different isoforms, or variants of the protein. [32] For comparison, the mass sensitivity of the best current SMR is about 0.3 attograms ($3 \cdot 10^{-19}$ gram) at a bandwidth of 1000 Hz. [37] In other words, an increase in mass sensitivity of about two times would already allow for these proteins to be measured individually by suspended microchannel resonators. The designs presented here go even further and provide a mass sensitivity increase of more than an order of magnitude compared to this current best performing design. This could put the mass sensitivity in the range to also measure bovine serum albumin (BSA) with a mass of about 66 KDa, or about 0.11 attograms ($1.1 \cdot 10^{-19}$ grams), as has been measured by nanomechanical resonators in a different study. [6] Another example would be that Manalis et al. per-

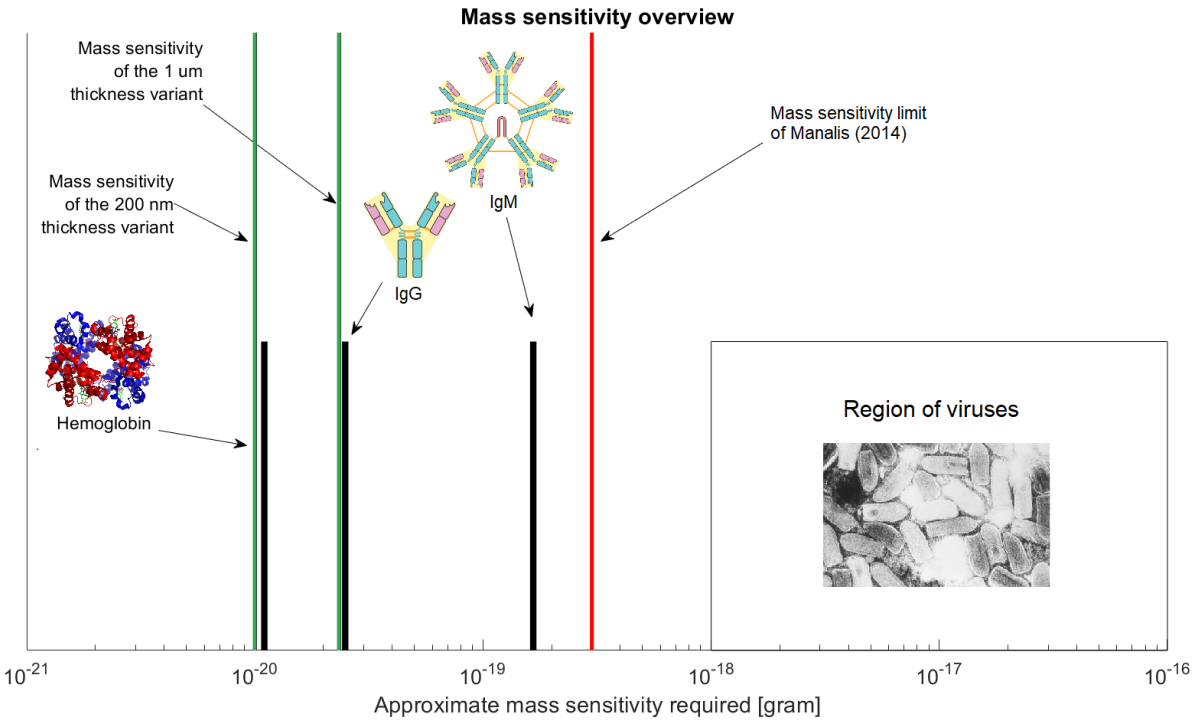

Figure 3: An overview of the current mass sensitivity limitation and the area of interest. In red, the mass sensitivity of the highest performing SMR by Manalis et al. (2014) [37]. The virus shown is called Indiana vesiculovirus and has previously been measured by [27]. In green, the mass sensitivity of the resonators presented in this thesis. As can be seen, more than an order of magnitude improvement in mass sensitivity is obtained, putting these resonators in the range to measure proteins. For the proteins shown, the assumption has been made that the mass sensitivity required is an order of magnitude lower than their actual mass. The figures of the antibodies shown are obtained from [11], the figure of hemoglobin is obtained from [14] and the figure of the viruses is obtained from [15].

formed Immunoglobulin G (IgG) mass detection by accumulation of these proteins to the surface of the microchannel. [44] This accumulation of the proteins could then be measured and so also indirectly measure the proteins themselves. The designs in this thesis could potentially do away with the surface treatments that are necessary for this detection entirely and instead measure them directly as these proteins have a mass of about 150 kDa, or about 0.249 attograms ($2.49 \cdot 10^{-19}$ grams). This is about an order of magnitude larger than the mass sensitivity of the larger micrometer thickness model which is about 25 zeptograms ($2.5 \cdot 10^{-20}$ grams) whose mass sensitivity would then be sufficient if assumed that an order of magnitude difference in mass is required to properly detect these proteins. All of this is visualized in figure 3 which provides an overview of the mass sensitivity problem. In red, the current best performing suspended microchannel resonator by Manalis et al. [37]. As can be seen, this resonator just falls short of being able to measure individual proteins while the resonators from this thesis in green do have this mass sensitivity. Likewise better mass sensitivity also means that these suspended microchannel resonators are able to measure even smaller nanoparticles. For comparison, the resonator by Manalis et al. (2014) was able to accurately measure golden nanoparticles of 10 nm. [37] With the improved mass sensitivity from the designs of this thesis, it might be possible to accurately measure single golden nanoparticles of 2.5 nm as has been done before with regular nanomechanical resonators. [6]

So how is this high performance attained? A paper by Ghadimi et al. showed nanomechanical resonator designs with a very high Q-factor and Qf product by using mechanisms called dissipation dilution, strain engineering and soft-clamping. [5] This thesis will show suspended microchannel resonators with these same mechanisms and will show how this will also lead to Q-factors on the order of a million. An example of what these SMRs look like can be seen in figure 4, with the channel indicated in blue. The length of the resonator is scaled down as in reality the resonator would be about 4 mm long with a

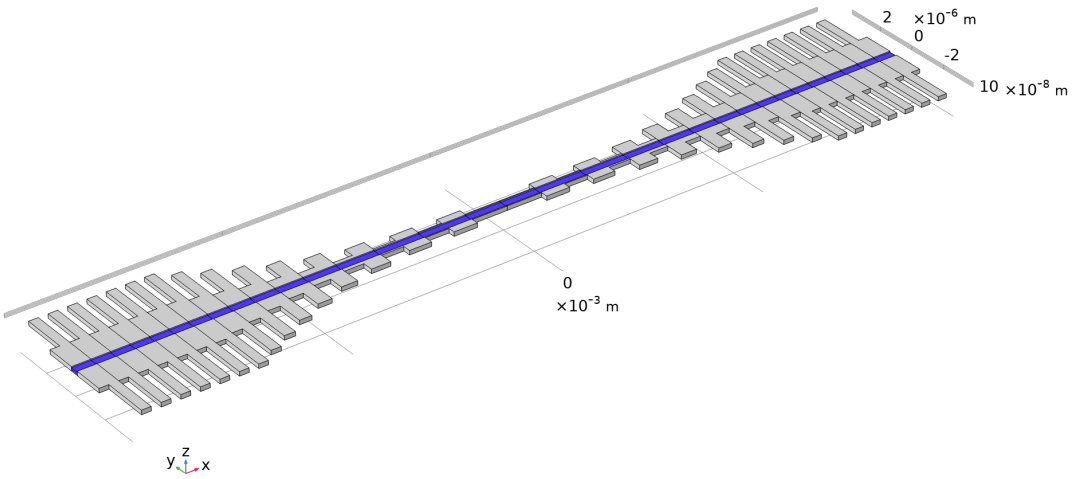

Figure 4: An example of the suspended microchannel resonator design presented in this thesis with the microchannel in blue within the doubly clamped beam. The length has been scaled down to present the resonator clearly.

maximum width of about 3.5 um in this case. Important to note is also the fact that the resonators from this thesis are made from silicon nitride instead of the more commonly used silicon or silicon dioxide as also indicated in figure 2. The silicon nitride designs are indicated in orange with the silicon and silicon dioxide designs indicated in blue and green respectively. For the designs presented here, the silicon nitride is pre-stressed which increases the stored energy of the system. This stored energy gives rise to dissipation dilution. In a word, dissipation dilution ”dilutes” the energy losses of the system by comparitively increasing the stored energy which is increased due to the internal stress of the resonator. As indicated in figure 2, other silicon nitride suspended microchannel resonators do exist, but only one is also made from high stress silicon nitride which is the design by Craighead et al. [3] The other design indicated in orange is made from low stress silicon nitride. As can be seen, the resonator by Craighead et al. has a very low Q-factor, possibly due to clamping losses in the system. For the resonator designs presented here that will not be a problem however, as these designs make use of soft-clamping which aims to minimize clamping losses. Soft-clamping is the use of phononic crystals to localize the eigenmode at the center to reduce the curvature at the boundaries which eliminates clamping losses. The phononic crystals can be seen in figure 4 as the periodic corrugated rectangles. Strain engineering is the tapering of the resonator in such a way to increase the stress at the center. The tapering is also clearly shown in figure 4. These mechanisms will be discussed later at length. It’s also important to note that the models shown in this thesis are optimized with machine learning through Bayesian optimization.

Before the resonator designs can be adequately calculated and optimized, there are a couple of points that need to be addressed first. First of all, the equation for the mechanical Q-factor needs to be derived for the three dimensional strain which hasn’t been done explicitly before in the literature. This is necessary as the embedded channel means the z-axis can’t be ignored since the thickness isn’t the same throughout the resonator and it might introduce additional effects such as non-negligible shear stress in the z direction. second, the intrinsic Q-factor or more specifically, the $Q_{surface}$ which is necessary to calculate the mechanical Q-factor. The $Q_{surface}$ in the form as it is used for silicon nitride nanomechanical resonators is dependent on the thickness of the resonator, which once again hasn’t one single value due to the channel. In order to calculate it, a paper by Yasumura et al. was used which explains the fundamental definition of the $Q_{surface}$. Third and finally, the fluid inside the channel can also cause energy dissipation which needs to be accounted for. Sader et al. investigated this Q_{fluid} in depth and their equations were used to numerically calculate it with the help of COMSOL. [19]

The core concepts that are relevant to the suspended microchannel resonators and the presented designs in particular will be discussed first in chapter one. Especially the mechanisms behind the high

Qf and Q-factor will be explained in depth. Chapter two will explain how the mechanical Q-factor and the Q_{fluid} are calculated and derived. An attempt will also be made to validate these equations either by way of existing experimental data or analytically, as experiments were not performed for this thesis project. Chapter three will explain how the COMSOL model works and how it works in conjunction with Matlab. It will also detail the optimization results of both the Qf product and the mass sensitivity. Finally, the thesis will be closed off with the conclusion and a reflection on the thesis project.

1

Theoretical Background

1.1. Nanomechanical Resonators

The Q-factor or quality factor in relation to nanomechanical resonators is a measure of energy loss in the system due to for example clamping, medium losses or in the case of suspended microchannel resonators, the fluid inside the channel can also induce losses in the system. [38][43] The Q-factor determines how accurately the resonance frequency of the system can be measured. A higher Q-factor leads to a higher resonance amplitude and a smaller width of the peak which enables the resonance frequency to be determined more accurately.[38]

The Q-factor and the resonator itself is best visualized in figure 1.1. Figure A displays a mass-spring-damper system. For example, if this system is provided with a force input, it will start to vibrate. The amount of damping then determines for the amplitude of vibration and for how long it will keep vibrating. Figure B shows the magnitude plot with the magnitude on the y-axis and the frequency on the x-axis. As can be seen, the plot with $\xi = 0.01$ has a very amplitude and so also a clearly defined peak. This indicates a high Q-factor with low damping. The other two plots have more damping and also a smaller, less defined resonance peak. The resonance frequency and the shift due to the mass of a sample can be more accurately determined when this peak is clearly defined. Generally, the Q-factor can be expressed in the form of equation 1.1 where W is the energy stored in the system and ΔW is the energy lost per cycle of vibration. [38] The Qf product, which is the product of the Q-factor and the resonance frequency is a measure of performance. For example, as has been mentioned in the introduction, it is understood that for quantum optomechanics at room temperature, a Qf product of Qf $> 6 \cdot 10^{12}$ Hz is required.[29] As one potential application of the SMR designs shown here is performing quantum mechanical experiments, this is definitely a value to keep in mind.

$$Q = 2\pi \frac{W}{\Delta W} \tag{1.1}$$

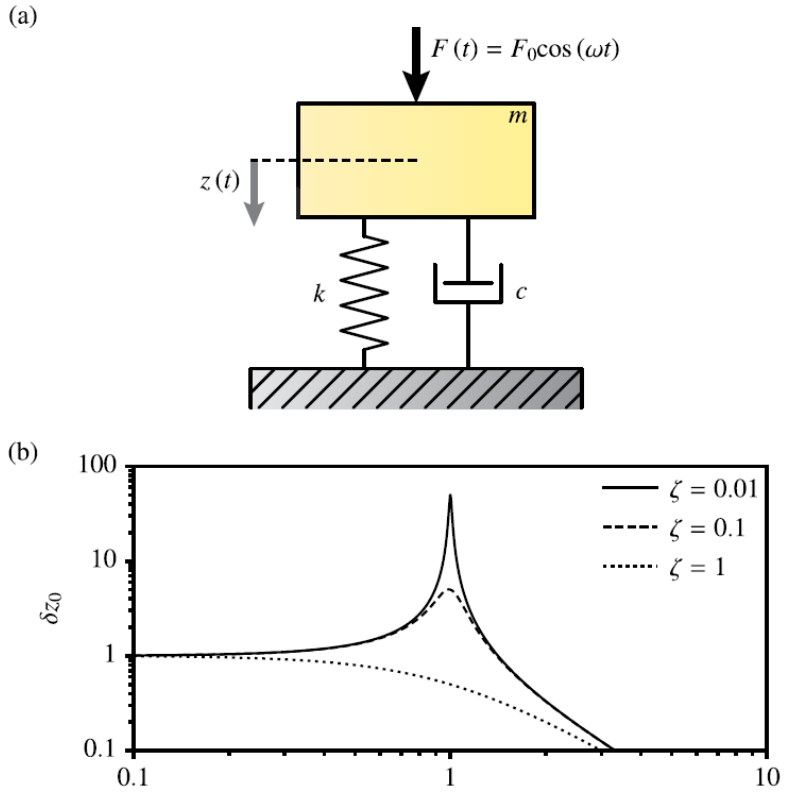

Figure 1.1: A figure which visualizes the resonator as a single mass-spring-damper system. Figure B displays various resonance peaks under the influence of different amounts of damping. This figure has been obtained from [41]

First, let's discuss how nanomechanical resonators perform mass sensing. Generally, a small mass can be measured by the degree of the displacement of the resonance frequency of the resonator which is caused by this mass. The resonance frequency of a resonator is simply a function of its mass and its stiffness. Equation 1.2 is a modification of the well-known equation obtained from [42]. Δm is the mass of the sample and α is a constant that depends on the location of the sample on the resonator. For example, in the case of microcantilevers, this value would be approximately equal to 1 if the sample is placed at the tip of the resonator. However, placement of samples can be quite difficult in the case of nanomechanical resonators. [32] This equation also implies that ideally, the mass of the resonator itself needs to be as small as possible to make sure that this frequency shift can be measured accurately. A smaller mass and in particular a smaller effective mass of the resonator would enable smaller sample masses to be detected.[4]

$$f = \frac{1}{2\pi}\sqrt{\frac{k}{m + \alpha\Delta m}} \tag{1.2}$$

Equation 1.3 is the mass sensitivity or the mass resolution of the system which is another measure to determine how small the mass of a sample can be. This equation was obtained from [24] The mass sensitivity will also be used to determine the performance of the designs considered in this thesis. The first fraction shown is the signal to noise ratio of the system measured in thermal noise. k_b is Boltzmann's constant with T as the temperature of the surroundings. The "signal" here is the maximum drive energy with ω_0 as the resonance frequency in rad/s and x_c as the RMS displacement at the center of the doubly clamped beam. Ekinci et al. determined this value to be 0.53t with t as the thickness of the resonator. [24] This is the value used for the designs of chapter 3. Δf is the chosen bandwidth of the system. If this is taken as 1, as is done in the remainder of this thesis, the mass sensitivity has the

units $\frac{g}{\sqrt{Hz}}$. Equation 1.4 is the effective mass, obtained from [8]. Here, ρ is the density of the material which multiplied by the total displacement of the resonator squared, x^2 and integrated over the entire volume of the resonator. Lastly, x_{max} is the maximum displacement of the resonator.

$$\delta m = 2m_{eff}\left(\frac{k_b T}{m_{eff}\omega_0^2 x_c^2}\right)^{0.5}\left(\frac{\Delta f}{Q\omega_0}\right)^{0.5} \tag{1.3}$$

$$m_{eff} = \frac{\int\left(\rho x^2\right)dV}{(x_{max})^2} \tag{1.4}$$

In a subset of nanomechanical resonators, high mechanical Q-factors can be achieved by inducing a high internal stress, on the order of 1 GPa, into the resonator. These resonators are usually made from silicon nitride (SiN), as silicon nitride has a yield strength of about 6 GPa. [5] This concept was first reported by Verbridge et al. They managed to create a nanomechanical resonator with a Q-factor of 207000, the highest at that time on a nanoscale. [12] The paper also beat the notion that the Q-factor decreases with smaller dimensions. The concept of inducing a high internal stress has come to be known as ”dissipation dilution”. As the high internal stress significantly increases the stored energy of the system, thereby comparatively ”diluting” the loss factors which increases the Q-factor per the definition given by equation 1.1. [45][38] Equation 1.1 can be rewritten as equation 1.5. Here, Q_0 is the intrinsic Q-factor which is the inherent material-dependent Q-factor of a resonator and the energy ratio $\frac{W}{\Delta W}$ is also known as the dissipation dilution factor. It should be noted that the mechanical Q-factor is equal to the intrinsic Q-factor in the case when the resonator is not pre-stressed. [38] In this case, the stored energy is roughly equal to the energy losses and the dissipation dilution factor is unity.

$$Q_{mechanical} = 2\pi Q_0 \frac{W}{\Delta W} \tag{1.5}$$

As mentioned in the introduction, the main inspiration for the designs discussed in this thesis is the paper by Ghadimi et al. [5] The most notable result from this paper specifically is the discovery that the combination of soft-clamping and strain engineering results in a dramatically increased Q-factor and Qf product.[5] This in combination with the already established dissipation dilution. One of the goals of Ghadimi et al. was to exploit dissipation dilution with the use of strain engineering to get the internal stress close to the yield stress of the material to obtain as high a Q-factor as possible. [5] Strain engineering here implies tapering the beam toward the center to locally increase the internal stress which increases the dissipation dilution effect. Soft clamping in the case of Ghadimi et al., consists of using phononic crystals which consists of a periodic structure with a defect at the center of the beam. The phononic crystals here take the shape corrugating beams. In other words, the resonator has a periodic varying width. This periodicity is a central concept of phononic crystals, which will be discussed at length later. Figure 1.2.A shows a schematic drawing of the resonator by Ghadimi et al. In it, the phononic crystals can be seen clearly as well as the tapering of the resonator. It also shows the localization of the mode shape at the center and the localization of stress as a result of the tapering. This is only one way of using phononic crystals in nanomechanical resonators. For example, Tsuturyan et al. have used phononic crystals in their design to create a lattice structure.[45] A picture of this can be seen in figure 1.2.B. It also shows the localization of the mode shape of the resonator which is indicated in yellow. For the darker parts of the resonator indicate a damped out modeshape. Phononic crystals are used in nanomechanical resonators with the intent to decrease or eliminate clamping losses.

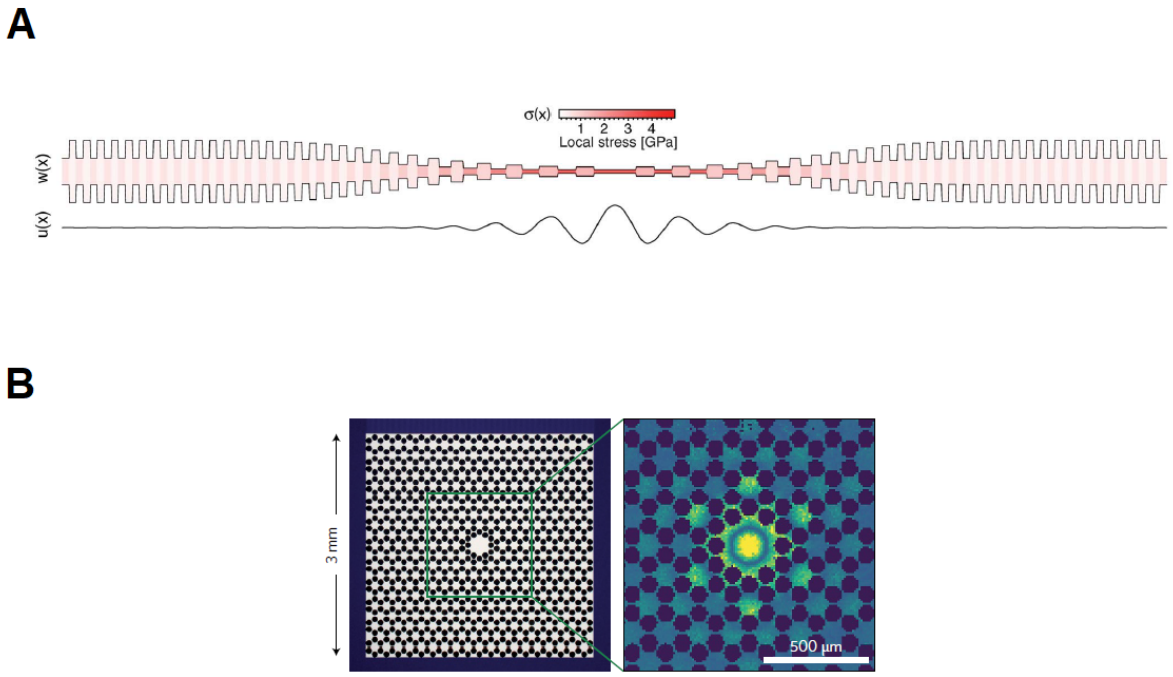

Figure 1.2: In figure A, the doubly clamped beam resonator design by Ghadimi et al. As obtained from [5]. In figure B, a resonator by Tsaturyan et al. with the lattice design. As obtained from [45].

Earlier papers reported that clamping losses caused by strain are a significant factor which is limiting the Q-factor in those cases.[39][34] Tsaturyan et al. were the first to combine dissipation dilution and soft clamping. Doing so resulted in Q-factors in excess of 10^8 and the highest Qf product at that time, more than 10^{14} Hz.[45] The phononic crystals used in the devices designed by Tsaturyan et al. and Ghadimi et al. cause the mode shape at resonance frequency to be localized at the center. In both instances there is a defect or error in the periodic structure of the phononic crystals. By constraining the modeshape at the center away from the boundaries reduces the curvature at the clamps that would otherwise be significant.[45][5] This reduced curvature means that clamping losses are reduced or even eliminated entirely as well, enabling the possibility to reach higher Q-factors. An example of what a localized eigenmode inside the phononic band-gap could look like is shown in figure 1.3. As can be seen in the figure, the mode shape is localized at the center and gradually damps out until it disappears near the boundaries where the resonator is connected to the substrate. This means that the curvature near the boundaries is likewise also very small or even negligible which results in the elimination or minimalization of the clamping losses. This is soft-clamping.

The use of strain engineering by Ghadimi et al. in their designs meant that the internal stress at the center of the resonator was about 3.8 GPa compared to the uniform internal stress of 1.27 GPa present in the device by Tsaturyan et al.[5][45] Figure 1.2.A shows the increased stress at the center compared to the lower stress near the boundaries of the device. The use of strain engineering meant Ghadimi et al. were able to achieve Q-factors of $800 \cdot 10^6$ and Qf products exceeding 10^{15}. Figure 1.4 shows how dissipation dilution, soft-clamping and strain engineering impact the Q-factor of the resonator designs by Ghadimi et al. At the bottom in gray is the intrinsic Q-factor of the resonator. Dissipation dilution, here indicated in green has the strongest effect on the Q-factor. Soft-clamping in blue, eliminates the clamping losses, pushing the Q-factor even higher. Finally, in red, the resonator is tapered towards the center, known as strain engineering which increases the stress at the center and thereby also increasing the effect of dissipation dilution.

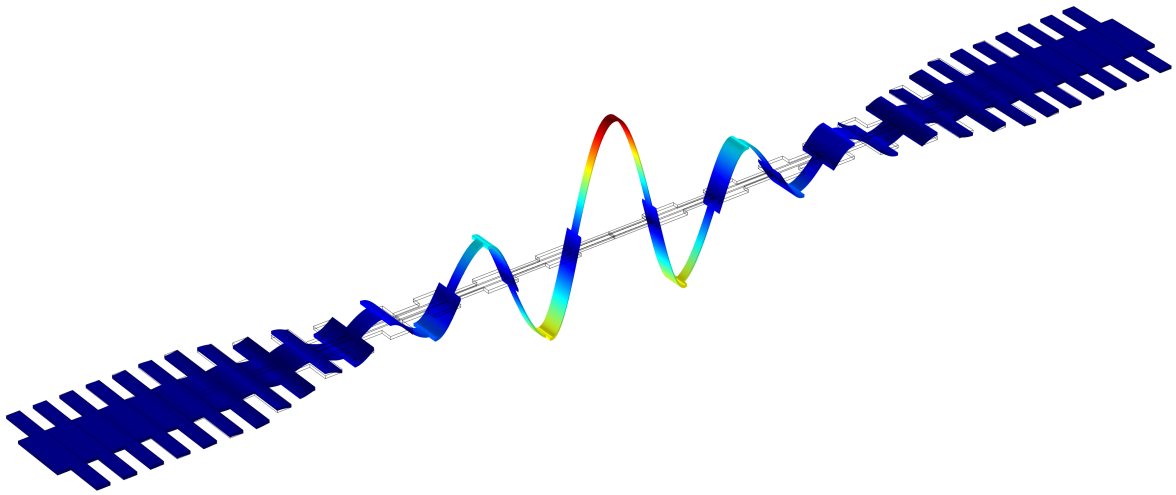

Figure 1.3: An example of what the eigenmode in the phononic bandgap can look like. This specific example is of the tapered beam design. The length is scaled down to provide this view. As can be seen, the modeshape is constrained at the center of the resonator and completely damped out near the boundaries.

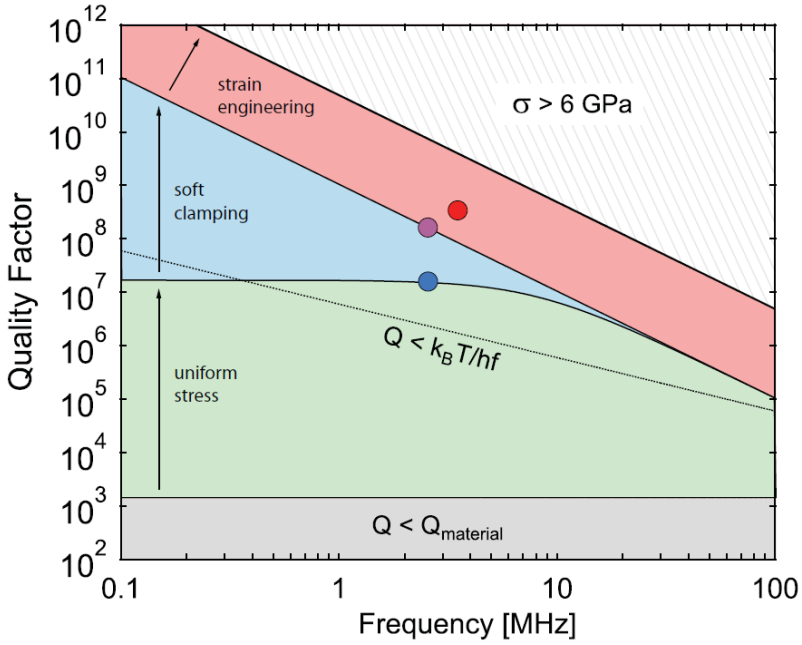

Figure 1.4: A figure showing what the combined effect of dissipation dilution, soft-clamping and strain engineering has on the Q-factor of the resonator designs by Ghadimi et al. This figure was obtained from [5]

1.2. Suspended Microchannel Resonators

One of the primary uses of nanomechanical resonators is mass detection.[5][45] However, for the use in the life sciences the sample often needs to be suspended in a liquid. Of course, this can also be done for nanoparticles of non-biological origin.[37] Before the invention of suspended microchannel resonators, one way of doing this is to simply put the entire device in a liquid. This causes very high damping losses due to the liquid as energy from the resonator is lost to the surrounding medium due to viscous losses.[38] It should be noted that generally nanomechanical resonators operate in a vacuum to ensure that medium losses are negligible. A review of cantilever sensors showed that the Q-factor of these devices in liquid is generally on the order 10^1 with limited exceptions regardless of size.[10]

Another study tested their four nanocantilevers in both vacuum and atmospheric pressures and noted a considerable degradation of the Q-factor.[30] For example, one device has a Q-factor of 500 in vacuum but only 15 at atmospheric pressure. A second, much smaller device degrades from 900 in vacuum to 500 at atmospheric pressure. As is stated in the study, size plays a significant role for air damping of these devices.[30] Naturally, this would also be the case for liquids but to an even larger extend due to the higher viscosity of liquids compared to air.

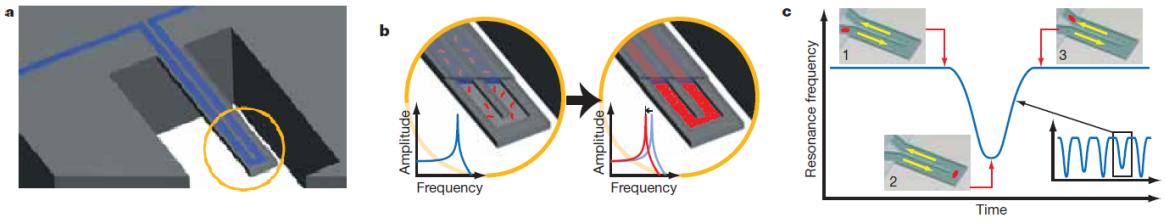

Figure 1.5: A figure showing the microchannel within a cantilever beam. It also shows how the frequency shifts as the sample moves through the liquid. Obtained from [44]

The problem of having a low Q-factor is solved by suspended microchannel resonators which embed a fluidic channel into the resonator and places the device itself in a vacuum. This completely eliminates medium losses as is the case with other nanomechanical resonators placed in a vacuum. First pioneered by the Manalis research group in 2003 and later improved upon in 2007, this device enabled mass detection of nanoparticles and bacteria which was impossible for liquid-suspended cantilevers due to the limitation of the Q-factor.[44] For mass sensing, SMRs function generally in the same way as regular nanomechanical resonators, which means that the sample mass can be derived from the displacement in resonance frequency according to equation 1.2. Figure 1.5 shows how this works in suspended microchannel resonators. The samples travel through the channel, slowly lowering the resonance frequency of the device as a result of the additional mass. When it reaches the tip, the displacement will be at its largest. Afterwards the resonance frequency returns to normal again as the sample leaves the cantilever. This is the main method of mass detection in suspended microchannel resonators. This same method of mass detection can also be used to determine the stiffness of the sample. Another application of SMRs is protein and concentration detection. Protein detection can't be performed directly with conventional suspended microchannel resonators however, which means that this can be done by coating the inside of the channel with a particular antibody to which the analyte will bind.[4] As a result of the analyte, the mass of the device will increase and once again the resonance frequency will also shift. Manalis et al. (2007) displayed exactly this by binding goat anti-mouse immunoglobulin-γ molecules to anti-goat immunoglobulin-γ antibodies.[44] The result was that the mass of the layers could be determined based on the shift in resonance frequency. As has been implied, this method of detection requires extensive chemical treatments to clean and prepare the device for the detection of the samples.[44][4] This is not necessary for mass detection of particles, as they travel in and out of the channel on their own. Improved mass sensitivity could also solve the problem of extensive cleaning procedures by being able to measure said samples directly.

SMRs offer multiple benefits and potential benefits compared to regular nanoresonators and other devices that are currently used for the same applications. Flow-through mass detection has the benefit that the SMR doesn't need to be cleaned between uses, which is not the case for competing devices. Mass resolution and mass per area resolution are also superior.[44] Generally speaking, to be able to detect certain cells, they might need to be "amplified", which means that more material needs to be generated, and they might need to be labeled as well.[23] As was the case for example during the research performed by Cross et al.[36] This requires a lot of time and needs costly materials. SMRs can potentially approve upon this with the kind of label-free testing performed by Zhang et al.[23]

Group	Geometry	Material	Dimensions (l x w x t) [um]	Frequency [MHz]	Q-factor [-]	Mass sens. $[\frac{ag}{\sqrt{Hz}}]$
Manalis (2007) [44]	Cantilever	Si	200x33x7	0.22	15000	9500
Manalis (2010) [21]	Cantilever	Si	50x10x1.3	0.76	10000	850
Manalis (2014) [37]	Cantilever	Si	27x7.5x1	1.99	15000	27
Lee (2016) [20]	CC-beam	SiO2	68x6.8x2	2.94	3130	286
Craighead (2010) [3]	CC-beam	Si3Ni4	20x2.5x0.8	25	800	4000

Table 1.1: A table with an overview of some relevant SMRs. The first three are created by the Manalis group and are all cantilever designs. The increase in mass sensitivity can be seen clearly with each new iteration. The last two are clamped-clamped beam designs with the resonator by Craighead et al. being the only known exiting design made from pre-stressed silicon nitride.

Table 1.1 notes the most prominent and highest performing SMRs to date. It only contains a small number of designs and a more complete overview can be found in the SMR review paper by De Pastina et al.[4] The general cantilever design first used by the Manalis research group in 2007 is by far the dominant design among SMR designs but a small number of clamped-clamped beam designs also exist. The best performing one is by Lee et al.[20] The paper by Lee et al. notes multiple CC-beam and cantilever designs of varying dimensions but the CC-beam in table 1.1 is both the smallest CC-beam design and the best performing one. It should also be noted all of their CC-beam designs are trumped by their cantilever designs which boast Q-factors of approximately 8000 depending on the design. [20] Another resonator of interest is the design by Craighead et al. This design is one of the few ones made from silicon nitride but more importantly it is also the only pre-stressed silicon nitride resonator found in the literature with a stress of σ=1.3 MPa [3] This could imply that the Q-factor could also be higher due to dissipation dilution but this can't be seen from the experiments. The Q-factor noted in table 1.1 is that of when the channel is filled with water. The Q-factor of the resonator is about 4000 when it's empty, so there is a definite decline in Q-factor between a filled resonator and when it's empty that's not generally seen in the designs by Manalis et al. [43][21][37] The low Q-factor could also imply that it's limited by a different loss factor than the intrinsic Q-factor, for example by clamping losses. The pre-stressed nature of the resonator has increased the resonance frequency as it is about an order of magnitude higher than comparable designs of similar dimensions.

The cantilever designs by Manalis et al. remain the highest performing ones to date with the design from 2014 having single attogram precision when measuring gold nanoparticles of 10 nm in diameter.[37] This same design also boasts a throughput of 18000 particles per hour, a record at that time. Another more recent study looked into increasing particle throughput by using deconvolution and by using SMRs in parallel. Deconvolution in this case meant using an algorithm to extract distorted resonance peak shapes and fit them to a library of theoretical peak shapes to obtain usable data.[28] Deconvolution increased throughput 16 times which means the device has a throughput of 2000 particles per minute. Using parallel SMRs meant a 55x improvement over just using a single SMR to 6800 particles per minute.[28] The authors also note that it should be possible to use deconvolution together with using SMRs in parallel. They estimate that this could cause a 197x improvement to 24000 particles per minute. Comparing this to the study performed by Manalis et al. (2014) which already achieved a record for SMRs with 18000 particles per hour, makes it clear that the throughput concerns raised in the SMR review paper by De Pastina et al. have for all intents and purposes been negated. [4][37] These concerns were based on the limited residence time of the particles inside the channel, but deconvolution was able to decrease the minimum residence time from 49 ms to 3 ms for the device tested.[28] The authors also note that the methods that were used are equally useful regardless the size of the SMRs involved.

Suspended microchannel resonators possess yet another interesting feature. Intuitively one might expect that the fluid inside of the channel might induce energy losses in the device but studies have shown this is not necessarily the case.[43][21] In SMRs, the Q-factor of the resonator is equal to $Q^{-1} = Q_{fluid}^{-1} + Q_{intrinsic}^{-1}$ given that there are no other significant loss factors.[43] Equation 1.6 shows this Q_{fluid}. It is dependent on equation 1.7 which is a function of β, the dimensionless frequency also

known as the Reynolds's number, given in equation 1.8. These equations are obtained from [43]. The Manalis research group has shown that the relation governing energy losses due to the fluid in the SMR is dependent on the viscosity of the fluid. The interesting part about this is that that relation is non-monotonic, meaning that it will not strictly increase or strictly decrease, but instead fluctuates as a function of the viscosity of the fluid. They showed this effect by slowly adding glycerol to a solution that was initially pure water. As they added glycerol to the solution, the Q-factor initially decreased as expected but shows a surprising higher Q-factor at about 80 mPa*s which appeared for both channel heights of 3 μm and 8 μm that were used. The Q-factor of the fluid is mainly dependent on the dissipation caused by the shearing of the fluid within the channel.[21] The amount of shear is in turn dependent on the inertia of the fluid characterized by the Reynolds's number β shown in equation 1.8. Here h_c is the height of the channel, μ and ρ_{fluid} are the viscosity and the density of the fluid and ω is the radial frequency of oscillation.

$$Q_{fluid} = F(\beta)\left(\frac{\rho_{device}}{\rho_{fluid}}\right)\left(\frac{h_{device}}{h_{channel}}\right)\left(\frac{w_{device}}{w_{channel}}\right)\left(\frac{L_{device}}{h_{channel}}\right)^2 \tag{1.6}$$

$$F(\beta) = \frac{38.73}{\beta} + 0.1521\sqrt{\beta} \tag{1.7}$$

$$\beta = \left(\frac{h_c}{\sqrt{\frac{\mu}{\rho_{fluid}\omega}}}\right)^2 \tag{1.8}$$

Simply put, the energy dissipation is lower when the fluid is able to follow along with the displacement of the cantilever, which is according to the study at low levels of inertia.[43] At low inertia there are no clear boundary layers at the top and bottom walls of the channel as they overlap as a result. The energy dissipation slowly increases with increasing inertia. As expected, at high inertia, the fluid is no longer able to move with the cantilever and instead moves completely out of phase. High inertia is characterized as $\beta >> \beta_{min}$. The absolute minimum in energy dissipation is at intermediate values of inertia characterized as β_{min} in the paper by Manalis et al. (2009).[43] This minimum occurs when the boundary layers merge as a result of moving from high inertia to low inertia.[19] This is best visualized in figure 1.6. In it, the minimum energy dissipation does appear to be in the middle and due to the overlapping regimes, neither of the lowest points can be reached. The point where the regimes cross is also when the Q-factor itself is the highest. Furthermore, this finding and equation 1.6, imply that the Q-factor could increase when the device is miniaturized as β decreases with decreasing channel height.[43][19] In reality this has meant that instead of the Q-factor decreasing upon miniaturization, it would not decrease and remain consistent with the Q-factors of previous devices. The Q-factor of nanomechanical resonators tends to decrease when a resonator is miniaturized.[12] The total Q-factor of a suspended microchannel resonator then is limited by the $Q_{intrinsic}$ as the Q_{fluid} is orders of magnitude higher than the $Q_{intrinsic}$, at least in the case for the Manalis resonator designs. What that means for the designs presented in this thesis, is that increasing the $Q_{mechanical}$ which is the $Q_{intrinsic}$ times the dissipation dilution factor, will increase the total Q-factor considerably. Table 1 also shows how the Q-factor has remained remarkably consistent over the years and instead improved performance relies on decreases in mass and an increase in resonance frequency as a result of miniaturization. As can be seen, the mass sensitivity of the Manalis designs improve as well. Equation 1.3 has shown that, as the mass sensitivity scales with Qf^2, the mass sensitivity increases a lot with a constant Q-factor and increasing resonance frequency.

What this finding means for fluid inside the channel is that the Q-factor of the SMRs are either similar or show a small improvement when comparing the same device when it is empty or when it is filled with water. This is also shown by Lee et al. [21] They filled their device with either water, ethanol

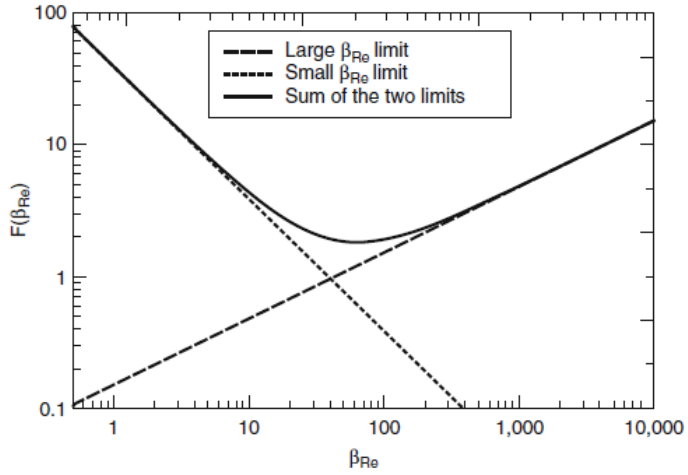

Figure 1.6: Plot showing the dimensionless function vs. dimensionless frequency. The minimum indicates the point of lowest energy dissipation. From [38]

or D_2O and while the device filled with water had a slightly higher Q-factor compared to the empty channel, the ones filled with ethanol and D_2O had lower Q-factors. This despite the fact that ethanol has a lower viscosity than water but D_2O has a higher viscosity. The resonance frequency does show a more predictable result as they showed that it has a linear dependence on the density of the fluid and so also its combined mass.[21] The combined implication of these findings are that miniaturization is possible and that the Q-factor does not necessarily degrade based on the miniaturization itself. Instead, performance is likely to increase as the resonance frequency increases and the mass of the SMR will decrease which means a higher mass sensitivity. It also conveniently means that Q-factor calculations of empty SMRs are highly indicative of what the actual Q-factor will be when the device is filled with water as the total Q-factor of the resonator is ultimately limited by the $Q_{intrinsic}$.

1.3. Phononic Crystals

As has been mentioned in section 1.1, phononic crystals have recently found their way into nanomechanical resonators with the express purpose of decreasing clamping losses of the resonator and to increase the quality factor as a result.[5][45] Phononic crystals are structures with a certain periodicity.[31] This periodicity can either be a repeating pattern as is the case with the resonator designs of Ghadimi et al. with the rectangular corrugated beams or Tsaturyan et al. which display a repeating pattern of missing circular holes. Both of these resonators can be seen in figure 1.2.A and figure 1.2.B, respectively. The phononic crystals can also be a periodic pattern of interchanging materials with different densities. Even though phononic crystals in these cases are on a microscopic scale, they are not limited to it. On a macroscopic scale, phononic crystals could for example improve acoustics and on nanoscopic scales it is possible to control heat flow through a material.[31] Furthermore, phononic crystals exist as 1D, 2D and 3D variations. This is visualized in figure 1.7. For example, the resonator by Ghadimi et al. uses 1D crystals and the resonator by Tsaturyan et al. uses 2D crystals. The logic behind it is as simple as in that the structure of the device by Ghadimi et al. only varies in one axis, this being the x-axis, and the structure of the device by Tsaturyan varies in two axes, both x and y. A 3D crystal would then also need to vary in the z-axis.

Central to the idea of phononic crystals is the phononic band-gap. The phononic band-gap is a range of frequencies at which waves can't propagate through the material.[31] The phononic band-gap can be visualized in a band-gap diagram in which the eigenfrequencies are mapped against the wavenumber vector. An example of this is shown in figure 1.8. The phononic band-gap is indicated in gray. The band-gap is enclosed by two pairs of eigenmodes as indicated. In order to facilitate vibration at resonance frequency that is necessary for mass sensing and other applications, a central defect to the periodic

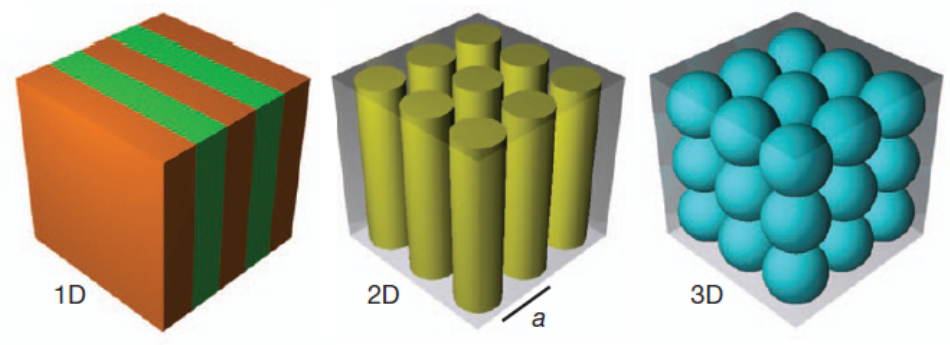

Figure 1.7: A figure that visualizes the different phononic crystal variations. Obtained from [31]

phononic crystal structure has been employed. The central defect allows for a break in the periodic structure and so allows vibrations locally at the defect. Both the resonator designs of Tsaturyan et al. and Ghadimi et al. have such a defect. As has been mentioned before, the defect allows the resonator to vibrate while actuated in the phononic band-gap near to defect as can be seen in figure 1.3. The resonance frequency of the defect mode can be changed by modifying the length of the defect.[5][13] For example, the study by Ghadimi et al. found that the defect mode with the highest Q-factor was located in the middle of the band-gap which was found by experimentally varying the defect length.[5]

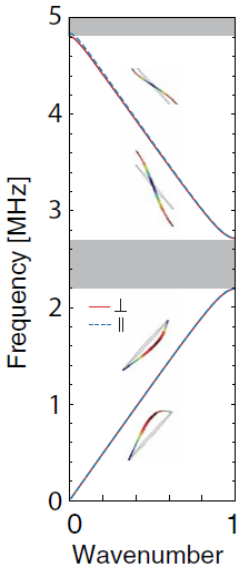

Figure 1.8: A figure of a phononic band-gap diagram. Obtained from [5]

The band-gap width also plays a role here. A wider band-gap could make it easier to place the defect mode within the band-gap without having the risk that when mass is added to the resonator due to a sample, that that additional mass displaces the frequency such that it will no longer be located in the band-gap.[13] The same study also found that the band-gap can be widened by increasing the mass contrast of the phononic crystal. In context of the resonator by Ghadimi et al. this could for example mean making the sides longer. The study also found that this would also increase localization of the defect mode.[13] The drawback of doing this is that it might increase internal losses in the system. They note that the trade-off might be worth it depending on the circumstances and whether or not the device is used at cryogenic temperatures or not.[13] One last thing that might also be of interest is that the high mass contrast devices that were tested also had a lower effective mass compared to their low contrast counter parts. This could mean that these high contrast devices might have a better mass sensitivity than the lower contrast ones according to equation 1.3.

1.4. Bayesian Optimization

As has been mentioned before, for the optimization of the resonator designs Bayesian optimization is used. Bayesian optimization is generally used to find either a global maximum or minimum of a specific function. [18] Specifically, a variant called GpyOpt. [7] Bayesian optimization optimizes in the case of the models presented in this thesis a desired variable by way of a Gaussian process. [9] The Gaussian process forms a probability distribution which is used to estimate the desired output value which is either the maximum or minimum of the objective function which is dependent on the design space. [9] The design space consists of the variables of the objective function. This is shown in equation 1.9 where f is the unknown objective function, $\mathbf{x}$ are the design variables and $\mathbf{x}^*$ are the optimized design variables as a result of the optimization. Before the optimization itself starts, the algorithm needs a number of data points to fill the design space and to create the so-called Gaussian prior distribution. [35] Here, these initial points are picked randomly as the objective function is unknown. After the initial points are determined, the algorithm can start with the data collection which is the determination of new iterations. These new data points are used to update the prior distribution to form the posterior probability distribution. [35] The difference between the prior and the posterior distribution is that the posterior depends on new data obtained by the algorithm and is generally updated each iteration. [9] With the obtained data and the posterior probability distribution, it can then create an acquisition function which determines the specific values of the design variables for the next iteration. There are a number of acquisition functions used for Bayesian optimization but the most commonly used one is the expected improvement or EI. [9] In the case of the EI acquisition function, it estimates where the biggest improvement over the current best result is located based on the known points acquired during previous iterations and the posterior. [22]

$$\mathbf{x}^* = \arg\max f(\mathbf{x}) \tag{1.9}$$

This is also visualized in figure 1.9. In it, three iterations of the Bayesian optimization are shown with the posterior probability field indicated in blue and the acquisition function indicated in green. As can be seen, the posterior decreases near newly assigned data points as the certainty is higher near these points. After calculating the new iteration and acquiring the output, the algorithm will then update both the posterior and the acquisition function with this new data point and repeat this process. The way EI works also implies that the acquisition algorithm prioritizes where it estimates where the biggest improvement can be found. This means that it could prioritize global solutions instead of local solutions. Bayesian optimization has also been shown to outperform other global optimization algorithms. [22]

The above explanation is how the Bayesian optimization is used in this paper, and it is also somewhat simplified, but there are other ways of dealing with the algorithm. For example, after as the cost of updating the GP scales cubically with the number of iterations, updating it becomes more computationally expansive. [9] Although it has been reported that iterations on the order of a couple of thousands should be attainable for desktop computers. [35] Computational complexity could for example be reduced by simplifying the GP by using approximations of the exact GP. This can reduce the complexity and so also the computation time considerably but it does introduce noise as a side effect of the approximation. [9] Alternatively, iterations could for example also be calculated in parallel instead of sequentially which is how Bayesian optimization typically works. [9] This could reduce computation time even if the number of iterations necessary does not change. In the case of FEM calculations this might be difficult to realize as the computation time of a single simulation could change significantly based on the design variables. It could create situations which require the Bayesian optimization to wait for long running simulations before it can recalculate the posterior and determine new points of interest. It should also be noted that using Bayesian optimization with a lot of parameters can be computationally expensive as the number of iterations required to define the design space properly scales exponentially with these parameters. [9] It has been reported that Bayesian optimization works well for problems with fewer than 20 parameters. [18]

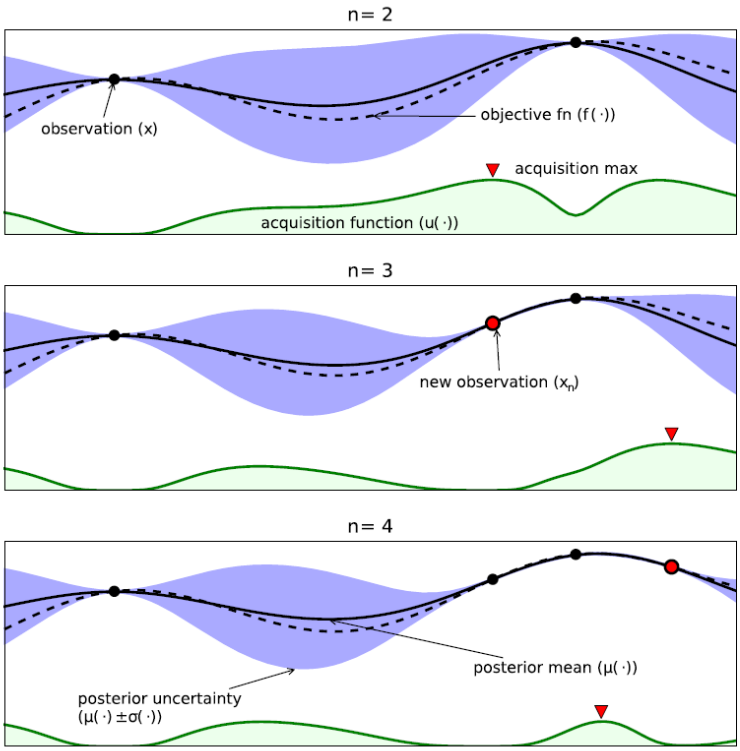

Figure 1.9: A figure that displays how the Bayesian optimization algorithm works. Obtained from [9]

2

Q-factor Calculations

Before the resonator designs themselves can be discussed, the mechanical Q-factor calculations need to be explained first. In the paper by Ghadimi et al., on which the general design of the resonators is based, they show the mechanical Q-factor calculations using 1D Euler-Bernoulli beam theory.[5] The Euler-Bernoulli beam theory is used to simplify equations and give an intuitive understanding of what components make up a certain equation. A second paper confirms that this equation has been used for their resonator designs and notes that the equation agrees well with the full 3D case. [17] The equations that they outline take the form of equations 2.1 and 2.2 with equation 2.1 as the mechanical Q-factor, which is the intrinsic Q-factor multiplied by the dissipation dilution factor. The dissipation dilution factor is the ratio of the stored energy over the energy losses to the system. Equation 2.2 is the intrinsic Q-factor which depends on the material of the resonator and the thickness of the resonator, h. In this chapter, both the dissipation dilution factor and the intrinsic Q-factor will be discussed with regard to their application in the suspended microchannel resonator designs and how they are different compared to Q-factors used elsewhere in the literature. Secondly, in contrast to most regular nanomechanical resonators, the fluid within the resonator can also cause energy dissipation to the system and so could also decrease the total Q-factor of the system. [19] This fluid-loss Q-factor, or Q_{fluid}, will also be discussed in this chapter.

$$Q = \frac{W_{tensile}}{W_{bending}} Q_0 \tag{2.1}$$

$$Q_0 = 6900 \frac{h}{100 \cdot 10^{-9}} \tag{2.2}$$

2.1. The Dissipation Dilution Factor

Calculating the mechanical Q-factor of the suspended microchannel resonator designs is a bit more tricky than calculating the Q-factor of a regular resonator. This is because these types of resonators contain a channel inside which gives these resonators a 3-dimensional geometry. It is because of this channel that simple plate or beam theory no longer suffices because the resonator can no longer be described by the 2-dimensional plate theory equation or Euler-Bernoulli beam theory as was used by Ghadimi et al. For the sake of completeness, let's discuss plate theory further and why it is insufficient in this case. The main idea behind classical plate theory also known as Kirchhoff's plate theory, is that a plate can be described by the following points: [16]

- The plate has uniform thickness
- The thickness of the plate is very small compared to its other dimensions.
- Shear strain in the z direction is small and can be neglected as a result. Normal strain in the z direction may also be neglected.
- Stress in the z direction is very small compared to stress in the other axes and can be neglected.
- Strain is small enough that it can be assumed that the mid-plane remains unstrained.

As has been mentioned, the suspended microchannel resonator violates the first statement, as the thickness depends on location on the resonator due to the channel. It is also not immediately clear whether or not the other points would be violated. In case of the micrometer-sized design variations, which will be introduced later, the thickness is considerable when compared to the minimum width of resonator; 1000 nm in thickness vs 1500 nm in width. Even in the smaller sized tapered design we are dealing with a thickness of 200 nm and a width of 500 nm. To compare, the uniform unit cell resonator by Ghadimi et al. has a minimum width of about 500 nm with a thickness of 20 nm. [5] When these dimensions are of the same order, it could imply that shear strain might be a considerable factor as well. The resonator design are however 4 mm in length. With these points it becomes clear that classical plate theory does not suffice and that a full three-dimensional Q-factor calculation is needed.

A full three-dimensional Q-factor equation can't be readily found in the literature and so it needs to be derived. As a starting off point we take a look at the theoretical equations derived by Yu et al. who have derived a mechanical Q-factor model based on classical plate theory for their square membrane resonators. [33] This model is in turn based on the one-dimensional model developed by Unterreithmeier et al. who used them for the one-dimensional string resonators. [34] The one-dimensional model is the same one that's been mentioned earlier when referring to the paper by Ghadimi et al. [5] The model developed by Yu et al. is used here because they discuss a very general case before they apply classical plate theory.

$$Q = \frac{2\pi U}{\Delta U} = \frac{2\pi U_{kinetic}}{\Delta U} \tag{2.3}$$

We start off with equation 2.3, the definition of the Q-factor, which is also the origin of equation 2.1 [38][33] Here we chose to use the kinetic energy, shown in equation 2.4, as the stored energy of the resonator instead of the tensile energy used by Ghadimi et al. This is mainly done for the sake of ease when the stored energy is determined in COMSOL but both methods are equally valid as these types of energy convert into each other during vibration. The kinetic energy is used by Yu et al. as the stored energy as well. The energy loss to the system is shown in equation 2.5 is obtained from Yu et al. [33] The energy loss of the system is proportional to the bending energy of the system with the crucial difference that the energy loss is caused by out-of-phase stresses described by E_2, the complex component of the total Young's modulus $E = E_1 + iE_2$ with E_1 as the conventional Young's modulus. [33][34] E_2, also known as the loss modulus or dissipative Young's modulus, is just like the conventional Young's modulus material dependent and responsible for the phase delay which causes the stresses in the system to partially be out of phase with the strain in the system. The out-of-phase stresses lead to some of the stored bending energy to be irreversibly lost to heat which is the energy loss of equation 2.5. [33]

$$U_{kinetic} = \frac{1}{2}\int \left(\rho\omega^2 \left(x_{disp}\right)^2\right) dV \tag{2.4}$$

$$\Delta U = \pi \int \left(E_2 \varepsilon_0^T M \varepsilon_0\right) dV = \pi \int \left(\frac{E_2}{E_1} E_1 \varepsilon_0^T M \varepsilon_0\right) dV = \pi Q_0^{-1} \int \left(E_1 \varepsilon_0^T M \varepsilon_0\right) dV \tag{2.5}$$

$$\mathbf{M} = \frac{1}{(1+v)(1-2v)} \begin{bmatrix} 1-v & v & v & 0 & 0 & 0 \\ v & 1-v & v & 0 & 0 & 0 \\ v & v & 1-v & 0 & 0 & 0 \\ 0 & 0 & 0 & \frac{1-2v}{2} & 0 & 0 \\ 0 & 0 & 0 & 0 & \frac{1-2v}{2} & 0 \\ 0 & 0 & 0 & 0 & 0 & \frac{1-2v}{2} \end{bmatrix} \varepsilon_0 = \begin{bmatrix} \varepsilon_{xx} \\ \varepsilon_{yy} \\ \varepsilon_{zz} \\ 2\varepsilon_{yz} \\ 2\varepsilon_{xz} \\ 2\varepsilon_{xy} \end{bmatrix} = \begin{bmatrix} \frac{\delta U}{\delta x} \\ \frac{\delta V}{\delta y} \\ \frac{\delta W}{\delta z} \\ \frac{\delta V}{\delta z} + \frac{\delta W}{\delta y} \\ \frac{\delta U}{\delta z} + \frac{\delta W}{\delta x} \\ \frac{\delta U}{\delta y} + \frac{\delta V}{\delta x} \end{bmatrix} \tag{2.6}$$

The energy loss can be rewritten to account for the loss modulus so that it is included in the intrinsic Q-factor, Q_0. Here, the intrinsic Q-factor is equal to $Q_0 = E_1/E_2$ which is equal to the volumetric loss. [25]However, as will be shown later, the intrinsic Q-factor is a little bit more complicated than that for our system here as surface losses also play a significant role on the nanoscale. [38] As has been mentioned before, our system takes into account the entire three-dimensional strain, shown in equation 2.6. As can be seen, only the linear strain is considered, a simplification also made by Yu et al. and Unterreithmeier et al. [33][34]Using only the linear strain is in part necessary because it proves difficult to calculate the nonlinear strain in COMSOL when the eigenfrequency analysis is considered, as is done here. As a final remark on this equation, the placement of the Young's modulus within the integral is only done as a matter of notation and not strictly necessary as it does not depend on the volume. Equation 2.7 presents the complete derived equation of the mechanical Q-factor in short form. With the intrinsic Q-factor taken out of the denominator, the energy ratio that remains is also known as the dissipation dilution factor. As has also been explained in chapter 1, this factor would be unity in case when the resonator is not pre-stressed. In that case, the mechanical Q-factor is equal to the intrinsic Q-factor. Finally, the solution of the energy loss equation is presented in equation 2.8 which can be directly used in COMSOL.

$$Q_{mechanical} = \frac{2\pi U_{kinetic}}{\Delta U} = Q_{intrinsic} \frac{\int \left(\rho \omega^2 \left(x_{disp}\right)^2\right) dV}{\int \left(E_1 \varepsilon_0^T M \varepsilon_0\right) dV} \tag{2.7}$$

$$\int \left(E_1 \varepsilon_0^T M \varepsilon_0\right) dV = \frac{E_1}{(v+1)} \int \left(\left(\frac{1}{2}\frac{\delta U}{\delta y} + \frac{1}{2}\frac{\delta V}{\delta x}\right)^2 + \left(\frac{1}{2}\frac{\delta U}{\delta z} + \frac{1}{2}\frac{\delta W}{\delta x}\right)^2 + \left(\frac{1}{2}\frac{\delta V}{\delta z} + \frac{1}{2}\frac{\delta W}{\delta y}\right)^2 + \right.$$

$$\left. \frac{1}{(2v-1)} \left((v-1)\left(\frac{\delta V}{\delta y}^2 + \frac{\delta W}{\delta z}^2 + \frac{\delta U}{\delta x}^2\right) - 2v\left(\frac{\delta U}{\delta x}\frac{\delta V}{\delta y} + \frac{\delta V}{\delta y}\frac{\delta W}{\delta z} + \frac{\delta U}{\delta x}\frac{\delta W}{\delta z}\right)\right) dV \right. \tag{2.8}$$

2.2. The Intrinsic Q-factor

Next, the intrinsic Q-factor will be discussed. As has been mentioned before, Ghadimi et al. used equation 2.2 as the intrinsic Q-factor for their resonator design which is accurate for thicknesses smaller than 100 nm.[5] For thicknesses of that order or smaller, the volume loss can be safely neglected. [26] The resonator designs considered here can be considerably thicker than that which means a more general description needs to be used which does include the volume losses as well. This general description of the intrinsic Q-factor takes the form of equation 2.9 which also includes the Q_{volume}. This

equation is obtained from Villanueva and Schmid. [26] There is also the complication of the channel, which again means that the thickness isn't the same throughout the resonator and that it might not be accurate to use this formulation of the $Q_{surface}$.

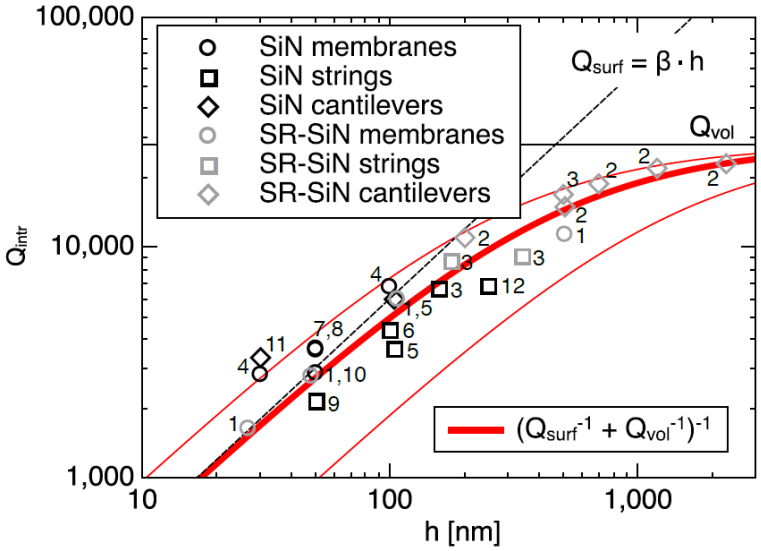

Figure 2.1: A figure that visualizes the Intrinsic Q-factor of SiN resonators. Obtained from Villanueva and Schmid. [26]

$$Q_{intrinsic} = \left(\frac{1}{Q_{surface}} + \frac{1}{Q_{volume}}\right)^{-1} \approx \left(\frac{1}{6E10h} + \frac{1}{28000}\right)^{-1} \tag{2.9}$$

First, volume loss needs to be discussed. Volume loss or bulk loss, is what limits the intrinsic Q-factor when the surface to volume ratio is reduced.[26] In other words, when the volume of the resonator is considerable compared to the surface. The relationship between the surface loss and volume loss is shown in figure 2.1 and by way of equation 2.9. The two separate loss factors are inversely added to each other which forms the complete intrinsic Q-factor as described by Villanueva and Schmid.[26] The figure was created by fitting the intrinsic Q-factors of different SiN resonators obtained from the literature. As can be seen from figure 2.1, and what was earlier implied, is that the volume loss dominates for larger values of the thickness of the resonator, while the surface loss dominates below thicknesses of about 200 nm. The surface loss in this equation is essentially the same as the one used by Ghadimi et al. shown in equation 2.2, but the inclusion of the volume loss allows for a more accurate calculation of the intrinsic Q-factor for larger thicknesses. As has been mentioned before, the intrinsic Q-factor is material dependent and so the values shown in equation 2.9 are only valid for silicon nitride structures.[26]

As the surface loss shown in equation 2.9 is thickness dependent, we are left with a similar issue as was presented for the dissipation dilution factor: the thickness isn't the same throughout the resonator due to the channel. One way of solving this could be to cut up the energy loss and the accompanying intrinsic Q-factor such that for each section the thickness is the same, which was what was done in an earlier version of the mechanical Q-factor calculation, but a more generalized and elegant solution is preferred. The solution presents itself through a paper by Yasumura et al. [25] They describe the volume loss as $Q_{volume} = E_1/E_2$, showing its material dependence in mathematical form, as the two components of the Young's modulus are material dependent, and the surface loss which they describe as being caused by a thin layer of contaminates or impurities, similarly how it is described by Villanueva and Schmid. [25] [26] Furthermore, they provide a more rigorous mathematical formulation described in equation 2.10, which has been adapted to present it in a complete form. The volume loss is described in a similar way, but with the energy losses taken over the volume instead. This leads to the case where the strain can be taken out of the equation which leads to the equation $Q_{volume} = E_1/E_2$.

$$Q_{surface} = \frac{2\pi W_{bending}}{\Delta W_{surface}} = \frac{2\pi \frac{1}{2} \int \left(E_1 \varepsilon_0^T M \varepsilon_0\right) dV}{\pi \int \left(E_2^s \varepsilon_0^T M \varepsilon_0\right) dV} \tag{2.10}$$

Equation 2.10 is what could lead to the more familiar description of the surface loss found in equation 2.9 which once again shows that the $Q_{surface}$ is thickness dependent, with the assumption that the width greatly exceeds the thickness of the resonator. [25] This isn't necessarily the case for the designs presented here due to the inclusion of the channel. Solving equation 2.10 is straightforward as the groundwork already exists in the form of the Mechanical Q-factor presented in section 2.1. Once again, the equation in Yasumura et al. was solved with the use of Euler-Bernoulli beam theory but here the entire three-dimensional strain will be considered to account for the channel. Equation 2.10 introduces a new E_2^s which, together with the integral of $\Delta W_{surface}$, is applicable to the surface only. This leads equation 2.10 to be rewritten as equation 2.12, that introduces δ, which is a variable that symbolizes a thin layer on the surface of the resonator. As a consequence, the volume integral is replaced by a surface integral, taken over the exposed boundaries of the resonator.

$$Q_{surface} = \frac{tE_1}{6\delta E_2^s} \tag{2.11}$$

$$Q_{surface} = \frac{2\pi \frac{1}{2} \int \left(E_1 \varepsilon_0^T M \varepsilon_0\right) dV}{\pi \int \left(E_2^s \varepsilon_0^T M \varepsilon_0\right) dV} = \frac{E_1 \int \left(\varepsilon_0^T M \varepsilon_0\right) dV}{\delta E_2^s \int \left(\varepsilon_0^T M \varepsilon_0\right) dS} \tag{2.12}$$

$$Q_{surface} = \frac{E_1 \int \left(\varepsilon_0^T M \varepsilon_0\right) dV}{\delta E_2^s \int \left(\varepsilon_0^T M \varepsilon_0\right) dS} = \frac{250E9 \int \left(\varepsilon_0^T M \varepsilon_0\right) dV}{0.69444 \int \left(\varepsilon_0^T M \varepsilon_0\right) dS} \tag{2.13}$$

Finally, equation 2.12 has two unknown variables that need to be solved in order to make the equation usable in COMSOL. These variables are δ and E_2^s which can be found with the help of the paper by Villanueva and Schmid. As has been mentioned before, Villanueva and Schmid created an experimentally retrieved equation for the $Q_{surface}$ which is $Q_{surface} = 6E10t$.[26] This equation can be equated to equation 2.11 obtained from the paper by Yasumura et al. to get $6E10t = \frac{tE_1}{6\delta E_2^s}$. Solving this equation leads to $\delta E_2^s \approx 0.69444$ which is substituted in equation 2.12 to result in equation 2.13. There is some nuance to use equation 2.13 in COMSOL. Due to how COMSOL calculates displacement of eigenmodes, it has proven to be necessary to select surfaces based on their orientation instead of just simply selecting every surface in order to get accurate results. This means that, as most surfaces on the resonator model are aligned to a specific axis, only strains applicable to that axis are calculated instead of the complete three-dimensional strain. Realistically, strain that isn't applicable to a certain surface should be zero but this isn't necessarily the case in COMSOL. This is why it proved to be necessary to specify the surface and the applicable strain for that surface. Unfortunately, it has also proven to be very cumbersome to do this automatically for each exposed surface due to how geometry changes during the optimization. That's why it has been decided to only consider surfaces in the XY-plane which according to limited tests should account for about 90-95% of all energy losses at the surface. These surfaces, which are basically the top and bottom of the resonator and those of the channel itself, as shown in figure 2.2, can be easily selected by using a box selection in COMSOL. Also, given that the equation has a very general form, it should also be mentioned that it is possible for the channel to take on any shape if so desired. How COMSOL reacts to for example a circular channel with regard to strain isn't entirely clear however, but it seems likely that as long as the strains that are being calculated do in fact also exist, there shouldn't be a problem with regard to errors.

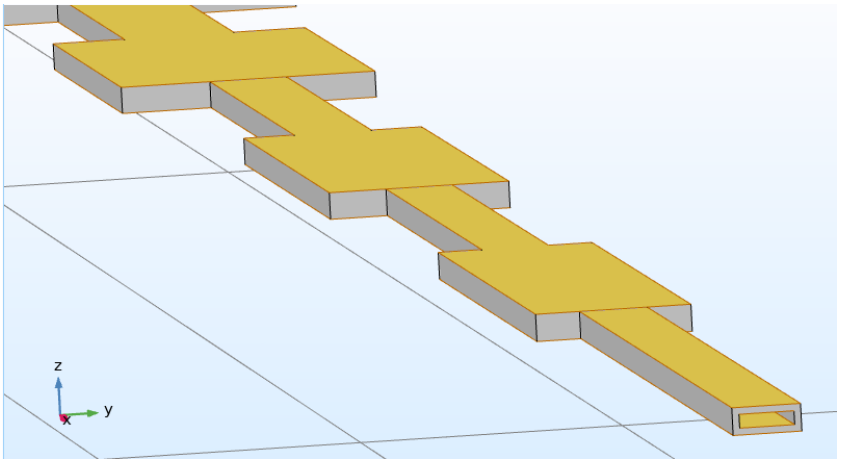

Figure 2.2: This figure highlights in yellow the surfaces that are generally used to calculate $Q_{surface}$ which are the top and bottom surfaces of the resonator and that of the channel.

Another issue is that it is not immediately clear whether or not the walls of the channel itself should also count towards the surface energy loss as these surfaces are technically not exposed during operation of the resonator, as during operation the resonator is filled with a fluid. To look into the effect that the channel walls have on the $Q_{surface}$, it is compared with the $Q_{surface}$ without taking the channel walls into account. The values can be found in table D.2 which is located in the appendix and are calculated using equation 2.13. For the tapered beam design, one of the two main models discussed in chapter 3, these values are very comparable.

Finally, the validation of the mechanical Q-factor calculation is discussed. Validating the calculation proved very difficult as performing experiments was not within the scope of this thesis. After having considered a couple of resonators to be used as a way of validating the calculation, none of the models created based on these resonators quite match their experimental values. The resonators that were considered were the three main resonators from Manalis et al., [44],[21],[37] and the resonator by Craighead et al. [3] The Q-factors of the Manalis et al. resonators match up the best, with at most about a 50% difference. The biggest problem with these resonators is that they are made from silicon instead of silicon nitride. This means that the values for Q_{volume} and $Q_{surface}$ are not the same as the ones presented before as those values are calculated from silicon nitride resonators. It is plausible that these values aren't that different for silicon than silicon nitride but that is pure speculation. The model based on the resonator by Craighead et al. had a different problem. The material of this resonator is silicon nitride but the Q-factor calculated from it was off by about an order of magnitude. One possible explanation is that in contrast to the resonators considered here, the clamping losses for this resonator aren't negligible as $Q_{clamping} \propto \frac{l}{w}$. [38] Here, l is the length of the resonator which is 20 um, and w is the width of the resonator which varies between 0.65 um and 2.5 um. [3] This means that validating the mechanical Q-factor equation isn't possible through other suspended microchannel resonators which only leaves validating the equation through other resonators that do contain phononic crystals. This is done for the uniform unit cell design by Ghadimi et al. The Q-factor for this recreated model was about 1E8 which is within the expected values judging from graph 3G from the paper by Ghadimi et al. [5]

2.3. The Fluid-loss Q-factor

Lastly, the Q-factor attributed to fluid-loss or Q_{fluid} should also be considered. As has been mentioned before, Manalis et al. have studied this Q-factor extensively and confirmed that for their suspended nanomechanical resonators, the total Q-factor is largely unchanged or even slightly increased for resonators filled with water. [21] As experiments are not an option for this work, the determination of fluid-loss Q-factor will be based on the equations developed by the Manalis group. As equation 1.6 mentioned in chapter 1 is only accurate for cantilevers excited in their fundamental mode, a more general equation will be considered.

$$\mathbf{e} = -i\omega\left(1 - \frac{1-i}{2}\sqrt{\frac{\beta}{2}}\frac{cosh((1-i)\sqrt{\frac{\beta}{2}}z)}{sinh(\frac{1-i}{2}\sqrt{\frac{\beta}{2}})}\right)\frac{dW}{dx}(\mathbf{xz} + \mathbf{zx}) \tag{2.14}$$

$$E_{diss} = \int\left(\frac{2\pi\mu}{\omega}\left(\mathbf{e} : \mathbf{e}^* - \frac{1}{3}\left|tr(\mathbf{e})\right|^2\right)\right)dV \tag{2.15}$$

$$Q_{fluid} = \frac{2\pi E_{kin}}{E_{diss}} \tag{2.16}$$

The equation used to calculate the fluid-loss Q-factor is equation 2.14 which is the rate of strain tensor of the fluid channel based on the velocity field. [19] This equation needs to be substituted in equation 2.15 to calculate the dissipated energy due to the fluid. Beta, which is the Reynolds number, can be calculated separately after which equation 2.15 can be used in COMSOL to calculate the dissipated energy by integrating it over the channel volume. This way of calculating the dissipated energy can be considered because the only relevant parameters the equation needs from COMSOL is the modeshape and the deflection. These are automatically calculated during the eigenfrequency analysis as already performed to calculate the mechanical Q-factor. Finally, the dissipated energy can be substituted in equation 2.16 to calculate the Q_{fluid} of the system which uses the total kinetic energy of the resonator as the stored energy of the system. All of these equations have been obtained from [19]. These equations also form the basis of equation 1.6 as this equation is essentially a simplified form, accurate only for cantilever resonator excited in the fundamental resonance frequency.

Equation 2.14 only considers the so-called ”On-axis flow” which is the case when the channel is placed on the neutral or symmetry axis of the resonator. [19] A more elaborate equation exists that takes the energy dissipation into account when the channel is placed off-axis but this will be neglected here and it will be assumed that the channel is indeed placed on the neutral axis. In a separate paper the mode dependence is also investigated. [1] For the on-axis problem however, the mode dependence is restricted to the deflection and Reynolds number only, something that is easily calculated by COMSOL. There’s also something to be said about the defect eigenmode. As Sader et al. notes, one of the reasons, and the only reason in the case of the on-axis problem, that the Q_{fluid} is lower for higher order modes is that the deflection is also higher for these modes. [1] However, due to soft-clamping, the curvature and so also the deflection of the defect eigenmode is severely reduced. [5] [45] It could imply that the fluid-loss Q-factor could also be higher for the defect eigenmode compared to other eigenmodes of similar frequency. However, looking into this matter is beyond the scope of this thesis. Sader et al. also investigated the dependence of the Q_{fluid} on the poisson’s ratio. [2] This dependency is however only the case when the channel is placed off-axis, either by fabrication errors or on purpose, but again, here the assumption is made that the channel is placed on-axis.

Lastly, there is also something to be said about the energy dissipation due to the fluid at the side walls of the channel. This energy dissipation is neglected in equation 2.14, but the appendix of [19] also contains the complete velocity field that takes it into account. This energy dissipation could potentially be more significant than in the cantilever resonators by Manalis et al. as the channel width to channel height ratio is less in the resonators that are considered here. Specifically, 700 nm to 400 nm in the worst case scenario versus 1400 nm to 400 nm in the case of the resonator by Manalis et al developed in [37]. For the sake of completeness, the complete velocity field was derived into a rate of strain tensor and used on the resonators discussed in chapter 3. When compared with the results from equation 2.14, the difference in energy dissipation is less than one percent which means the dissipation at the side walls can be safely neglected.

To validate the fluid-loss Q-factor, and the method with which they can be calculated, the resonator

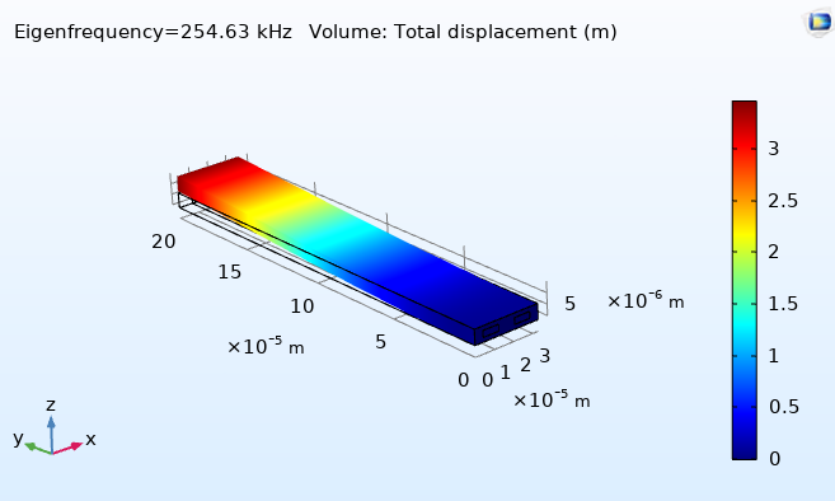

Figure 2.3: An image of the COMSOL model replicating the resonator from [44]. This model is used to calculate the numerical Q_{fluid}. Its fundamental mode is shown.

	Analytical Q_{fluid}	Numerical Q_{fluid}
Manalis et al. (2007) [44]	$1.313{\cdot}10^5$	$1.072{\cdot}10^5$
Manalis et al. (2010) [21]	$8.172{\cdot}10^5$	$7.100{\cdot}10^5$
Manalis et al. (2014) [37]	$8.760{\cdot}10^5$	$6.838{\cdot}10^5$

Table 2.1: This table compares the analytically calculated Q_{fluid} using equation 1.6 with the numerically calculated Q_{fluid} based on equation 2.16 and a corresponding COMSOL model. As can be seen, the values are very comparable.

designs by Manalis et al. have been replicated in COMSOL on which equation 2.15 have been used and compared with the analytical result based on equation 1.6. The models work as follows: First, the cantilevers are replicated using the dimensions provided in the corresponding papers. Second, the channel is filled with a mesh and the channel domain, which is simulated as a solid, is given the density of water. The purpose of this is to simulate the mass and eigenfrequency change only, just so that these values can be used to calculate the Q_{fluid}. The result of these simulations is summarized in table 2.1, with an image of one of the resonator models provided in figure 2.3. As can be seen from the table, the results match each other quite well with the models from 2007 and 2014 having about 18 % and 22 % difference between the analytical calculation and the numerical one respectively. The model of the resonator from 2010 has a smaller difference of about 13 %. With these results it should be reasonable to expect that the numerical Q-factor calculation will give a good result for the resonators discussed in chapter 3 as well.

3

Resonator Design and Optimization

In this chapter, the designs and optimization of the resonators will be discussed. There are two types of models that are considered here and whose design variables are optimized using machine learning through Bayesian optimization. The optimization is performed in two parts. First, the Qf product will be optimized to see if the threshold value of $6 \cdot 10^{12}$ Hz can be reached and to see how the individual design variables depend on each other in the case of the tapered beam model. The Qf product optimization is also performed on the so-called MDV model or simply, the multi design variable model which has 11 design variables. The optimization as considered here then, is performed on two different models. Afterwards, the MDV model is also optimized for the mass sensitivity in two different variants, a 1 um thickness variant and a 200 nm thickness variant. This for the sake of showing what is possible at a smaller scale. The appendix also contains some alternative models like the uniform unit cell model and smaller variants of the MDV and tapered beam models.

3.1. COMSOL Modelling

First, in this section the COMSOL models and optimization processing will be elaborated further. The models discussed in this chapter consist of full 3d elements which use the solid mechanics module in COMSOL. The resonators here also use both the stationary study step and the eigenfrequency analysis, as is necessary to account for the pre-stressed nature of the designs. Only half of a resonator is simulated which is valid as the resonators are supposed to be completely symmetric. This massively cuts down on the number of degrees of freedom and so also computation time. For this purpose, a symmetry condition is applied at the center defect boundary. On the other end which connects the resonator to the substrate, a fixed constraint is applied. There is no distinction between the two study steps as far as the applied conditions are concerned. The eigenfrequency analysis uses the region option which means that the range of frequencies in which the solver searches for eigenfrequencies is decided upon by manually selecting the lower and upper boundaries of this region. For the material of the resonator the standard silicon nitride material was used with E = 250 MPa, $\rho = 3100 kg/m^3$ and v= 0.23. These are the Young's modulus, density and Poisson's ratio respectively. The applied initial stress is 1300 MPa and is applied on every part of the resonator. All optimized models also simultaneously calculate the mechanical Q-factor and the Q_{fluid} to calculate the total Q-factor, so that the Bayesian optimization uses the total Q-factor for the optimization which accounts for fluidic losses. This is especially important as the MDV model also includes design variables that could directly impact the Q_{fluid}, such as the tapering of the channel and its height. As has been mentioned in chapter 2, it does this by filling the channel with a domain which has the density of water to simulate the frequency shift due to the fluid inside the channel. This domain can then be used to calculate the energy dissipation due to the fluid from equation 2.15 which uses the deflection and modeshape to perform this.

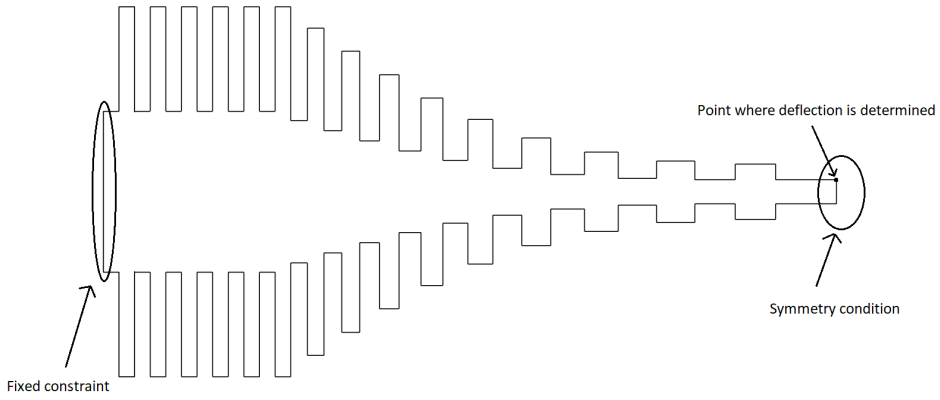

Figure 3.1: A figure displaying the boundary conditions of the COMSOL model. These boundary conditions are the same for every model considered. The surfaces of these boundary conditions are selected with the help of box selections.

Most of the processing on these models is done in Matlab with simulation done in COMSOL. This is necessary to perform the optimization as every iteration has to be handled completely automatically. Matlab is then able to collect the variables of interest like the Q-factor, eigenfrequency and mass sensitivity and put them in a separate Excel file to save the optimization history. This is very useful as the Bayesian optimization only saves the optimized parameter and the normalized design variables. The Excel worksheet can then be used later for analysis and be used for figures. Matlab is also responsible for calculating the geometry of the tapered beam design and the MDV model. Matlab calculates every point necessary for the polygon that COMSOL uses to determine the geometry of the resonator. It does this in conjunction with the relevant design variables of that specific model.

Another important part of the processing in Matlab is that the code has to be able to select the eigenfrequency of the defect mode reliably to be able to calculate the Q-factor of the correct eigenmode. To do this, COMSOL calculates the deflection of the resonator at the center defect for every eigenmode by selecting a point at that location and then determines the one that has the largest deflection. The eigenmode with the largest deflection is the defect eigenmode. To ensure that the right point, surface or domain is selected for their specific purpose, box selections are used. This is done because otherwise COMSOL would rely on the number that is assigned to that specific point or surface which may vary between optimizations. Box selections in COMSOL depend on the x, y and z coordinates that are attributed to them. Box selections are also used to select the surfaces for the fixed constraint and the symmetry condition and to select the surfaces necessary to calculate the dissipated energy due to the exposed surfaces from equation 2.13 for the same reasons as mentioned above. In case of the latter, the individual box selections are also summed into cumulative selection so that the complete surface integral can be calculated at once.

Most of the COMSOL simulations are performed on one of the research clusters of the TU Delft. This proved to be necessary as the models are very memory intensive because of the large number of degrees of freedom necessary, namely on the order of several million, to model the designs properly. The individual simulations generally required more than 100 GB of RAM and used four processors on one node. As the optimizations also take a long amount of time, a couple of days for about 100 iterations, it was also a matter of convenience to be able to run the optimizations on the cluster. As mentioned in chapter 1, the specific version of Bayesian optimization used in this thesis is GPyopt. [7] GPyopt is python based, and as such the optimization algorithm itself runs in python. The python script calls on the Matlab code used for each model. The python script also contains information such as the design variables and whether they are either continuous variables or discrete. Before the optimization can be performed, the convergence of the Q-factor needs to be discussed first to ensure good simulation results. It is also important to strike a good balance between computation time and accuracy of the result as the machine learning optimizations involve a lot of iterations required.

The convergence will be checked of both the 1 um thickness variant and the 200 nm thickness variant of the tapered beam model. To illustrate what these models look like, see figure 3.6 which provides an overview of the relevant dimensions of the model and figure 3.15 to see the difference between the two size variants. For the sake of brevity however, the convergence of the 200 nm thickness variant can be found in the appendix. As these variants are shared with the MDV model, the assumption will be made that the results are valid for those models as well.

There are two variables of interest for the converge checks. First is the minimum element size whose value directly translates in the amount of elements allocated for a given geometry. The second is the ratio of elements allocated in the length direction of the resonator. As the resonator is very long, the idea behind this variable is to reduce the number of elements in this direction while still having small elements in the width and height direction of the resonator. Because of the length of the resonator, reducing this variable will cut into the number of degrees of freedom quite dramatically and thereby also reducing computation time a lot as well. To illustrate the convergence checks for each variant, two surface plots are presented for each. The surface plots have the two variables on the x and y axes and the value of interest on the z-axis. The color indicates the number of degrees of freedom.

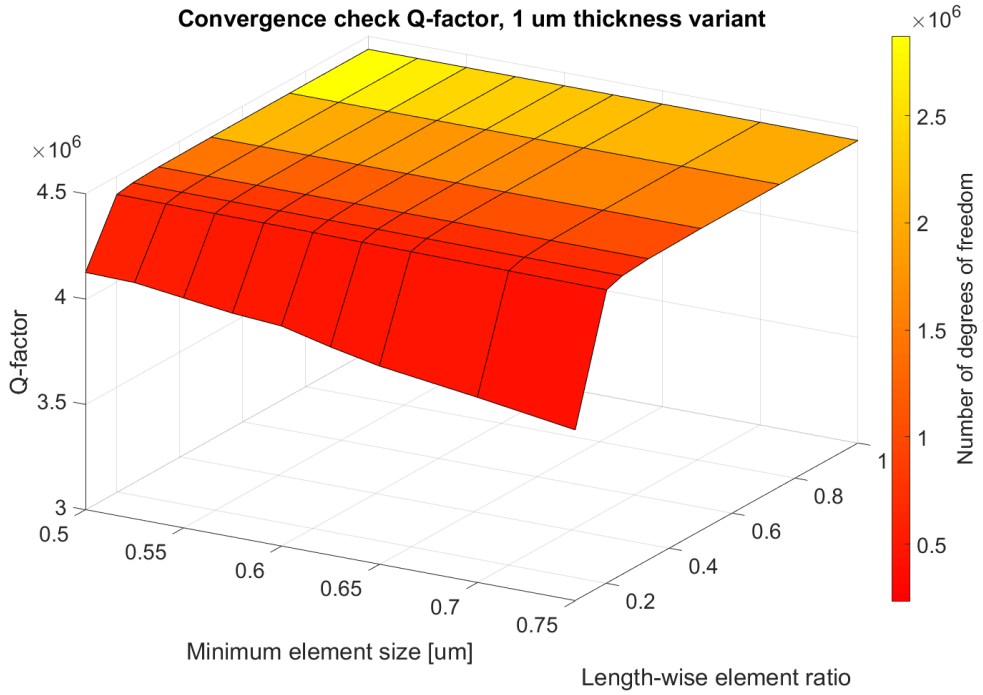

Figure 3.2: The convergence check plot of the Q-factor. The model is the 1 um thickness variant of the tapered beam model.

For the 1 um thickness variant it can be said judging from figure 3.3, which displays the computation time, that it won't be much of an issue for this model as the longest computation time is about 700 seconds. Figure 3.2 shows the mechanical Q-factor of the convergence check across the two variables and as can be seen the Q-factor stays remarkably consistent. The Q-factor only drops significantly when the length-wise element ratio becomes really small, either 0.1 or 0.2 meaning only about 10% and 20% of the number of elements are allocated in the length-wise direction compared to the other two directions. Effectively, this means that the convergence of the Q-factor is very good. From this, it would be quite easy to choose the two variables, which were chosen to be 0.5 um for the minimum element size and 0.25 as the length-wise element ratio. The latter cuts the number of degrees of freedom by about three quarters while the computation time is about 300 seconds. During optimization it is likely that the computation time will change, especially in the case of the MDV model as it seems very likely that computation time will scale with the number of unit cells. Another thing to mention is the case when the channel is filled which would naturally also increase computation time and degrees of freedom as elements would need to be allocated to this space as well. This is not done for the models used to

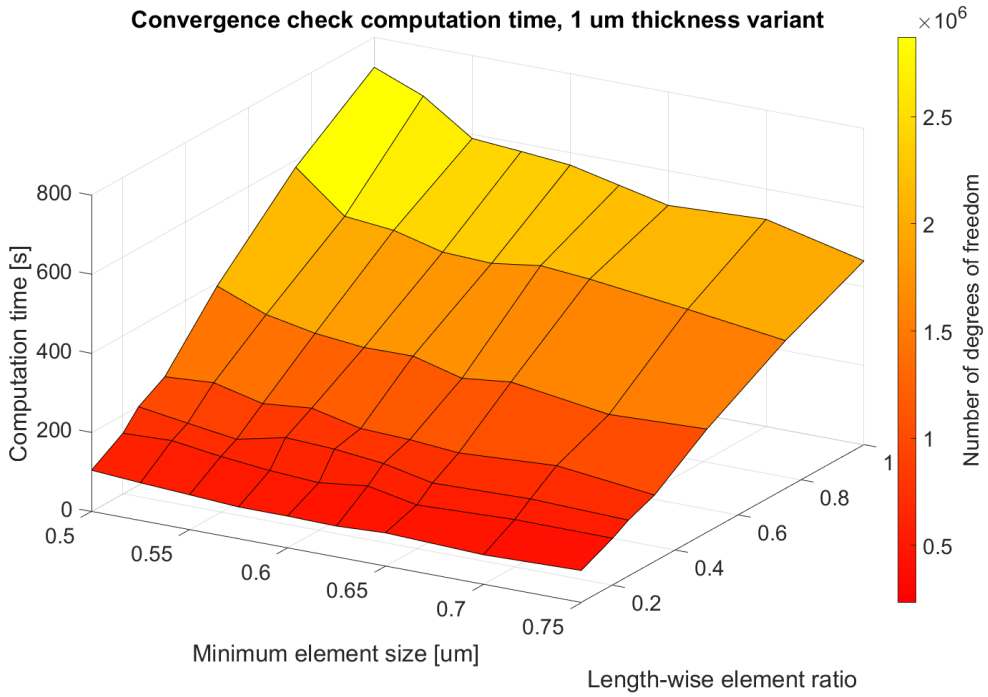

Figure 3.3: The convergence check plot of the computation time. The model is the 1 um thickness variant of the tapered beam model.

calculate the convergence checks. It should also be mentioned that for smaller values of the minimum element size for both the 1 um thickness variant and the 200 nm thickness variant, the simulations fails as COMSOL runs out of memory, even when running on a cluster node that has 256 GB of RAM.

There is however the case that when the element size is too big, COMSOL can't model the resonator properly anymore and will output warnings when this is the case as the minimum element size is bigger than the size of a specific feature of the geometry COMSOL tries to mesh. These warnings do not affect whether the simulation will run or not, so extra care to prevent this must be taken. One point of concern is however what would happen if the wings have their width decreased as is possible in the case of the MDV model. It could possibly mean that in that case the convergence wouldn't be as good. For that reason a ratio of 0.25 is chosen instead of going for even lower values of the length-wise element ratio and using the smallest value of the minimum element size, 0.5 um, as this does not have a negative impact on computation time to have a nice balance between convergence and computation time.

To illustrate what the mesh of these models look like, figures 3.4 and 3.5 show the mesh of the 1 um thickness variant of one unit cell and its connection to another. Both figures have the minimum element size as 0.5 um which is also the value used for the optimizations of this variant. The difference is the length-wise element ratio. Figure 3.4 has a ratio of one and 3.4 has a ratio of 0.25, the value ultimately used for the optimizations. As can be seen, the effect of the length-wise element ratio is that the elements are somewhat predictably stretched out in the length-wise direction although it also appears that there is a slight reduction in the number of elements in the width direction in the widest part of the unit cell.

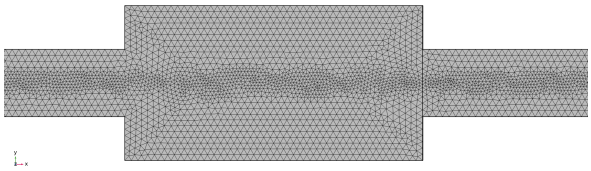

Figure 3.4: An image of an unit cell of the 1 um thickness variant which shows the mesh of the model. In this figure the length-wise element ratio is set to one.

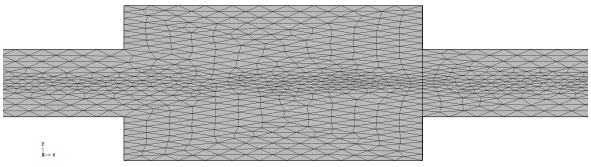

Figure 3.5: An image of an unit cell of the 1 um thickness variant which shows the mesh of the model. In this figure the length-wise element ratio is set to 0.25.

3.2. Optimizing the Qf Product

The Bayesian optimization of the Qf product of the tapered beam model consists of 100 iterations which include 20 initial iterations whose design variables are placed randomly. The MDV model has 150 initial iterations and 847 iterations in total. This uneven number is due to the algorithm being ran for as long as possible until time ran out. As this model has more design variables, it also needs more initial points to fill the design space. It should be mentioned that for the final optimized results of all models shown in this section a complete resonator model was made and simulated. This is done in order to check the correctness of the modeshape as calculated for one half of the resonator and to check the values of the optimization result for those models as well. Both the values and the modeshape given by the optimization algorithm appear to be correct and line up perfectly between the values and modeshapes of the full resonator models. Additionally, these full resonator models were also used for the corresponding figures. In this section, the two models optimized for the Qf product will be introduced sequentially.

3.2.1. The Tapered Beam Model

The tapered beam model uses strain engineering to increase the stress of the resonator locally by tapering the resonator towards the center. This should increase the dissipation dilution effect and so also increase the Q-factor, as reported by Ghadimi et al. [5] It should be mentioned that both this model and the uniform unit cell model are based on the resonators by Ghadimi et al. [5] An overview of the tapered beam design can be seen in figure 3.6 which also shows the design variables of the model and the microfluidic channel, indicated in blue. Figure A gives a top view of the resonator and figure B provides a cross-sectional view with relevant dimensions indicated. The tapered beam model has three design variables which are the length of the defect and two design variables that determine the tapering of the beam: alpha and i_0. The tapering is determined by the width of each unit cell as shown in the equation in figure 3.6. Concretely, alpha determines the amount of tapering while i_0 determines at which unit cell the tapering starts. The length of this model is fixed to 4 mm in total as are the number of unit cells at 15. The tapered beam model as shown here and the MDV model as shown in section 3.2.2 have cross-sectional dimensions that try to aim to be reasonable with a view on manufacturability. Moreover, the models also use some of the dimensions of the best performing resonator from [37] by Manalis et al. like the channel height in the case of the tapered beam model, the channel width and the thickness of the resonator for both models as a way of grounding this manufacturability to some basis as it can't be conclusively tested. The resonator width as indicated in figure 3.6 is the minimum fixed width at the center defect. Moreover, the tapered beam model has a strictly straight channel with the same dimensions as indicated.

The optimization results of the Qf product of the tapered beam model are presented together with the best performing suspended microchannel resonator in table 3.1. It lists the total Q-factor, which is the inverse summation of the $Q_{mechanical}$ and the Q_{fluid}, the resonance frequency, the Qf product, the effective mass and the mass sensitivity. As was said in the introduction, the resonator designs presented here have a total Q-factor of about two orders of magnitude higher than that of the best performing conventional design. The tapered beam model has a total Q-factor of $3.88 \cdot 10^6$ versus 15000 of the design by Manalis et al. Likewise, the Qf product is also two orders of magnitude higher compared

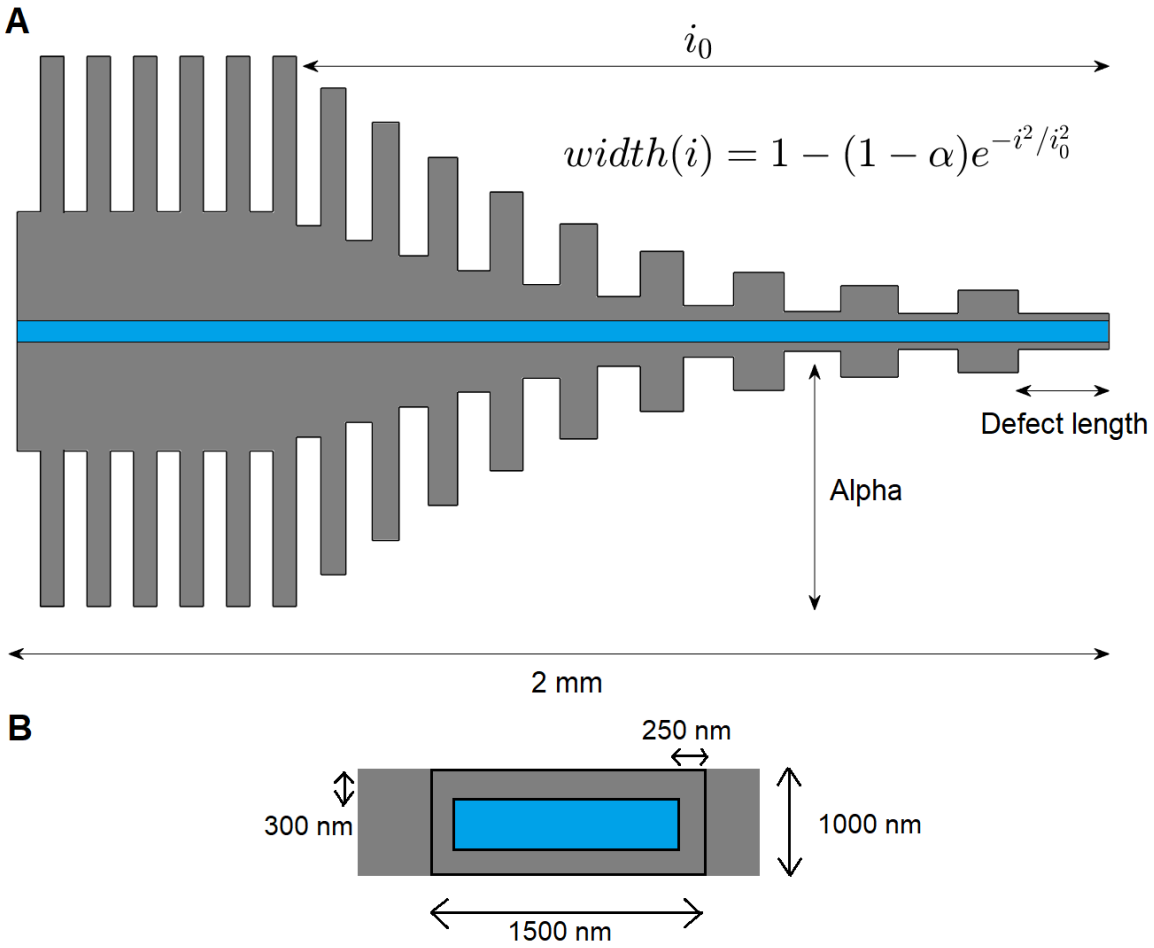

Figure 3.6: An overview of the tapered beam design with its design variables indicated. The channel is also indicated in blue. The formula in the figure is used to calculate the tapering.

to the highest performing conventional design. This puts the tapered beam model in the range where performing quantum mechanical experiments at room temperature is possible, as the optimized result reaches the threshold of $6 \cdot 10^{12}$ Hz. The resonance frequency of the tapered beam model is due to the number of unit cells used located at 1.56 MHz and is about half of that of the resonator by Manalis et al. The tapered beam model was also optimized for 25 unit cells to approximate the frequency range of the Manalis design but this caused Qf product to decrease to $5.8 \cdot 10^{12}$ Hz which is below the threshold for quantum mechanical experiments at room temperature.

	Total Q-factor [-]	Freq. [MHz]	Qf product [Hz]	E. mass [pg]	Mass sens. $[\frac{zg}{\sqrt{Hz}}]$
Tapered beam model	$3.88 \cdot 10^6$	1.56	$6.1 \cdot 10^{12}$	1519	10.83
Manalis (2014) [37]	15000	2.89	$4.3 \cdot 10^{10}$	92.3	9.49

Table 3.1: A table of the optimization results of the Qf product of the tapered beam design. It lists the total Q-factor, resonance frequency, Qf product, effective mass and the mass sensitivity of the models that have been optimized.

The next parameter of interest is the effective mass. The effective mass is important for the determination of the mass sensitivity. As can be seen in table 3.2, the tapered beam model has an effective mass of more than an order of magnitude higher than the design by Manalis et al. This can be easily explained due to the length of these models, as they are 4 mm in length versus that of the Manalis' design with a length of 22.5 um while the cross-sectional dimensions are relatively comparable. The

effective mass for these models is comparatively lower due to the localization of the eigenshape as a consequence of soft-clamping which also localizes the deflection as a whole. This results in an effective mass that's approximately 5% of the total mass for these resonator models. For cantilever beams, the effective mass is about 25% of the total mass according to the literature. [8] As the mass sensitivity depends on the effective mass according to equation 1.3, this enables a high mass sensitivity for resonators that are technically much heavier. Lastly, the mass sensitivity itself. As this section is about the models that are optimized for the Qf product, these values will be improved further in section 3.3 when the mass sensitivity is optimized. For the tapered beam model the mass sensitivity is comparable that of the design by Manalis et al. albeit slightly higher. As the mass sensitivity depends on Qf^2 and the tapered beam model has a relatively low resonance frequency.

	$Q_{surface}$	$Q_{mechanical}$	Q_{fluid}	Total Q-factor
Tapered beam model	53306	$4.21{\cdot}10^6$	$5.03{\cdot}10^7$	$3.88{\cdot}10^6$
Manalis (2014) [37]	-	-	$6.8{\cdot}10^5$	15000

Table 3.2: A table of the optimization results of the Qf product of the tapered beam design. It lists the different Q-factors of the models that have been optimized.

Table 3.2 lists the $Q_{surface}$, the $Q_{mechanical}$, Q_{fluid} and the total Q-factor. Important to note is that the Q_{fluid} causes a degradation in the total Q-factor for the tapered beam model. As far as the $Q_{surface}$ is concerned, for the tapered beam model and the MDV model in this section, it plays a much smaller role for the determination of the $Q_{intrinsic}$, as the $Q_{surface}$ is much larger at about 55000 on average than the Q_{volume} which is 28000 according to the literature. [26]

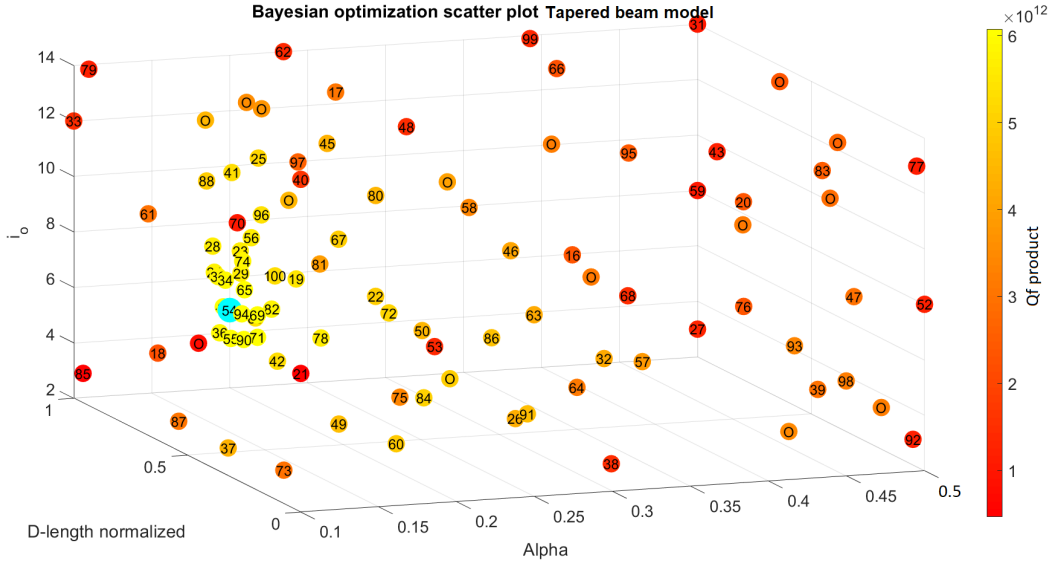

Figure 3.7: The scatter plot of the tapered beam model which shows the design space. The optimum Qf product is indicated in cyan.

Next, the optimization history will be discussed. Figure 3.7 displays a 3D scatter plot of the tapered beam model with the three design variables mapped to the axes. Each dot is an individual iteration and the color indicates the Qf product. Yellow indicates a high Qf product, red a low one. The final optimum point is also indicated in cyan. The algorithm allocates a lot of points near the optimum point. It can be seen that the algorithm intermittently allocates points away from the optimum point in an effort to look for global optima instead of local optima which it is more likely to find. These points appear to be sparse though, as the algorithm might have sectioned off values of alpha that are higher than 0.25 as Qf products are low for this region. A lot of the points in this region are also randomly allocated as part of the initial iterations. The code is instead more interested in varying alpha as little as possible and vary the defect length and especially i_0 instead. Note that alpha indicates the degree of tapering, with 0.1

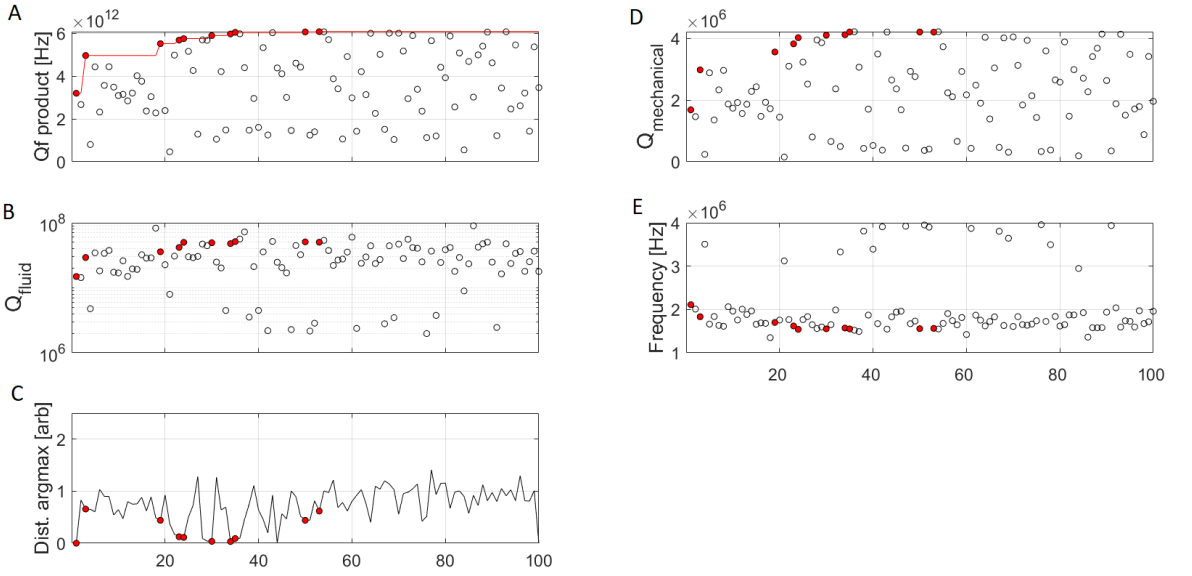

Figure 3.8: The optimization history of the tapered beam model. It provides an overview of the optimization history of the Qf product, with the optima indicated in red, the Q_{fluid}, the $Q_{mechanical}$, the resonance frequency and the distance between the best optima per iteration.

as the highest amount of tapering possible for the algorithm. Higher degrees of tapering would likely increase the stress at the center of the resonator and so contribute to a higher mechanical Q-factor.

Figure 3.8 contains the optimization history of the tapered beam model. The first graph maps the Qf product to the iterations with the optima indicated in red. As can been seen, the algorithm finds new optima very quickly after it has simulated the 20 initial points. The final optimum point is found shortly afterwards. The graph next to it tracks the mechanical Q-factor and as can be seen, a high mechanical Q-factor can be quite indicative of also being an optimized point. The second graph in the second column is the resonance frequency of the defect mode. The frequency remains quite consistent throughout the optimization. As has been said earlier, this is likely due to design space for this model as it likely doesn't allow for a lot of variance in the frequency. The second graph of the first column is the Q_{fluid}. Here the dependence of the Qf product can be seen as well, as a high Q_{fluid} is necessary so that it does not impact the total Q-factor. Finally, the third graph in the first column indicates the distance of the design variables from the latest optimum point at that time. This graph makes it clear that the new optima the algorithm finds at around iteration number 20 are local optima, as the distance between the points is small. This is of course visually confirmed by figure 3.7. The final optima appears to have same distance between its previous optima as judged from figure C, indicating that this could be a more global optimum. Finally, the algorithm also appears to look for more global optima after it finds the final optimum point as the distance between the points is much larger than before. It is however unable to find any such global optima. The geometry and the defect eigenmode of the tapered beam model is shown in figures 3.9 and 3.10, respectively. Figure 3.9 also shows the microfluidic channel in blue. The modeshape clearly displays the soft-clamping effect as the vibration has completely damped out near the boundaries. The deflection shown is arbitrary as COMSOL has normalized the deflection.

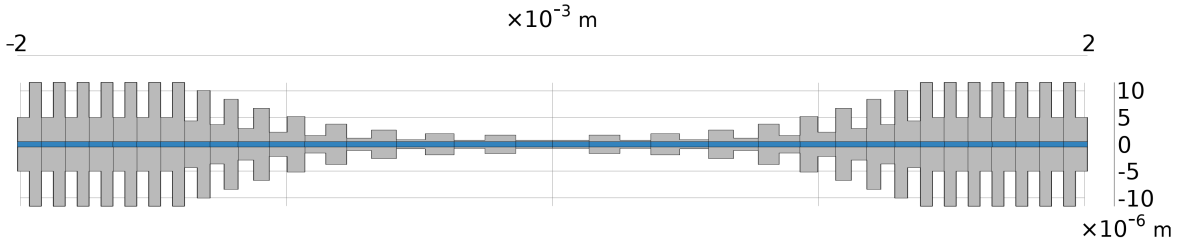

Figure 3.9: A figure of the geometry of the tapered beam model optimized for the Qf product. The microfluidic channel is indicated in blue. The length has been scaled down for presentation purposes to 1:20.

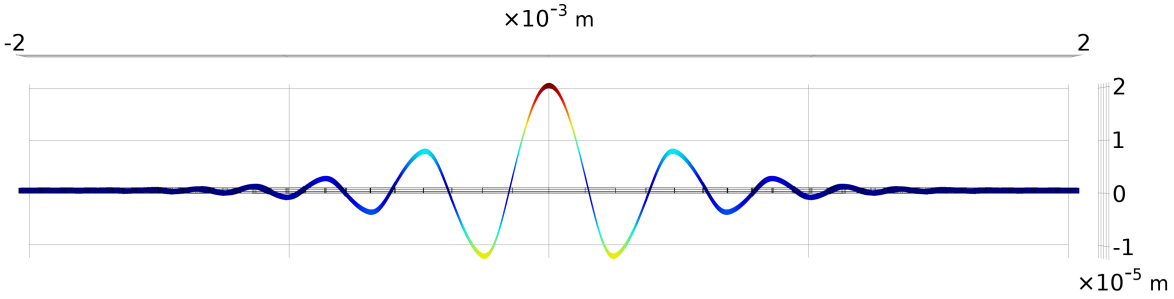

Figure 3.10: A figure of the modeshape of the optimized tapered beam model.

3.2.2. The Multi Variable Model

The second and last model to be introduced is the multi design variable model, or MDV model. This model tries to open up the design space by adding more design variables to potentially allow for an even better Qf product and mass sensitivity. This could potentially also allow for better strain engineering as the strain can be more precisely determined due to the increased design space which allows for more variable geometry. As this model is the same for both the Qf product optimization and the mass sensitivity optimization, the model tries to strike a balance to provide both optimizations with interesting design variables. The MDV model is shown in figure 3.11 with the design variables indicated and the channel colored blue. First, The MDV model does away with the equation to taper the resonator as shown in figure 3.6 and replaces it with five design variables that determine the minimum width at that specific location. The minimum width nodes are placed evenly away from each other. The example as shown gives an idea of what kind of resonator shapes can be achieved using the MDV model. This specific example is for visualization purposes only. The length of the defect is once again also a design variable and now the width and the length of the wings are also design variables. Contrary to the tapered beam model, the MDV model does allow for the number of unit cells to be varied, from 15 unit cells to 50 unit cells. This design variable is mainly included for the fact that the resonance frequency of the defect mode tends to increase with the number of unit cells. [5] As the mass sensitivity also scales with Qf^2, this could allow for a better mass sensitivity. As indicated in figure 3.11, this model also allows for a tapered channel, one that approximately follows the shape of the resonator overall. This model then also includes a design variable to scale the tapering of the channel all the way down to it being completely straight. Finally, the MDV model also includes a design variable that allows for varying the height of the channel from 150 nm to 700 nm in height as indicated in 3.11 B. The MDV model as shown here shares the cross-sectional dimensions with the tapered beam model other than the channel height.

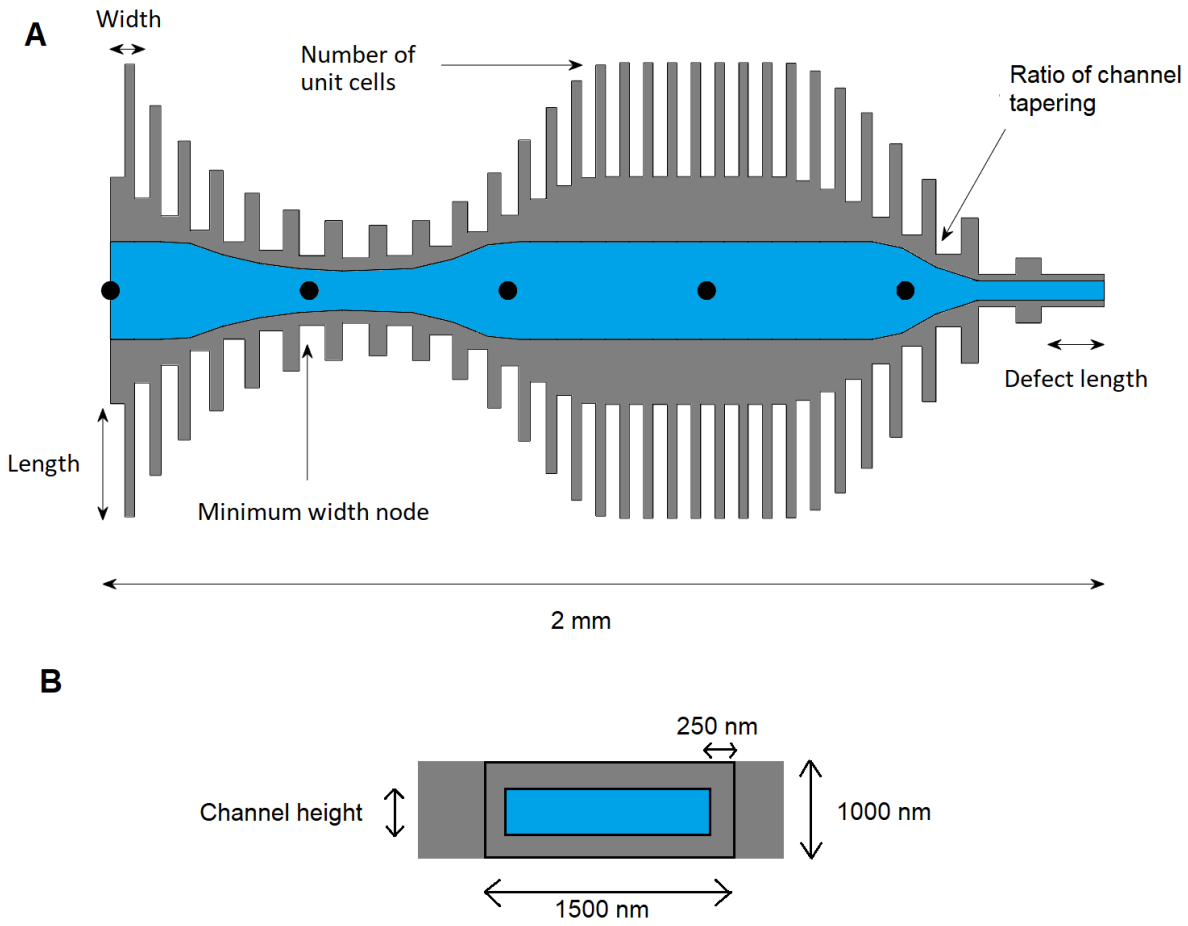

Figure 3.11: A figure showing an overview of the MDV model and its design variables. The channel is also indicated in blue. The tapering shape of the channel and that of the resonator are done for visualization purposes only.

	Total Q-factor [-]	Freq. [MHz]	Qf product [Hz]	E. mass [pg]	Mass sens. $[\frac{zg}{\sqrt{Hz}}]$
MDV model	$4.55{\cdot}10^6$	1.74	$7.90{\cdot}10^{12}$	1563	3.91
Tapered beam model	$3.88{\cdot}10^6$	1.56	$6.1{\cdot}10^{12}$	1519	10.83
Manalis (2014) [37]	15000	2.89	$4.3{\cdot}10^{10}$	92.3	9.49

Table 3.3: A table of the optimization results of the Qf product with both the MDV model and the tapered beam design. It lists the total Q-factor, resonance frequency, Qf product, effective mass and the mass sensitivity of the models that have been optimized.

The optimization results of the MDV model optimized for the Qf product are shown in table 3.3, together with the tapered beam model and the best conventional design by Manalis et al. As can be seen, the Q-factor and the resonance frequency of the MDV model are even higher than that of the tapered beam model. This results in an even higher Qf product of $7.90{\cdot}10^{12}$ Hz which is an increase of about 30%. As has been mentioned before, the MDV model contains design variables that also allow more variance in the resonance frequency, which means that frequency can also be higher compared to the tapered beam model which would directly result in a higher Qf product. The number of unit cells however, one of the design variables directly responsible for a higher resonance frequency as noted by Ghadimi et al., is only 15 for the optimized model. [5] The explanation of this higher total Q-factor is given in figure 3.4 by way of an increased $Q_{mechanical}$ and a much higher Q_{fluid}. The reason why the Q_{fluid} of the MDV model is so much higher than the tapered beam model can be explained by the fact that the height of the channel for the tapered beam model is much bigger than that of the MDV model, 400 nm

in height vs 150 nm in height for the optimized result of the MDV model. As the MDV model allows for a smaller channel height, the Q_{fluid} is two orders of magnitude higher. This is the case as both the Reynolds' number and the energy dissipation of the fluid scale with the channel height. [43] This causes the impact of the Q_{fluid} on the total Q-factor to be negligible in the case of the MDV model.

	$Q_{surface}$	$Q_{mechanical}$	Q_{fluid}	Total Q-factor
MDV model	56223	$4.55{\cdot}10^6$	$5.07{\cdot}10^9$	$4.55{\cdot}10^6$
Tapered beam model	53306	$4.21{\cdot}10^6$	$5.03{\cdot}10^7$	$3.88{\cdot}10^6$
Manalis (2014) [37]	-	-	$6.8{\cdot}10^5$	15000

Table 3.4: A table of the optimization results of the Qf product with both the MDV model and the tapered beam design. It lists the different Q-factors of the models that have been optimized.

Finally, the optimization history of the MDV model is shown in figure 3.12. As mentioned earlier, the MDV model has 847 iterations as it also has more design variables than the tapered beam model. As can be seen in figure A, the algorithm needs substantially longer to find the final optima due to the number of design variables. Contrary to the tapered beam design, the mechanical Q-factor of the initial points is quite low, as during this period it never finds Q-factor higher than 2 million. There also appears to be a substantial jump in mechanical Q-factor for the optimum point at around iteration 250. It also seems that this jump in mechanical Q-factor is mirrored in the Q_{fluid} as it also jumps to about two orders of magnitude higher at the around the same iteration. As far as the resonance frequency is concerned, shown in figure E, the range of frequencies is now a lot larger compared to the tapered beam model. However, as was also shown in table 3.3, the frequency of the MDV model has a similar value than that of the tapered beam model. As it is the Qf product that gets optimized the algorithm gives equal importance to the Q-factor and the resonance frequency. It seems likely that for the iterations that have a higher frequency, this comes at the cost of a lower Q-factor. Large enough that it also results in a lower Qf product. Drawing conclusions from figure C is a bit harder, as the distance between optima doesn't become that small. However, this could indicate that the new optima the algorithm keeps finding are in fact global optima as the distance between optima is substantial.

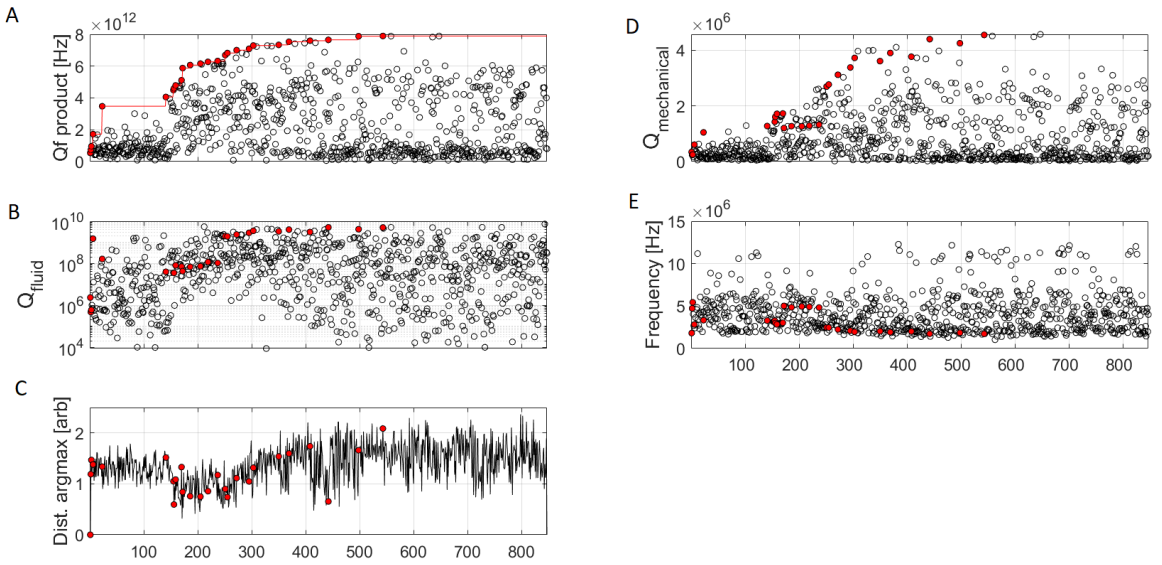

Figure 3.12: The optimization history of the MDV model optimized for the Qf product.

The geometry and the modeshape of the optimized MDV model is shown in figures 3.13 and 3.14. The geometry of the MDV model optimized for the Qf product is very similar to that of the tapered beam mode in both the number of unit cells, 15, and the shape of the tapering as well. The MDV model then, seems to achieve its increase in Qf product from the optimization of the unit cells and reducing the

height of the channel to 150 nm which increased the Q_{fluid} to such an extend that it does not impact the mechanical Q-factor negatively anymore. The appendix contains a scatter plot that displays the relation between Q_{fluid} and two ”channel variables”, the ratio of the tapering of the channel and the channel height. The modeshape as can be seen in figure 3.14, is virtually identical to that of the tapered beam model shown in figure 3.10.

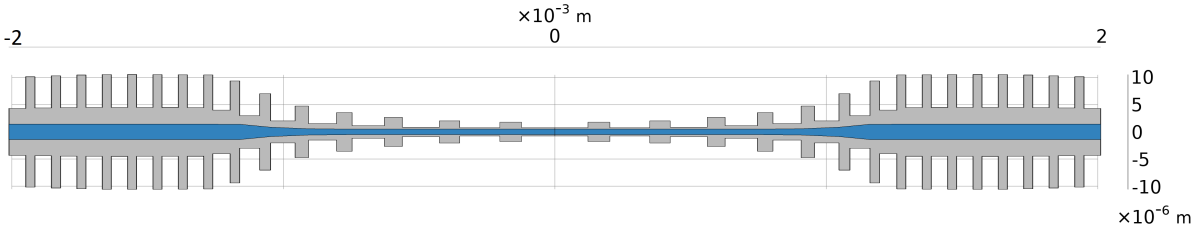

Figure 3.13: A figure of the geometry of the MDV model optimized for the Qf product. The microfluidic channel is indicated in blue. The length has been scaled down for presentation purposes to 1:20.

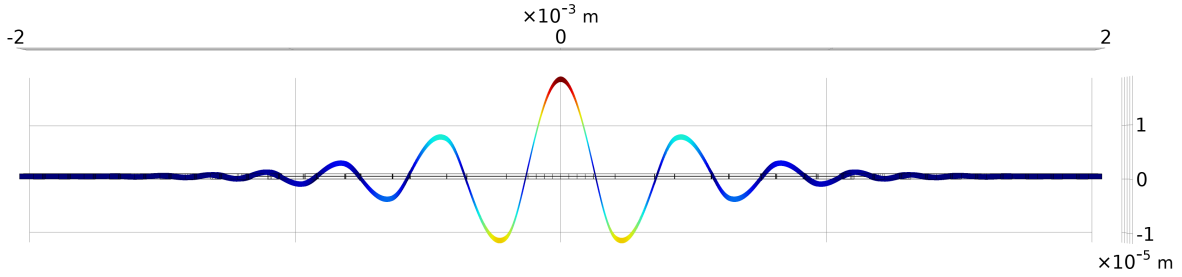

Figure 3.14: A figure of the modeshape of the MDV model optimized for the Qf product. Note its similarity to the modeshape of the tapered beam model.

3.3. Optimizing the Mass Sensitivity

Next, the mass sensitivity will be optimized. For this optimization only the MDV model shown in figure 3.11 will be considered. However, for this section the 200 nm thickness variant will also be considered in addition to the 1 um thickness version as has been shown in the preceding section. The two variants are shown in figure 3.15 and as can be seen, the 200 nm thickness variant does not have the design variable to vary the height of the channel. This is because the height of the resonator is already as small as it is, so it was decided to make it a constant value of 100 nm. This means that the 1 um thickness variant has 11 design variables but the 200 nm thickness variant only has 10 design variables. To avoid confusion, the 1 um thickness variant and the 200 nm thickness variant of the MDV model will be referred as such from here on.

The optimization results of the mass sensitivity are shown in table 3.5. As can be seen, both variants offers more than an order of magnitude increase in mass sensitivity compared to the resonator by Manalis et al. As the mass sensitivity as defined by equation 1.3 scales with Qf^2, the emphasis on the Q-factor is subdued and as a result has dropped significantly compared to the results of the optimization of the Qf product from table 3.3. With an increased importance the resonance frequency is now 8 times as high as it was for the Qf optimization in the case of the 1 um thickness variant. Likewise the effective mass of the MDV model is now a third compared to the MDV model when it was optimized for the Qf product. This is likely due to the increased localization of the eigenmode as the model here has 50 unit cells. This also shows the increased importance on resonance frequency. Consequently, as a result of the significant drop in Q-factor, the 1 um thickness variant no longer has a Qf product higher than $6 \cdot 10^{12}$ Hz which is the minimum Qf product necessary to perform quantum mechanical experiments at room temperature. There do exist intermediate optimization iteration results that do provide both the minimum Qf product of $6 \cdot 10^{12}$ Hz and the order of magnitude improvement of mass sensitivity

compared to Manalis et al. (2014). Alternatively, the 200 nm thickness variant could be considered, which has a Qf product of almost three orders of magnitude higher compared to the Manalis design which means that it is safely above the quantum mechanical limit. In addition, the mass sensitivity of the 200 nm thickness variant is also twice as high as that of the 1 um thickness variant.

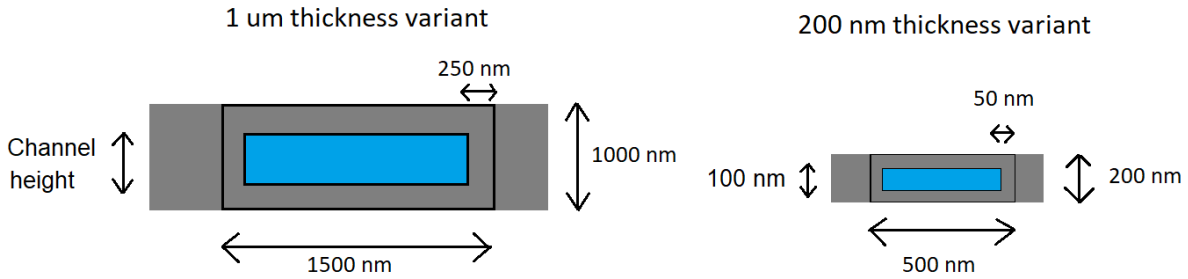

Figure 3.15: A figure displaying the cross-sectional view of both the 1 um thickness variant and the 200 nm thickness variant. Both variants are tapered and the corresponding dimensions are included in the figure. The variants are not to scale. In the case of the MDV model, the thickness of the top and bottom walls can vary as a result of the design variable which changes the height of the channel.

	Mass sens. $[\frac{zg}{\sqrt{Hz}}]$	Total Q-factor [-]	Freq. [MHz]	Qf product [Hz]	E. mass [pg]
1 um thickness variant	0.74	$1.83 \cdot 10^5$	10.96	$2.0 \cdot 10^{12}$	564
200 nm thickness variant	0.34	$6.89 \cdot 10^6$	6.03	$4.2 \cdot 10^{13}$	30.6
Manalis (2014) [37]	9.49	15000	2.89	$4.3 \cdot 10^{10}$	92.3

Table 3.5: A table of the optimization results of the mass sensitivity. It lists the mass sensitivity, the total Q-factor, resonance frequency, Qf product and the effective mass. The two variants listed are of the MDV model.

Figure 3.16 shows the optimization history of the 1 um thickness variant of the MDV model. As the MDV model here is the same as the one considered for the Qf optimization, there are once again 150 initial iterations with a total number of 820 iterations. When looked at figure 3.16, figure D, the optimization history of the mechanical Q-factor confirms that the algorithm does not consider the mechanical Q-factor to be that important as the history shows that the mechanical Q-factor never seems to reach $1.50 \cdot 10^6$ which is only about a third of the Q-factor of the MDV model optimized for the Qf product. For the resonance frequency shown in figure E, there seems to be a clear mean value of about 6 MHz whereas this was not the case for the model optimized for the Qf product. Additionally, the frequency of the final optimum is also one of the highest values, which clearly shows the dependency on the resonance frequency for the mass sensitivity. Finally, the geometry and the modeshape of the optimized 1 um thickness variant is shown in figures 3.17 and 3.18, respectively. Again, the 1 um thickness variant has 50 unit cells instead of 15 compared to the models optimized for the Qf product. Most notably, as shown in figure 3.18, the modeshape is of higher order and more localized compared to the other two models as a result of the large number of unit cells. It should be mentioned that Ghadimi et al. have also shown the increased localization of the modeshape as a result of the increased number of unit cells. [5] The increased localization can be explained as each unit cell can contribute the the destruction of the elastic waves in the resonator. As there is a greater number of unit cells, they are also placed closer together which means that the wave will be damped out faster.

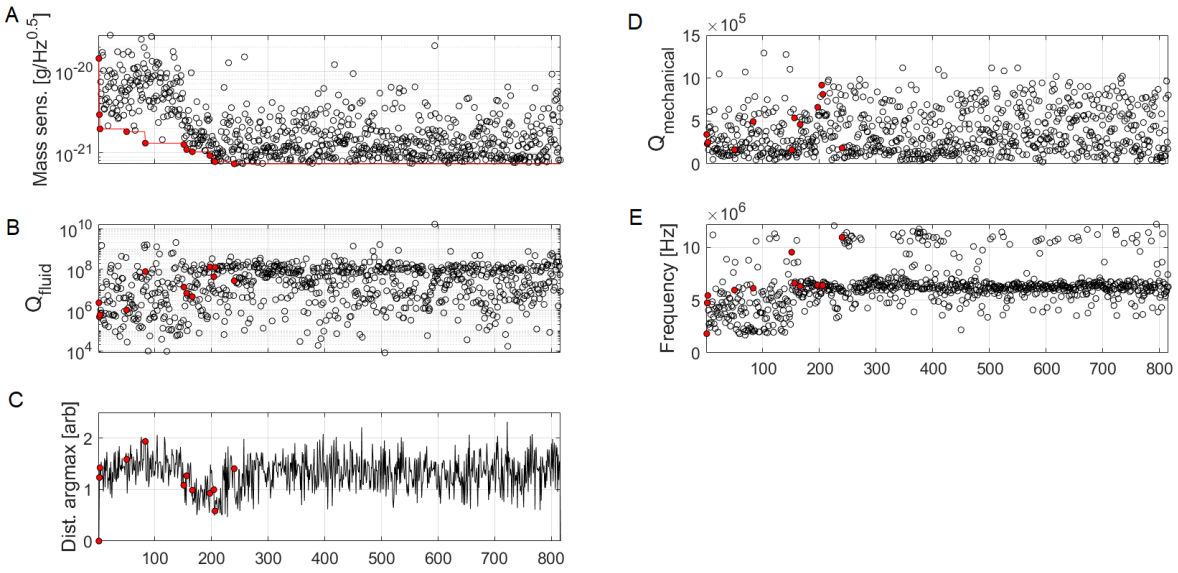

Figure 3.16: The optimization history of the 1 um thickness variant optimized for mass sensitivity.

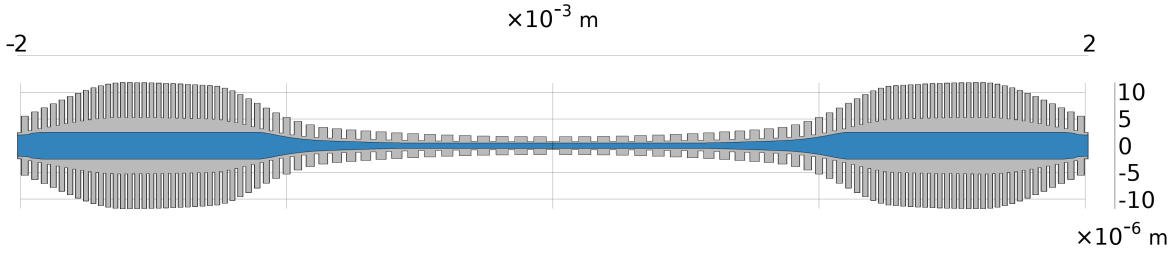

Figure 3.17: A figure of the geometry of the 1 um thickness variant optimized for the mass sensitivity. The microfluidic channel is indicated in blue. The length has been scaled down for presentation purposes to 1:20.

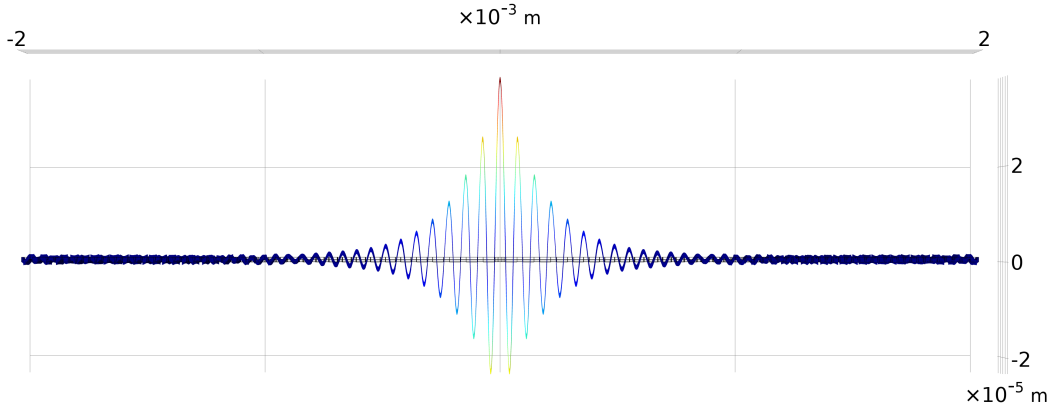

Figure 3.18: The modeshape of the 1 um thickness variant optimized for the mass sensitivity. As can be seen, the modeshape is more localized and of higher order compared to the MDV model optimized for the Qf product.

The optimization history of the 200 nm thickness variant can be seen in figure 3.19. Figure B, which contains the Q_{fluid}, shows similar values as the 1 um thickness variant, even though the channel of the 200 nm thickness variant is smaller. Likewise the resonance frequency shown in figure C is also of similar values compared to the 1 um thickness variant. This is likely due to the identical maximum amount of unit cells and the same resonator length. The mechanical Q-factor is however an order of magnitude higher. One key difference is however that the 1 um thickness variant converged much

faster than the 200 nm thickness variant. Even when it has one extra design variable.

The geometry and modeshape of the 200 nm thickness variant can be seen in figures 3.20 and 3.21, respectively. The 200 nm thickness variant has also 50 unit cells just like the 1 um thickness variant. Interestingly enough, 200 nm thickness variant has a totally different tapering shape and a straight channel as well. The modeshape of the 200 nm thickness variant appears to be even more localized than the 1 um thickness variant. This could a result from the tapering shape as it appears that the modeshape damps out quickly when the resonator gets wider. Again, as the unit cells cause the modeshape to be damped out, it makes sense that when these unit cells are close together this would also happens faster. This is the case near the center of the resonator, exactly when the modeshape dampens out. For example, this is not the case for the optimized 1 um thickness variant which remains very narrow until about a milimeter removed from the center. This could explain the difference in modeshape between the two variants, even when they share the same amount of unit cells. The modeshape of the 200 nm thickness variant also appears to be of lower order than that of the 1 um thickness variant.

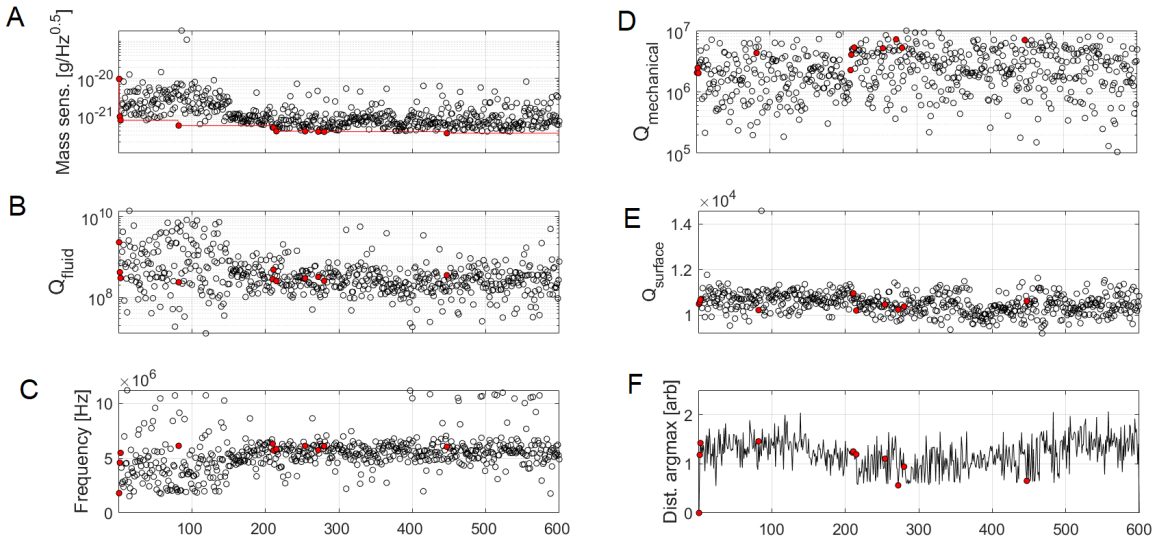

Figure 3.19: The optimization history of the 200 nm thickness variant optimized for mass sensitivity.

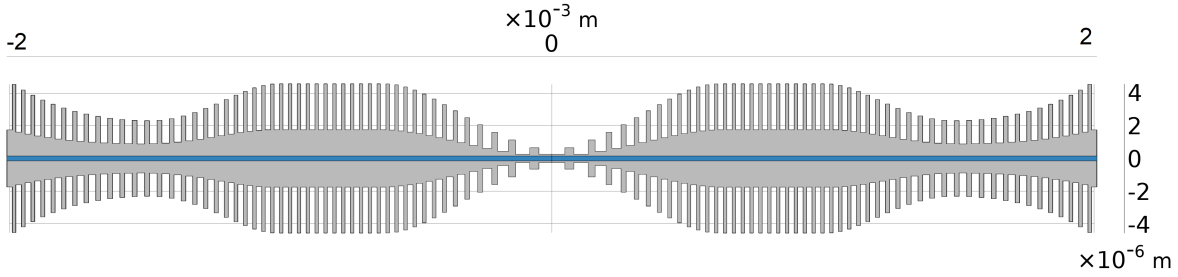

Figure 3.20: A figure of the geometry of the 200 nm thickness variant optimized for the mass sensitivity. The microfluidic channel is indicated in blue. The length has been scaled down for presentation purposes to 1:20.

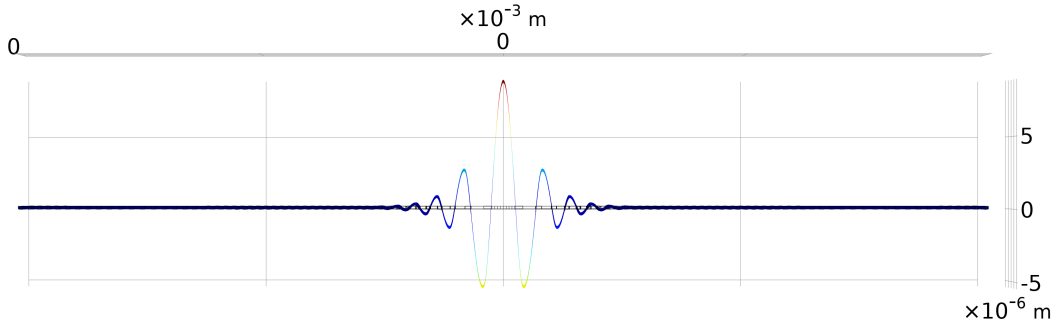

Figure 3.21: The modeshape of the 200 nm thickness variant optimized for the mass sensitivity. As can be seen, the modeshape is more localized and of higher order compared to the MDV model optimized for the Qf product.

3.4. Discussion and Recommendations

The optimization results of the Qf product show that the tapered beam model has a high enough Qf product to enable quantum mechanical experiments at room temperature which is $6 \cdot 10^{12}$ Hz. This is two orders of magnitude higher compared to the SMR design by Manalis et al. [37] As has been mentioned, there are other models that were optimized for the Qf product that perform better but for practical reasons, this is the model that could be chosen to be fabricated. Alternatively, the MDV model could be chosen instead to account for any possible losses in Qf product that may or may not be encountered when the resonator is fabricated as the MDV model offers an even higher Qf product at the same dimensions.

For the mass sensitivity, the 1 um thickness variant of the MDV model optimized for the mass sensitivity offers more than an order of magnitude improvement compared to the same Manalis et al. design, from about 9.5 $\frac{zg}{\sqrt{Hz}}$ to only 0.74 $\frac{zg}{\sqrt{Hz}}$. This translates to a mass sensitivity of about 23.7 zeptograms at a bandwidth of 1000 Hz. This is the same bandwidth used by Manalis et al. [44][21][37] As has been mentioned in the introduction, this is sufficient to replicate the study performed on immunoglobin M, which requires a mass sensitivity of 100 kDa or 0.166 attograms ($1.66 \cdot 10^{-19}$ grams). [32] It could even be sufficient to measure β-amylase measured in a different study with a mass of about 200 kDa. [6] A mass sensitivity of about an order of magnitude lower could then be sufficient to measure this protein individually. Neither of these proteins can be measured by conventional suspended microchannel resonators as they lack the mass sensitivity to do so. It would also mean that the designs presented here could measure even smaller nanoparticles. A recurring kind of nanoparticle is one made from gold. [32][6][37] In the study performed by Naik et al., these golden nanoparticles only have a diameter of about 2.5 nm with a minimum mass of 480 kDa. [6] This would imply a mass sensitivity is needed of about 48 kDa or about 80 zeptograms ($8 \cdot 10^{-20}$ grams) to distinguish the individual particles properly. The 1 um thickness variant of the MDV model has the mass sensitivity to do this. For the sake of comparison, Manalis et al. were able to measure golden nanoparticles with diameters of 10 nm, 15 nm and 20 nm with their suspended microchannel resonator which required a mass sensitivity of about 1 attogram ($1 \cdot 10^{-18}$ gram).

The 1 um thickness variant of the MDV model optimized for mass sensitivity does not exceed the Qf product of $6 \cdot 10^{12}$ Hz, however. In order to get both an order of magnitude improvement in mass sensitivity and the high Qf product for Quantum mechanical experiments at room temperature, the 200 nm thickness variant could be considered instead which does have the Qf product necessary and offers even better mass sensitivity, to only about 10.8 zeptograms ($1.08 \cdot 10^{-20}$ grams) at a bandwidth of 1000 Hz, but fabrication could prove to be more difficult as it is significantly smaller than the 1 um thickness variant. Achieving both the order of magnitude improvement in mass sensitivity and the necessary Qf product for quantum mechanical experiments at room temperature for the 1 um thickness variant might not be impossible however, as intermediate optimization results did indicate that this is possible. The optimization algorithm was not set up to account for this however, and such, none of these iterations were acknowledged as optima by the algorithm. The recommendation is then for future work to try and

fabricate the MDV model, either optimized for mass sensitivity in which case the 1 um thickness variant should be considered, or optimized for the Qf product depending on the usage of the resonator.

It is then important to confirm the findings made here experimentally as this was beyond the scope of this work. Not only with regard to the total Q-factor and whether or not the defect eigenmode shows up at the resonance frequency given by COMSOL but also with regard to the fluidics. For example, it could be possible that the Q-factor could be higher when it is filled with a fluid, as shown by Manalis et al. [43][21][37] The opposite could also be true however, as occurred with the resonator by Craighead et al. whose design performed worse when it was filled with a fluid, even when the theoretical Q_{fluid} predicted was high enough that it shouldn't impact the Q-factor but experiments proved otherwise. [3] Also, while the fluidics of suspended microchannel resonators have been experimented on with higher order modes, this hasn't been done with the defect eigenmode. [1] The fabrication of these resonators could be an issue regardless of the dimensions of the design, as a clear step by step plan to fabricate the resonators was also beyond the scope of this project. Potentially, wafer fusion bonding could be one way to do this but this has not been done with pre-stressed silicon nitride before. Alternatively, a fabrication technique could be used like the one in Craighead et al. where they created a trench and used a sacrificial layer of polysilicon to create a channel within pre-stressed silicon nitride. [3] However, the geometry of the resonators from this thesis is more complicated than the simple rectangular beam from Craighead et al. It should be mentioned however, that the design by Craighead et al. in terms of its height is sub-micrometer with a channel of about 100 nm and has a comparable width. If this fabrication method can be used for millimeter-length devices, this could potentially be one way of fabricating these resonators.

The actual designs can of course also still be improved upon. Even without going to thicknesses of the resonator smaller than 1 micron. An important constraint that was put in place, mostly to ensure that the defect mode could be selected accurately, was fixing the width at the center defect. Fixing it meant that the anti-symmetric mode doesn't show up for example. This is of importance as only one half of the resonator was modeled and COMSOL doesn't allow for both the symmetry condition and anti-symmetry condition to be selected at the same time. Accounting for this in the Matlab code could be quite challenging but it would allow even more unique geometries. The total length could also be increased for example, which could also increase the Q-factor albeit at the cost of the resonance frequency. It would then be interesting to see if this also leads to improved performance overall. For either the tapered beam model or 1 um thickness variant of the MDV model, it could prove useful to perform multi-objective optimization with both the Qf product and the mass sensitivity. This to ensure that the Qf product is sufficiently high while getting a high mass sensitivity at the same time as this is not a given result from the optimization as shown before but it could be achieved. It should also be mentioned that since the MDV model has so many design variables, it can't be conclusively said that there does not exist a combination of design variables with an even higher Qf product or mass sensitivity. Finally, higher order defect modes could also be looked at. A small test on a single model seemed to imply that, while the resonance frequency increases significantly, this doesn't weigh up against the decrease in Q-factor at the same time. Not even for the mass sensitivity which scales with Qf^2 as for the model checked, the resonance frequency doubled while at the same the Q-factor decreased by a factor of ten. It could be possible however that this does not hold up for all geometries and so it also deserves a closer look.

Conclusion

This thesis introduced a novel suspended microchannel resonator design with two orders of magnitude improvement in Qf product and one order of magnitude improvement in mass sensitivity compared to earlier designs. Most notably, the resonator design by Manalis et al. which has the highest performance to date.[37] The Qf product of the designs exceeds the value that allows for quantum mechanical experiments at room temperature, $6 \cdot 10^{12}$ with similar dimensions as the resonator design by Manalis et al. (2014) [29] For the mass sensitivity, it means that the design could potentially directly measure individual immunoglobulin proteins as the mass sensitivity of the 1 um thickness variant of the MDV model is about 23.7 zeptograms at a bandwidth of 1000 Hz. [32] Both the Qf product and the possibility of measuring single proteins has not been reported for suspended microchannel resonators in the literature. The use of Bayesian optimization for both the Qf product optimization and mass sensitivity optimization has resulted in different kinds of designs in the case of the MDV model. This enabled the performance as discussed and resulted in designs tailored for each performance parameter. The 1 um thickness variant of the MDV model does not provide both the high Qf product and the one order of magnitude improvement in mass sensitivity however, at least according to the final optimization results. The smaller, 200 nm thickness variant does offer both at the same time albeit at the cost of also being more difficult to fabricate.

This is possible due to the use of pre-stressed silicon nitride which causes an effect called dissipation dilution. This dissipation dilution reduces the losses of the system comparatively by increasing the stored energy in the system. This is also a rather new concept for suspended microchannel resonators as it has only been reported once in the literature in a paper by Craighead et al. [3] However, contrary to the resonators in this thesis, it did not result in a higher Q-factor of the resonator. This is likely due to clamping losses and so the solution to that problem is eliminating those losses with the help of soft-clamping which constrains the modeshape to the center of the resonator. As has been said, soft-clamping consists of phononic crystals which prevent elastic waves from moving through the resonator in the phononic band-gap. The combination of dissipation dilution, soft-clamping and also strain engineering, which is the tapering of the resonator to increase stress at the center, results in very high Q-factors. This was first reported by Ghadimi et al. for regular nanomechanical resonators. [5] This thesis is the first to combine these features for suspended microchannel resonators with the before mentioned increases in Qf product and mass sensitivity as a result. Of course, it is important to mention that this thesis is purely based on FEM results, and so it is necessary to confirm the findings by fabricating the designs and testing them experimentally.

Reflection

At the end of the project, it is also important to reflect on it. Personally, I found this project to be very interesting, maybe even more so than initially thought. Before the start of this project, I believe I have encountered suspended microchannel resonators before but I've never really delved into the subject as was necessary for the project. The idea of these tiny nanoscale channels was really intriguing. It proved to be necessary to learn a lot not just about suspended microchannel resonators but also on nanomechanical resonators as a whole and phononic crystals in a short time which was really challenging. For the thesis, the way the energy dissipation worked was especially difficult and also time consuming. Luckily, I was already familiar with Comsol which has been a constant presence throughout this project as it is completely FEM based.

Even though the results that have been obtained are really good and show great promise for these kinds of new SMRs, I think one of the things that bothered me was the fact that performing experiments wasn't possible in the time frame allotted for a Master thesis. As the geometry of these resonators for SMRs is quite novel, there is no straightforward way to manufacture them. This really needs to be looked into in depth and so doing the preparation work necessary to fabricate them in the first place and also performing experiments proved to be too much. It was decided early on to not fabricate them and instead focus more on the optimization and having greater variance in the geometry of the designs. I had personally hoped for quite some time that it would still be possible to at least include a kind of blueprint to fabricate these resonators and present a clear, straightforward plan but as certain parts took longer than initially expected, this too was abandoned. I think that especially that last part is the greatest regret I have regarding this project.

Another point of interest was the discussion about what to do with the calculation of the Q_{fluid}. Initially, this was thought of actually trying to simulate the fluid flow inside the microchannel and so a lot of time went into thinking up ways to do this accurately. Doing these kinds of fluid flow calculations in matlab for vibrating devices can be quite tricky but in the end it was decided that it wasn't necessary to perform the fluid flow calculation as the solution was found in the rate of strain equations by Sader et al. The Comsol simulations also required a lot of trial and error to get right. Sometimes it proved difficult to rid of certain errors, especially with regard to meshing. At times I also could be too eager to get a new version of the models up and running which could also result in errors and required me to go bug hunting within the Matlab code. This was especially a concern halfway through the project as new versions of models were created in a relatively short time span. Had I taken more time to check the code for bugs, this process might have gone over quicker. Later on I did get better at this even though at the last stages of the project, the models could still change quite a lot. The research cluster was very helpful in getting the results, but there were times when certain errors were caused by the cluster. A persistent one was when the Matlab code could not connect to Comsol. Even after introducing error handling to take care of this, this could still occur. The result of this error is a faulty iteration in the machine learning algorithm which is an especially annoying thing to happen. However, in the final simulations these errors did disappear so it would seem that the error handling did work after all.

Finally, messaging and presenting the material was brought up by my supervisors as a point of improvement. I have had difficulty to cut down the amount of models to a minimum for the sake of clarity and messaging. Most likely because I've worked with these models for as long as I did. Initially I especially regretted getting rid of the 200 nm thickness variants of the Qf optimization as they offered the highest performance and moving the data to the appendix felt like getting rid of it entirely. Of course, my supervisors were right and I had trouble explaining even four different models in one table. The end result is that the message will be clearer and easier to understand as there are only two models

for each optimization objective. I don’t think the worth of the research is necessarily less for it and it will be easier to present this material during the defense as well.

A

Investigating Unit Cell Geometry

In order to model the suspended microchannel resonators properly, the phononic band-gap diagrams were looked into first. As has been explained in paragraph 1.3, the phononic band-gap consists of a frequency range in which no eigenmode is present. The band-gap is necessary to achieve soft clamping by localizing the modeshape to the center of the resonator and reduce/negate the energy losses associated with clamping. To our knowledge, the phononic band-gap hasn't been explored in suspended microchannel resonators prior to this work as phononic crystals also haven't been used with SMRs before. For this purpose, and for modeling the resonators later on, two designs have been chosen: a model with the channel on top of a plate resonator and one where the channel is embedded within the resonator. These are shown in figures A.1 and A.2. They will be referred to as the center height model and equal height model respectively. The phononic band-gap diagrams have been created using COMSOL which uses the 3D solid mechanics physics to acquire the eigenfrequency of a single phononic unit cell. The study also includes a parameter sweep of the wavenumber to calculate the eigenfrequencies for that corresponding wavenumber. For the eigenfrequency analysis the phononic unit cell has a periodic condition on each end to simulate a whole sequence of unit cells with just a single one. The study also include a stationary step to calculate the stress of the unit cell. This is necessary because the unit cell is pre-stressed. The stationary step has two fixed constraints on each end of the unit cell instead of the periodic condition. The raw data with the eigenfrequencies and wavenumbers is then extracted to Matlab which is used to draw the phononic band-gap diagrams.

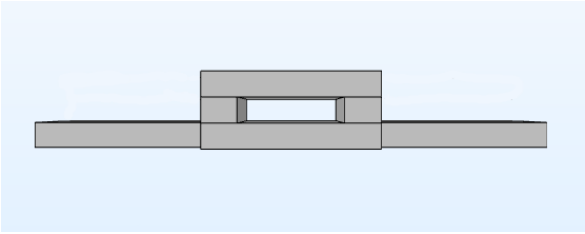

Figure A.1: A cross-sectional view of the center height model.

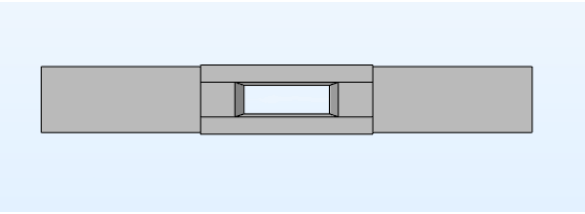

Figure A.2: A cross-sectional view of the equal height model.

The center height model, named such in reference to the increased height of the center beam compared to the side wings, was considered first as it is the result of simply putting a channel on top of a conventional nanomechanical resonator. As an introduction, the overall band-gap diagram will be discussed first. This overview is displayed in figure A.3 and the six eigenmodes within this frequency range are indicated as small pictures of the modes in question. The dimensions of this model are the same as that of the straight beam design by Ghadimi et al. As explained in section 1.3 on Phononic Crystals, the axes of a phononic band-gap diagram are the frequency on the y-axis and the wavenumber on the x-axis. The first two eigenmodes are the in and out-of-plane nodal modes of the first eigenmode

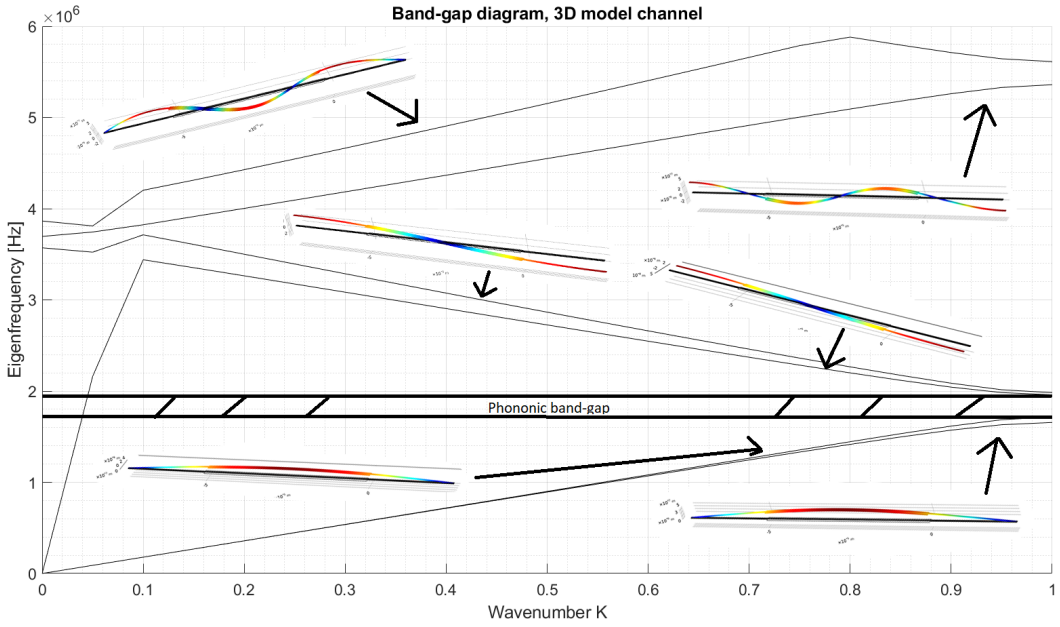

Figure A.3: The band-gap diagram of the 3D channel model with the eigenshapes indicated.

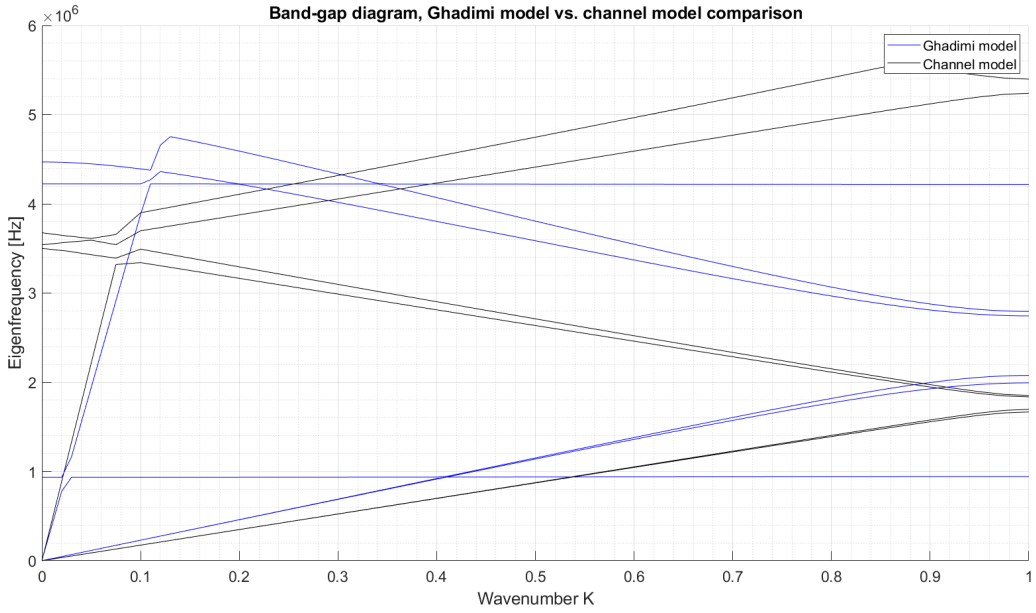

Figure A.4: A band-gap diagram of a comparison between the Ghadimi model and the channel model.

and the two modes after that are the anti-node modes of the first eigenmode. The band-gap is located between the node and anti-node mode of the first eigenmode with a frequency range of about 1.7 MHz and 1.95 MHz. The two remaining eigenmodes are of higher order. The eigenmode that seems to be traveling through the phononic band-gap is the fundamental eigenmode. The fact that this mode is traveling through the band-gap doesn't impede the function of the band-gap as the fundamental mode won't appear in the resonator itself because the fundamental mode is translational and the resonator is clamped at both sides.

It should be noted that the phononic band-gap of this model is quite small; it only has a bandwidth of about 0.25 MHz compared to the band-gap of the resonator by Ghadimi et al. of about 0.6 MHz.

This diagram can be seen in figure A.4 in blue together with the channel model indicated in black. The Ghadimi model is based on the straight beam design by Ghadimi et al. and was recreated in COMSOL in the same manner as the two channel models. The phononic band-gap of the Ghadimi model is enclosed by the same eigenmodes as the channel model. The difference between the two band-gap diagrams is mainly that the band-gap is bigger than that of the channel model and that the two other eigenmodes in this frequency range are two torsional eigenmodes instead of two eigenmodes of higher order. Due to the addition of the channel, the torsional modes have shifted to higher frequencies. This can be explained by the increased moment of inertia due to increased mass in the height direction because of the addition of the channel. This can be confirmed when looking at in-between values for the channel height. A figure like figure A.3 of the Ghadimi model is included in the appendix. Another important consideration is the difference in how the internal stress is applied. In the Ghadimi model, it can be assumed that the internal stress is applied evenly throughout the unit cell as it simply consist of a single layer of silicon nitride. In the channel model, this might be a bit more complex as it is unclear how the internal stress would work at least as far as the channel part on top of the rest of the resonator is concerned. For that reason the internal stress is only applied at the bottom of the resonator.

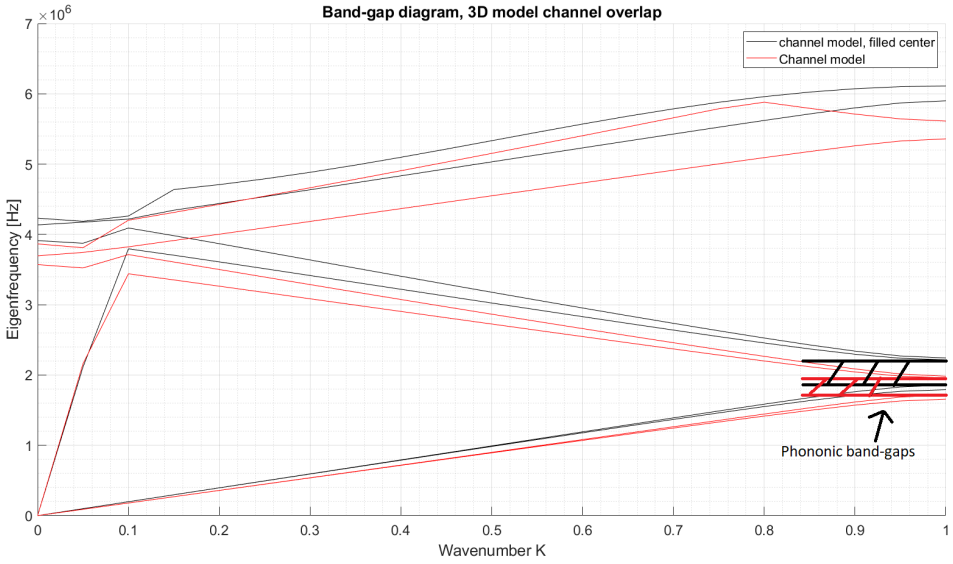

Figure A.5: A figure of the comparison between the channel model and the channel model with a filled center.

The small bandwidth of the phononic band-gap of the channel model can be a limiting factor when trying to optimize the resonator. The next section will discuss how the band-gap changes with the shape of the unit cell. First, a graph comparing the channel model with and without channel will be discussed. This graph is displayed in figure A.5. To make a fairer comparison between the filled and channel model, the internal stress has been applied throughout the unit cell in contrast to the graphs shown before where the stress is only applied on the bottom part. This is done so because otherwise the result would reflect negatively on the filled model due to the extra mass that doesn't have internal stress. This graph reflects purely the presence of the channel itself. The channel mainly causes a decrease in frequency of all eigenmodes. As a side effect this can also be seen in the band-gap itself. The band-gap is also smaller in the graph with the channel. This difference can mostly be explained by the applied internal stress. The eigenfrequency generally goes down with increased mass but figure A.5 shows the opposite; The model with the filled center has both higher eigenfrequencies and a wider band-gap while also having a higher mass. Internal stress can give the opposite effect which means higher eigenfrequency which explains the effect shown.

Next, the diagrams will be used to illustrate what happens to the band-gap when certain variables are changed. These variables are indicated in figure A.6. First, the channel height will be varied. In this model the top wall of the model will be kept 50 nm. This graph can be seen in figure A.7. It shows that the band-gap gets smaller and the eigenfrequencies will be lower with increasing channel height. The full parameter sweep for this variable continues up to 1 micron and this inclination does continue until

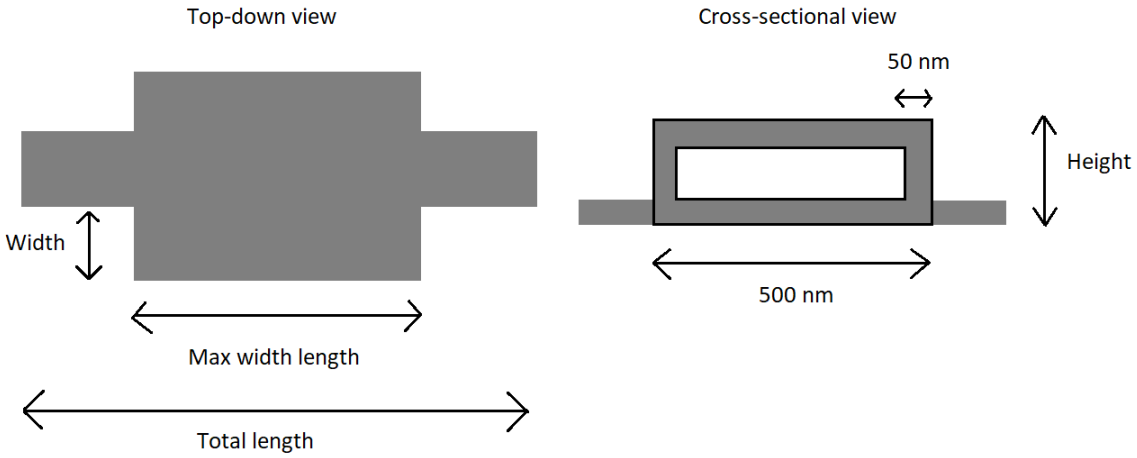

Figure A.6: A figure that provides an overview of the different parameters that have been varied.

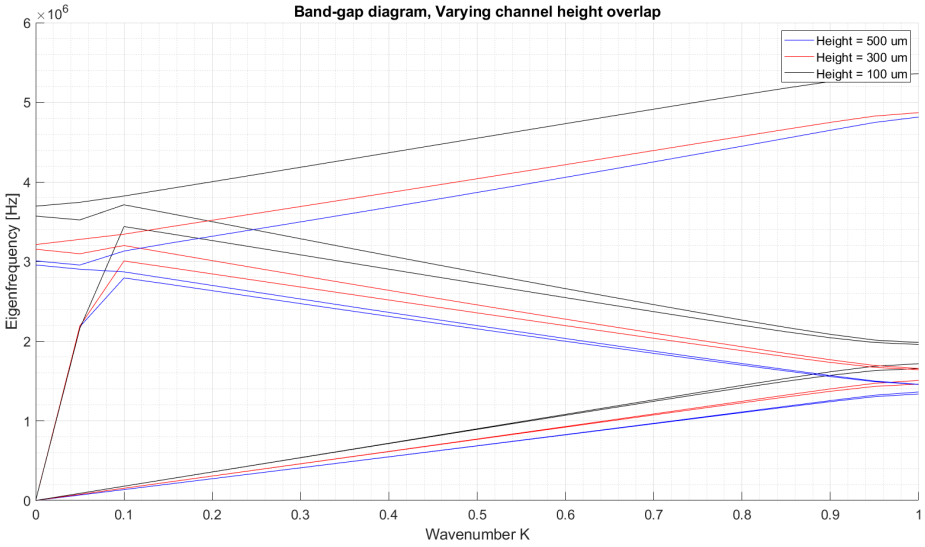

Figure A.7: A phononic band-gap diagram where the height of the channel is varied.

the band-gap disappears at about 800 nm. The explanation for this phenomenon is slightly different than that of figure A.5. Even though the volume over which the internal stress is applied does increase with a higher channel height, this effect appears to be outweighed by the sheer increase in mass itself. It should be noted however, that Reetz et al. concluded that an increase in mass contrast, like it happens here, should increase the phononic band-gap bandwidth instead of decreasing it as we see here. [13] The graph implies that only the increase in mass plays a significant role in how the band-gap is shaped as far as varying the height of the channel is concerned.

The next parameter that will be looked into is the width of the wings. Increasing this parameter also increases the mass contrast and from figure A.8, it can be seen that increasing the width also increases the bandwidth of the band-gap as predicted by Reetz et al. [13] Once again, the bandwidth becomes small enough that placing the defect mode within the band-gap could be cumbersome and that optimizing for these low values of the wing width can prove difficult. Finally the last parameter is the length-wise width of the wings. This parameter is set on a scale with scale = 1 meaning that the wings are exactly half as long as the entire unit cell. Once again, the band-gap diagram behaves according to theory stipulated by Reetz et al., as the bandwidth of the band-gap is determined by the mass contrast

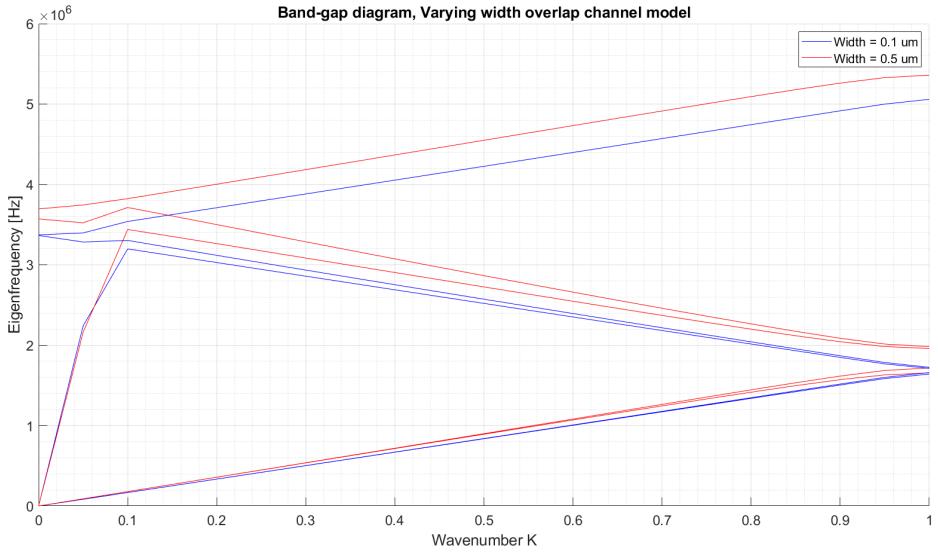

Figure A.8: A phononic band-gap diagram that compares different values of the width of the wings of the center height model.

of the unit cell. This time though, the mass contrast has two minima, one when the wing encompasses almost all of the unit cell and the other when the wing is very small. The biggest mass contrast lies in the middle and it can also be said that for values of the scale that are around 1 the band-gap remains mostly similar in bandwidth. This is illustrated in figure A.9. Values beyond the range displayed in the figure will cause the band-gap to shrink and eventually to disappear again. The final thing to note is that the frequency range of the band-gap is also mass dependent with the heavier model, the one with scale = 1.3, having a lower frequency range than the two other models shown which are lower in mass due to the wings being smaller.

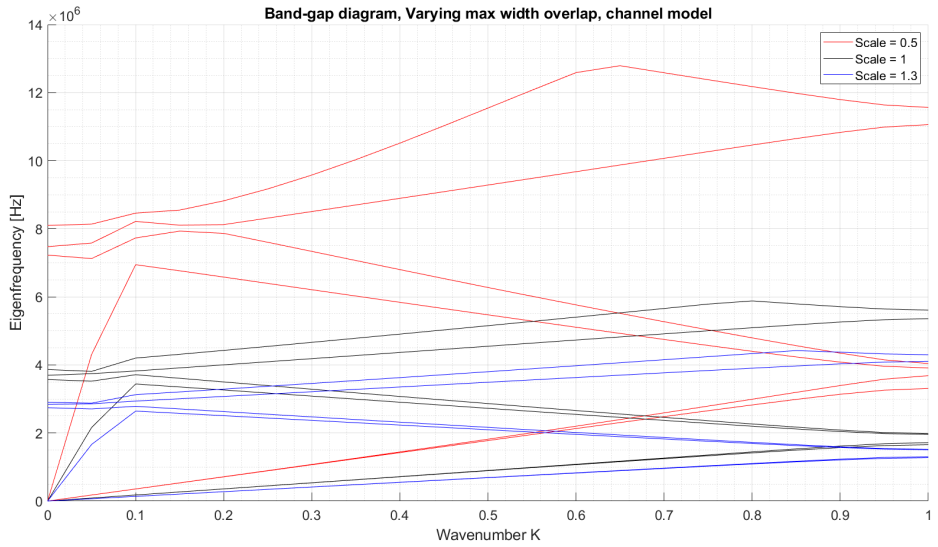

Figure A.9: A phononic band-gap diagram that compares different values of the length-wise width of the wings of the center height model.

At this point it has become clear that the center height channel model comes with some strings attached. The band-gap size is highly sensitive to any changes in the model due to the fact that the mass contrast can also change quickly when any adjustments are made. The baseline version of the model already has a small band-gap which means placing the defect mode within the band-gap could be tricky, especially when the resonator needs to be filled with a fluid before it can be used and when

both the fluid and a sample will also cause the defect mode to shift to lower frequencies. So what about the second design, the equal height model shown in figure A.2? At first the second design was thought of as being impractical and too heavy to be used but the phononic band-gap diagrams that have been created of this model have shown that this is not the case. A comparison between the center height model, the model discussed first, and the second model, also called equal height model as the wings are as thick as the center part, can be found in figure A.10. The figure contains three different models. The center model, the equal height model with a similar stress configuration as the center model, which means that stress is only applied on one slice of the model, and the equal height model with stress applied throughout the unit cell evenly. As can be seen for the figure, both versions of the equal height model have a substantially increased band-gap bandwidth compared to the center height model. Furthermore, the equal height model with stress applied throughout the model also has an increased frequency range and is in this regard and the band-gap size very comparable to the phononic band-gap from the Ghadimi et al. design shown in figure A.4. Seemingly, the addition of the channel doesn't appear to have a major impact on the phononic band-gap in the equal height model. However, that is only the case when stress is evenly distributed in the resonator which could prove to be difficult to fabricate.

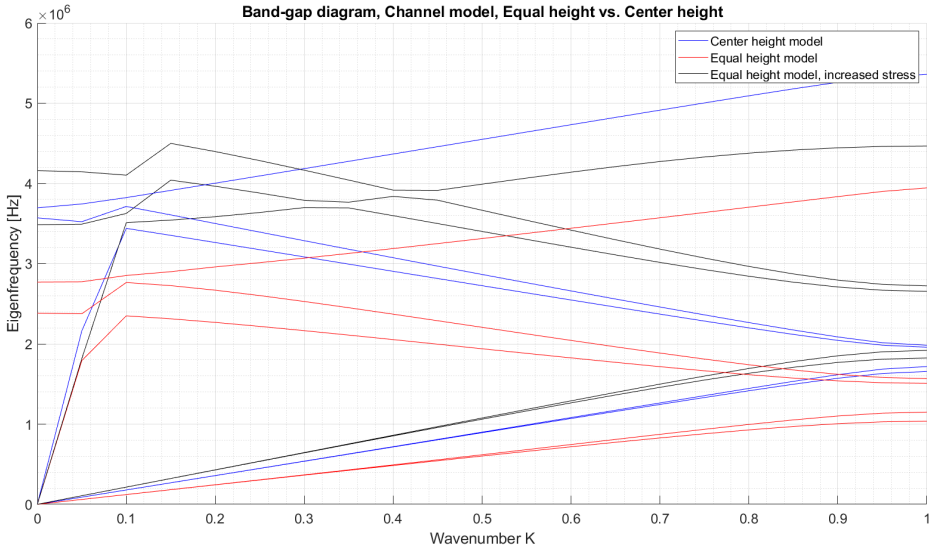

Figure A.10: A figure that visualizes the difference of the center height model and the equal height model.

The benefits of the equal height model also extend to varying the individual parameters. For the sake of simplicity, all figures discussed hereafter have the internal stress applied to the entire resonator in the case of the equal height model. A good example of one of these benefits is when the height of the unit cell is varied. A comparison between different heights of the equal heights model can be found in figure A.11. In contrast to figure A.7, which shows the height variation of the center height channel model, the equal height model has very similar band-gap bandwidths and frequency ranges between the models shown in the figure. This would imply that it would be much easier to scale the model up as the band-gap remains sufficiently large. Figure A.11 can be explained by way of the mass contrast between the wings and the center beam of the resonator staying roughly the same as the resonator increases in height. The frequency range of the phononic band-gap does decrease slightly over this range of resonator heights but not nearly as much as was the case with the center height model. This is because the increase in mass is counteracted by an increase in volume over which the internal stress is applied.

These same kind of changes can also be seen with the width and max width length design variables. These can be seen in figure A.13 and A.12 respectively. Most notably, the bandwidth of the phononic band-gap stays bigger in the equal height model versus the band-gap of the center height model for the same widths. This allows for a bigger range of values to be of practical use in the equal height

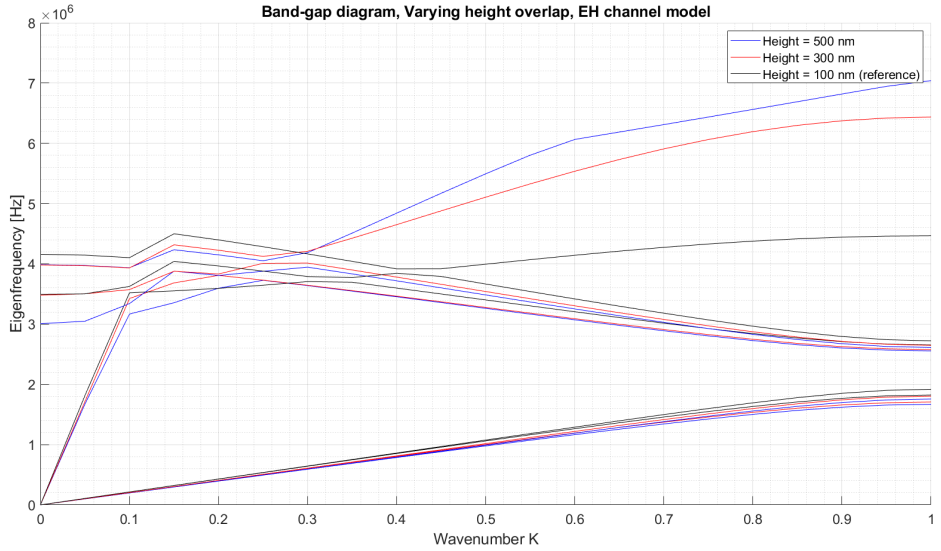

Figure A.11: A phononic band-gap diagram that varies the height of the channel of the equal height model.

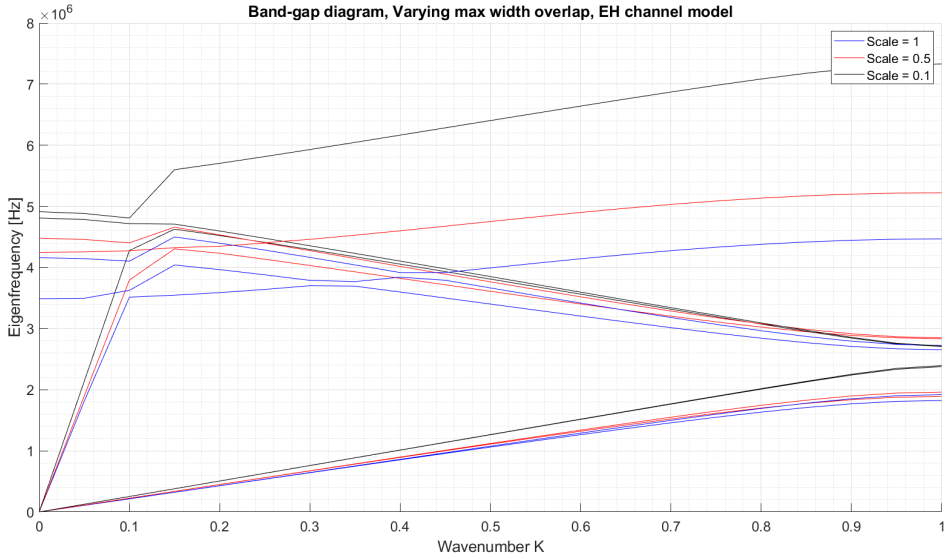

Figure A.12: A phononic band-gap diagram that compares different values of the length-wise width of the wings of the equal height model.

model. Another interesting thing to note is that with a smaller width the frequency range is higher in the equal height model than that of the center height model. A plausible explanation for this is once again the internal stress that's applied to the entire of the equal height model versus it only being applied to the bottom plate of the center height model. The max width length comparison in figure A.12 shows similarities to figure A.11 when different heights of the equal height model were compared. The phononic band-gap bandwidths and frequency ranges are more comparable in size and the band-gaps are also wider in general. Another thing is that the equal height model doesn't suffer from the effect where the in-plane and out of plane modes of a single mode would grow apart and so decrease the bandwidth of the band-gap. Instead, these modes stay more together which results in a wider band-gap as can be seen for scale = 0.5 of the equal height model in figure A.12. Scale = 0.1 for the equal height model is also still ”coherent” and could potentially be used as a value when the resonator is optimized. In the center height model, the separation of the modes continues to such a degree where

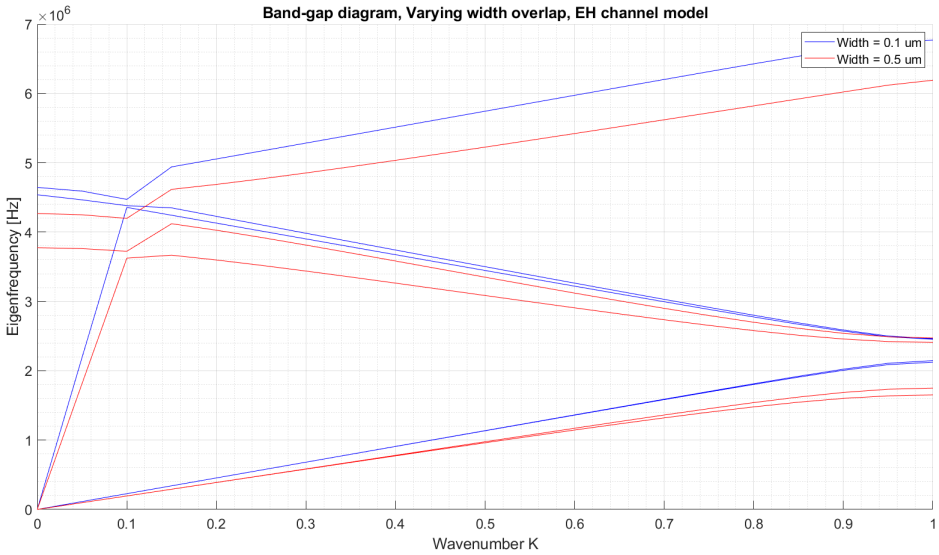

Figure A.13: A phononic band-gap diagram that compares different values of the width of the wings of the equal height model.

the band-gap has completely disappeared.

In conclusion, in this section the phononic band-gap diagrams of the channel models were discussed. Four parameters were chosen to be looked into by performing parameter sweeps on them. Out of the two channel models presented, the equal height model, shown in figure A.2, has proven to be more versatile and generally has a phononic band-gap that is wider than the competing design, the center height model shown in figure A.1. This to such a degree that the bandwidth of the band-gap of the equal height model is comparable in width and range to the uniform unit cell design by Ghadimi et al. which doesn't have a channel. The main reason for the better performance of the equal height model is that the mass contrast between the center beam and the "wings" remains more consistent and is generally bigger in this model. The effect of the mass contrast on the phononic band-gap has been explored by Reetz et al. [13] As the equal height model has shown to be favorable to the center height model, it will be used in the resonator design itself.

B

Convergence check of the 200 nm thickness variant

For the 200 nm thickness variant, the situation is a bit different compared to the 1 um thickness variant. As the dimensions are more extreme compared to the 1 um thickness variant, the number of degrees of freedom needed to accurately model these resonators and so also the computation time are considerably higher for the 200 nm thickness variant. According to figure B.2, in the worst case, the computation time is more than 4000 seconds which is about an hour, with about 11 million degrees of freedom. For the sake of comparison, for the 1 um thickness variant the longest computation time is about 700 seconds with about 2.5 million degrees of freedom. Ideally, the computation time should be about 1000 seconds, or lower which is indicated by the transparent blue surface. Once again, figure B.1 tracks the mechanical Q-factor on the z-axis and as was the case with the 1 um thickness variant, the convergence of the Q-factor appears to be good for this variant as well, as the figure displays similar values for the Q-factor across most of the surface except for low values of the length-wise element ratio as was also the case for the 1 um thickness variant. The jump in computation time and number for degrees of freedom near the top of the surface can be explained by the fact that for these small values of the minimum element size COMSOL allocates additional elements in the z-direction. As this applies to the entire model, this concerns a very large number of elements and so also increases the number of degrees of freedom by a lot. A good balance between convergence and computation time for this model is found to be at 0.25 for the length-wise element ratio and 0.225 um as the minimum element size. Lower values of the element ratio are avoided for the reasons mentioned earlier and 0.225 um offers an acceptable computation time.

Figures B.3 and B.4 display part of an unit cell of the 200 nm thickness variant. Here, the addition of an element in the z-direction can be seen between figures B.3 and B.4 which was responsible for the increase in computation time and number of degrees of freedom mentioned earlier. When the minimum element size is set to 0.25 um, it also gets rid of another element in the z-direction. It does seem that the number of elements in this direction does not have a noticeable impact on the convergence of the Q-factor of the 200 nm thickness variant shown in figure B.1.

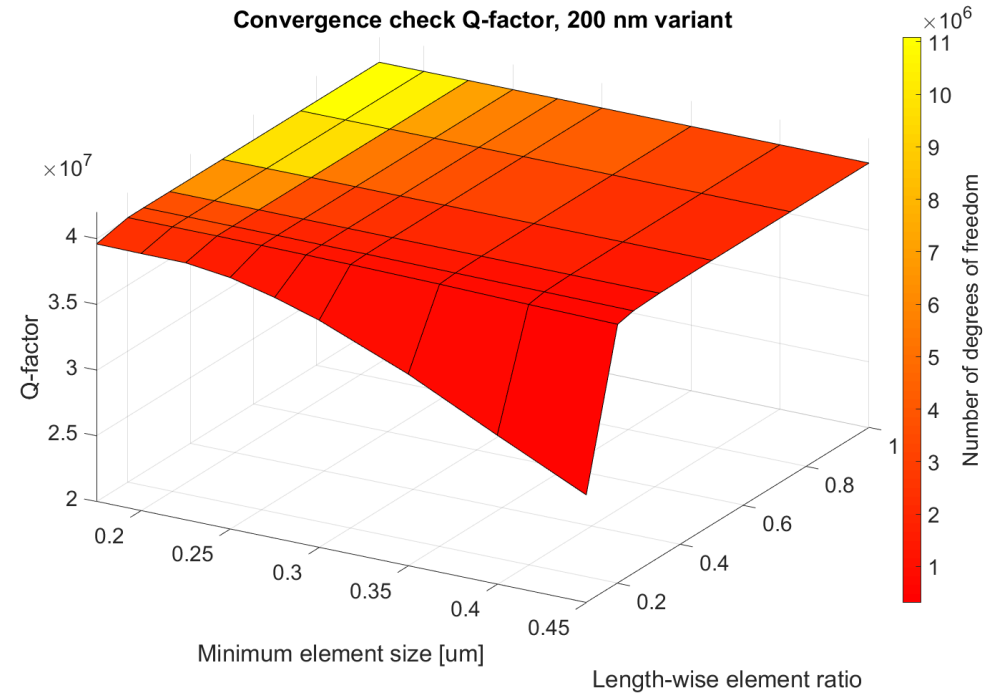

Figure B.1: The convergence check plot of Q-factor. The model is the 200 nm thickness variant of the tapered beam model.

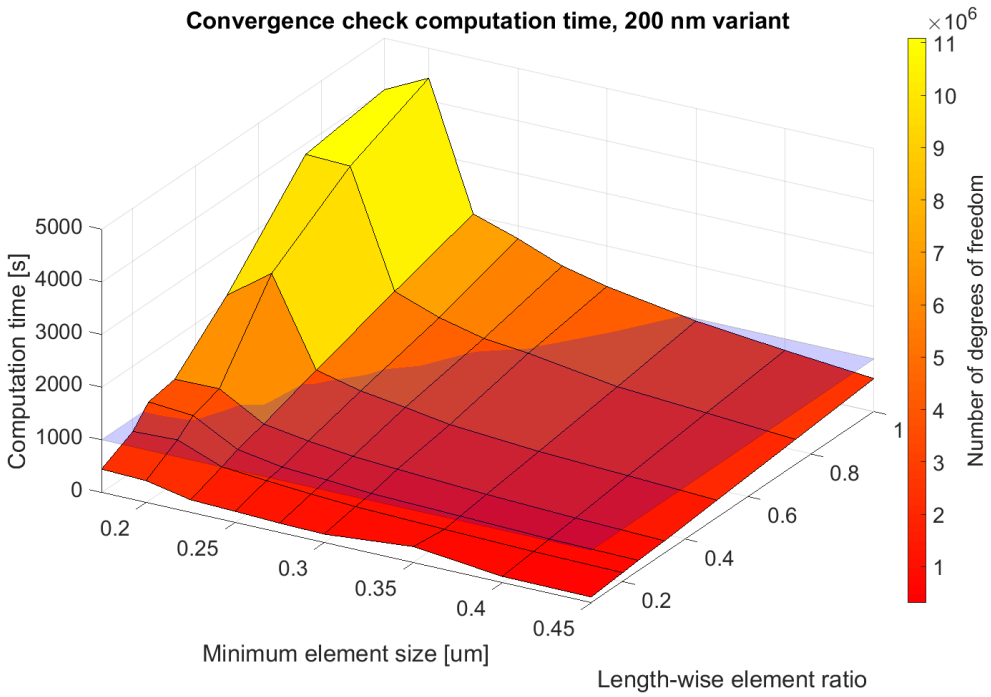

Figure B.2: The convergence check plot of the computation time. The model is the 200 nm thickness variant of the tapered beam model.

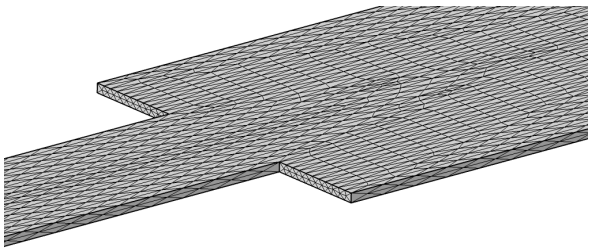

Figure B.3: An image of an unit cell of the 200 nm thickness variant which shows the mesh of the model. Here the minimum element size is set to 0.2 um.

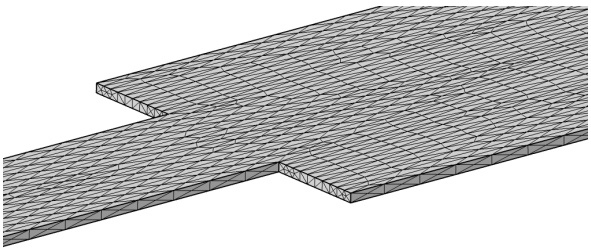

Figure B.4: An image of an unit cell of the 200 nm thickness variant which shows the mesh of the model. Here the minimum element size is set to 0.225 um.

C

The Uniform Unit Cell Model

The so-called uniform unit cell model which, maybe a bit self-explanatory, has phononic unit cells of equal length and equal width. The number of unit cells is fixed at 15 as is the length of the resonator at 4 mm plus the length of the defect. The Uniform Unit cell model has three design variables which are based on the variables that were varied upon in Appendix A: the width and length of the ”wings” of the unit cell and the length of the defect. The uniform unit cell model is shown in figure C.1. The design variables of this model are also shown in the figure together with relevant parameters. These parameters include the fixed thickness of the design at 200 nm, the minimum width fixed at 1 micron and the thickness of the channel walls, fixed at 50 nm. This leaves the channel dimensions which are 900 nm in width and 100 nm in height.

The optimization history of the uniform unit cell model is shown in figures C.2 and C.3. The scatter plot clearly shows a very strong correlation between defect length and Qf product as Qf products higher than about $8 \cdot 10^{12}$ Hz are limited to very small values of the defect length. Interestingly enough, defect lengths larger than about 2e-5m instantly mean much lower values of the Qf product. This strict localization can't be observed in the tapered beam model. There does appear to be a localization of iterations around the optimum point as has been observed before as well. Figure C.3 shows once again that the algorithm is able to quickly find new localized optima after the 20 initialization points, even faster than for the tapered models. This could possibly be because of the strong dependence on the defect length of the model which could effectively reduce the design space. The distance between the optima also shows the close clustering of new optima points. It does appear the case that the algorithm does look for global optima afterwards, however. Another curious observation can be made which is that there appears to be certain iterations with extremely low mechanical Q-factor which sometimes also have much larger resonance frequencies. This still results in a low Qf product and so should not impact the validity of the results however. It is possible that for some of these iterations the defect mode is not selected or does not exist in that case. The correlation between resonance frequency and high Qf product doesn't appear as most iterations have a very comparable resonance frequency. The Q_{fluid} also appears to be around similar ranges when compared between iterations. Curiously, and in contrast to the tapered models, there does seem to be some correlation between high mechanical Q-factor and high $Q_{surface}$ as a lot of the optima also have high $Q_{surface}$ values. The $Q_{surface}$ is also occupies a larger range of values compared to the tapered models. It could be possible that the $Q_{surface}$ is dependent on the defect length as the optima have both a low value of the defect length and a high $Q_{surface}$.

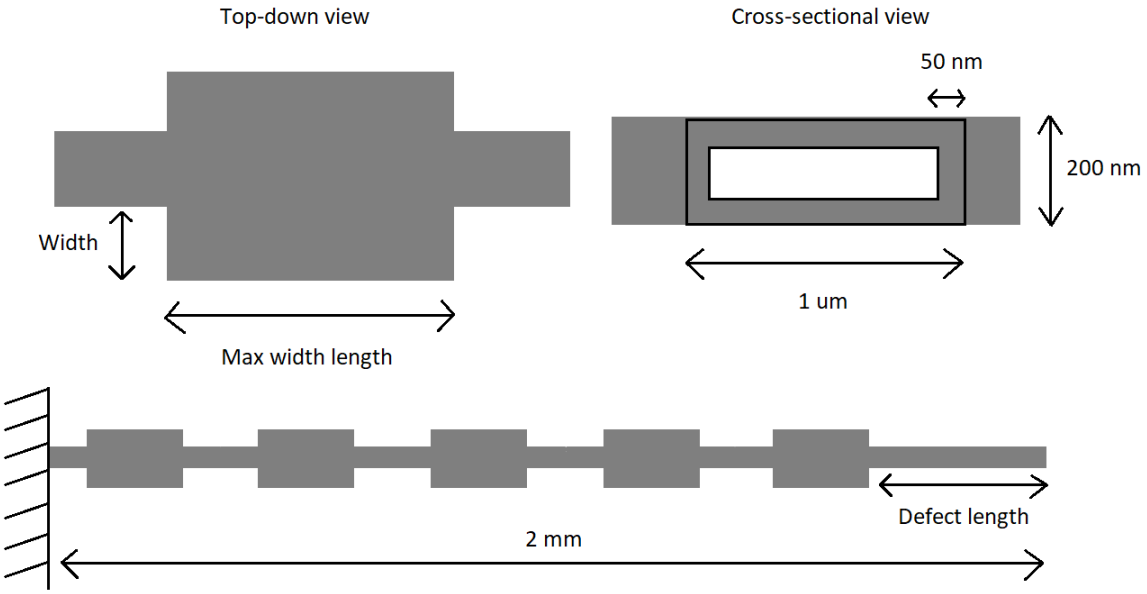

Figure C.1: An overview of the uniform unit cell design.

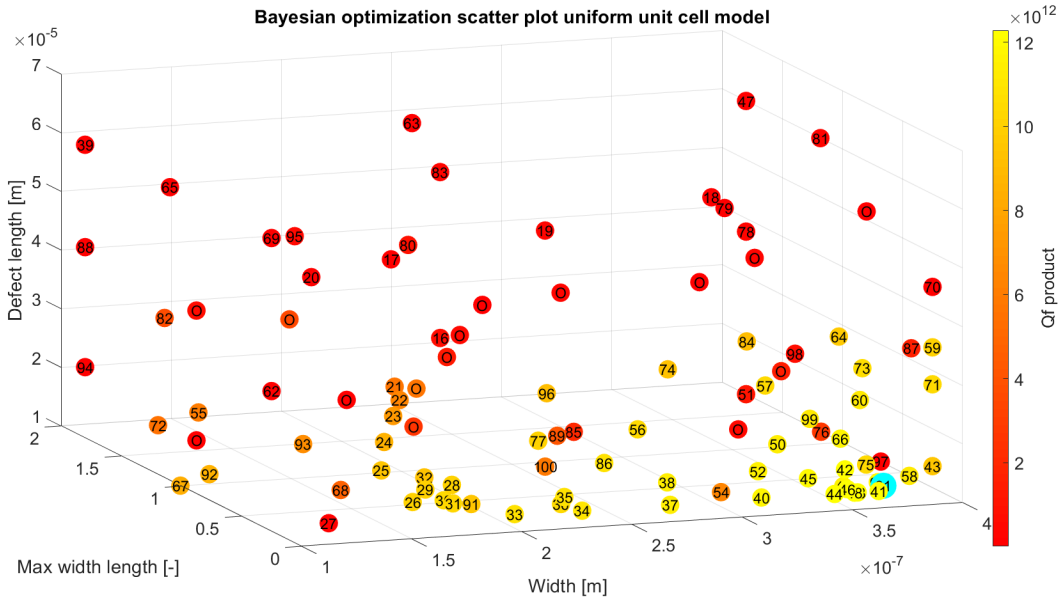

Figure C.2: A figure of the scatter plot of the uniform unit cell model with the three design variables as the axes. The color indicates the Qf product.

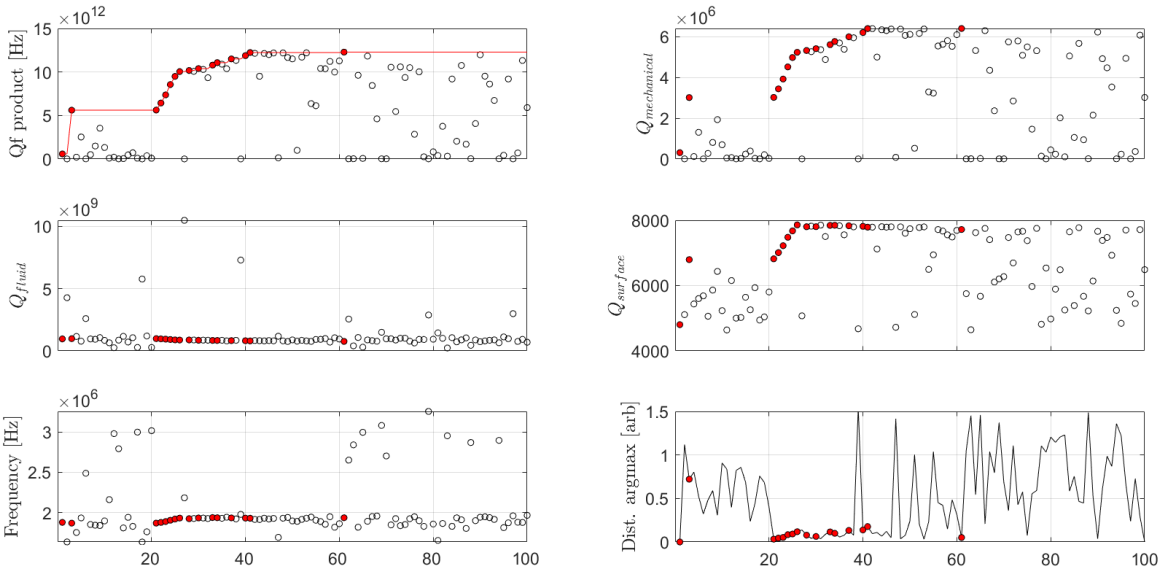

Figure C.3: The optimization history of the uniform unit cell model.

D

Assorted tables and figures

Q-factor Optimization

Interestingly enough, the tapered beam model has a lower Qf product when optimized for the Qf product rather than when the Q-factor is optimized as was done in earlier models. The difference is 0.2e12 Hz. The Q-factor optimization results are found in table **??**. The reason for this is likely that the algorithm tries to maximize both the Q-factor and the resonance frequency at the same time but the design space doesn't explicitly contain design variables that impact the frequency substantially, as the resonance frequency of these optimized results is also highly similar. The end result is a Q-factor that is not as high as it can be and a resonance frequency that's similar between optimizing for Q-factor and Qf product which translates to a lower Qf product when optimized for it.

	Total Q-factor	Frequency [MHz]	Qf product	Mass sensitivity [$\frac{zg}{\sqrt{Hz}}$]
TBM, 1 um thickness variant	4.06e6	1.55	6.3e12	4.62
TBM, 200 nm thickness variant	40.10e6	1.45	5.8e13	1.87
Uniform unit cell model	10.01e6	1.94	1.94e13	3.73
Manalis (2014)	15000	2.89	4.3e10	9.49

Table D.1: A table of the optimization results of the total Q-factor as performed in earlier versions of the thesis. Note how the models offer a slightly higher Qf product. The tapered beam model has been abbreviated to TBM.

Surface Q-factor comparison

Table D.2 compares the $Q_{surface}$ of the models with and without taking the channel walls into account. The table contains the the tapered beam model which is discussed in chapter 3 and the uniform unit cell model found in the appendix. It also contains a model that has the dimensions of the uniform unit cell model but without the phononic crystals. All models are actuated in the defect mode except for the straight beam model which is vibrating in the fundamental mode. Also, in contrast to other simulations discussed in chapter 3, the $Q_{surface}$ presented in table D.2 does include the ZY and ZX planes as well. As a frame of reference, the $Q_{surface}$ is 12000 when calculated using equation 2.9 and assuming the resonator takes on the dimensions of the straight beam model but without the channel and 11250 when calculated using equation 14 from Yasumura et al. which lets go of the simplification that the width far exceeds the thickness of the resonator. [25] This last part emphasizes the need for a somewhat more elaborate $Q_{surface}$ calculation due to the geometry of the resonator, even without taken the channel into account.

Generally, the $Q_{surface}$ that does not include the channel walls is quite comparable to the other $Q_{surface}$

	$Q_{surface}$ with channel surfaces	$Q_{surface}$ without channel surfaces
Straight beam model	8034	10050
Uniform unit cell model	9249	10701
Tapered beam model	10149	10207

Table D.2: This table compares the $Q_{surface}$ that include the channel walls and compares it with the $Q_{surface}$ that doesn't take the channel walls into account. The values are calculated using equation 2.13.

that does not include the channel walls, with a mean value of about 10500. The tapered beam has the lowest $Q_{surface}$ among the models that have phononic crystals. One possible explanation for this is that the channel itself only accounts for a relatively small part of the resonator due to the tapered nature of it. It also has the smallest difference with the $Q_{surface}$ that does include the channel walls. The uniform unit cell model has the lowest $Q_{surface}$ that includes the channel walls among the phononic crystal models. This can once again be explained because this model has the highest channel surface area compared to the overall resonator. The straight beam model has the lowest $Q_{surface}$ overall with a possible explanation being that the strain of this model could be higher as it is actuated in the fundamental eigenmode instead of the defect eigenmode.

Complete Qf product optimization results

	Total Q-factor [-]	Freq. [MHz]	Qf product [Hz]	E. mass [pg]	Mass sens. [$\frac{zg}{\sqrt{Hz}}$]
Tapered beam model, 1 um thick	3.88e6	1.56	6.1e12	1519	10.83
Tapered beam model, 200 nm thick	35.87e6	1.50	5.4e13	88.2	2.05
MDV model, 1 um thick	4.55e6	1.74	7.90e12	1563	3.91
MDV model, 200 nm thick	32.96e6	2.02	6.67e13	76.8	1.28
Uniform unit cell model	6.34e6	1.94	1.2e13	283.1	5.97
Manalis (2014) [37]	15000	2.89	4.3e10	92.3	9.49

Table D.3: A table of the optimization results of the Qf product. It lists the total Q-factor, resonance frequency, Qf product, effective mass and the mass sensitivity of the models that have been optimized.

	$Q_{surface}$	$Q_{mechanical}$	Q_{fluid}	Total Q-factor
Tapered beam model, 1 um thick	53306	4.21e6	5.03e7	3.88e6
Tapered beam model, 1 um thick w/o channel	57468	4.07e6	-	4.07e6
Tapered beam model, 200 nm thick	10067	36.02e6	8.48e9	35.87e6
Tapered beam model, 200 nm thick w/o channel	11317	47.42e6	-	47.42e6
MDV model, 1 um thick	56223	4.55e6	5.07e9	4.55e6
MDV model, 200 nm thick	10269	33.20e6	5.74e9	32.96e6
Uniform unit cell model	7719	6.40e6	7.61e8	6.34e6
Manalis (2014) [37]	-	-	6.8e5	15000

Table D.4: A table of the optimization results of the Qf product. It lists the different Q-factors of the models that have been optimized.

Other tables and figures

	Mech. Q-factor	Qfluid	Total Q-factor	Frequency [MHz]	Qf product
Channel scale = 0	4.559e6	5.117e9	4.555e6	1.74	7.94e12
Channel scale = 0.25	4.555e6	5.114e9	4.551e6	1.74	7.93e12
Channel scale = 0.5	4.545e6	5.084e9	4.541e6	1.74	7.90e12
Channel scale = 0.75	4.532e6	5.020e9	4.528e6	1.73	7.85e12
Channel scale =1	4.510e6	4.918e9	4.506e6	1.73	7.78e12

Table D.5: In this table the optimized MDV model of the Qf product was taken and only the design variable that scales the tapering of the channel was varied. The optimization result has scale = 0.44 for reference. It implies that the tapering of the channel doesn't change the Qf product by that much and that the selection of the specific value of the scaler by the optimization algorithm seems arbitrary.

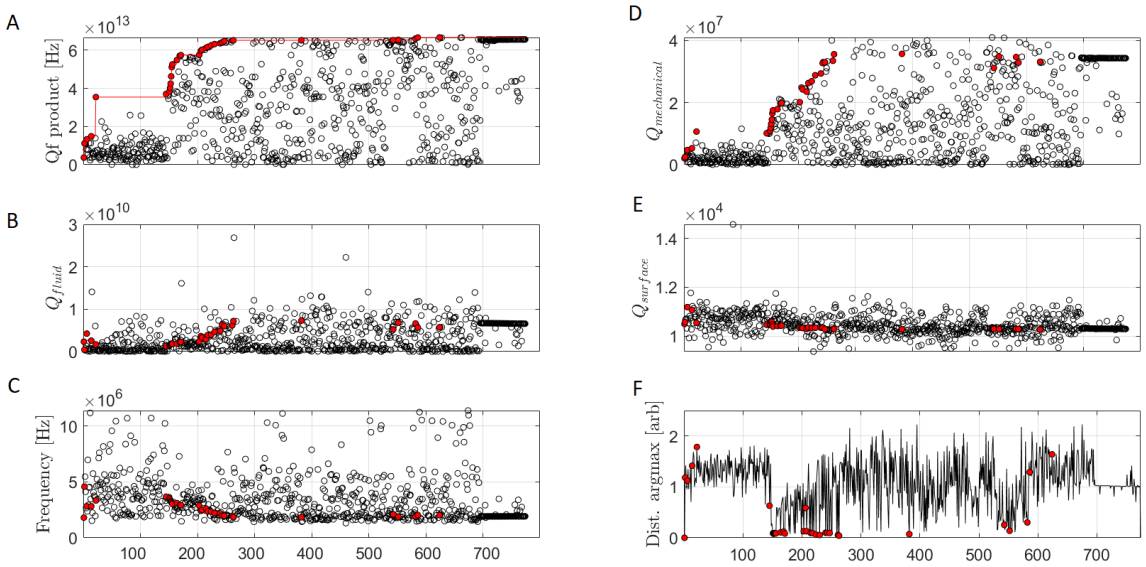

Figure D.1: A figure displaying the cross-sectional view of both the micrometer-sized model and the idealized model. Both models are tapered and the corresponding dimensions are included in the figure.

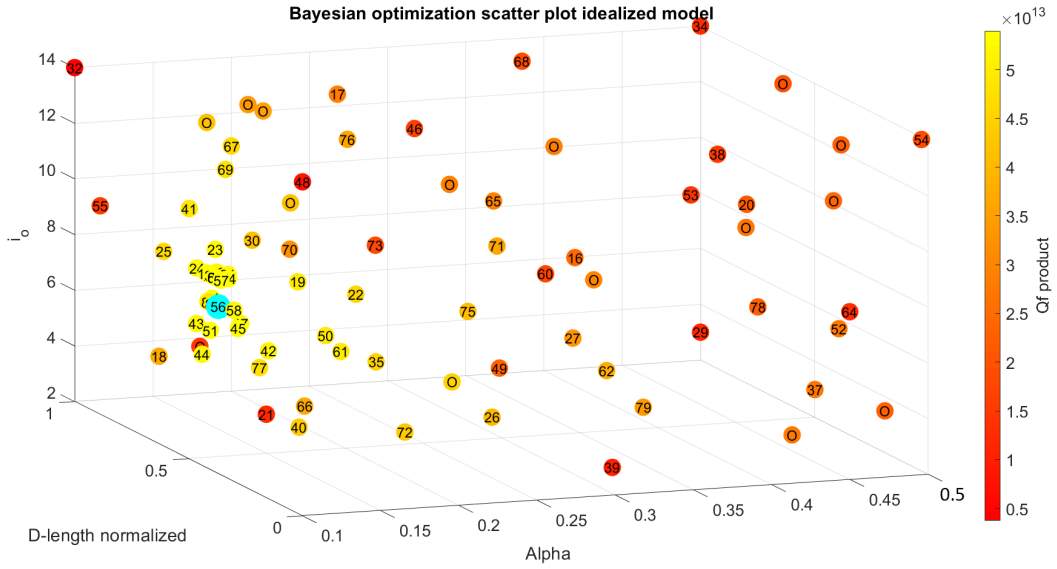

Figure D.2: A figure displaying the cross-sectional view of both the micrometer-sized model and the idealized model. Both models are tapered and the corresponding dimensions are included in the figure.

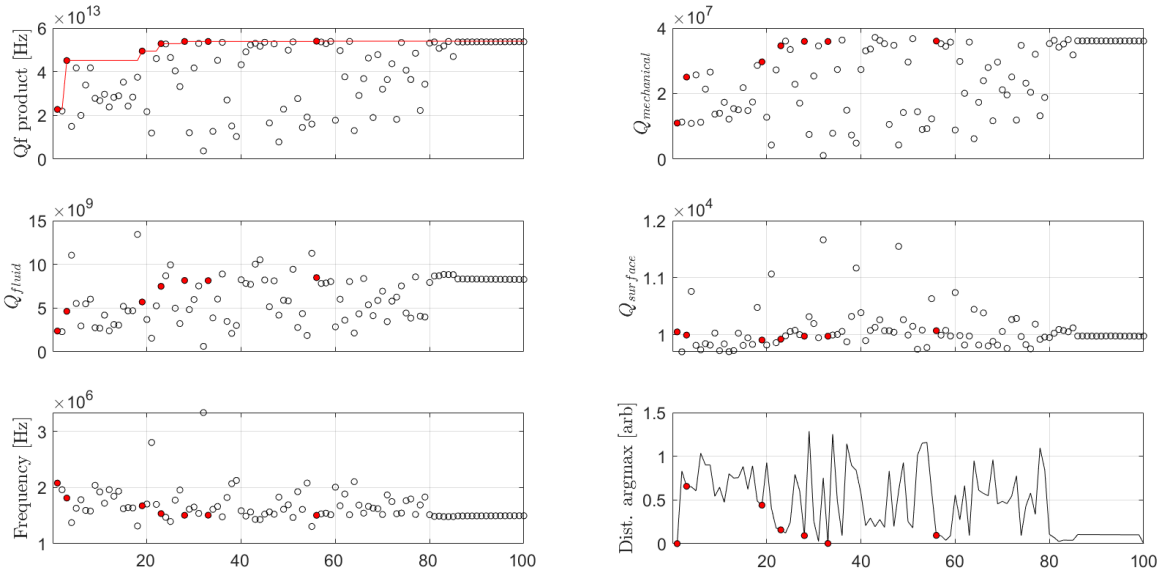

Figure D.3: A figure displaying the cross-sectional view of both the micrometer-sized model and the idealized model. Both models are tapered and the corresponding dimensions are included in the figure.

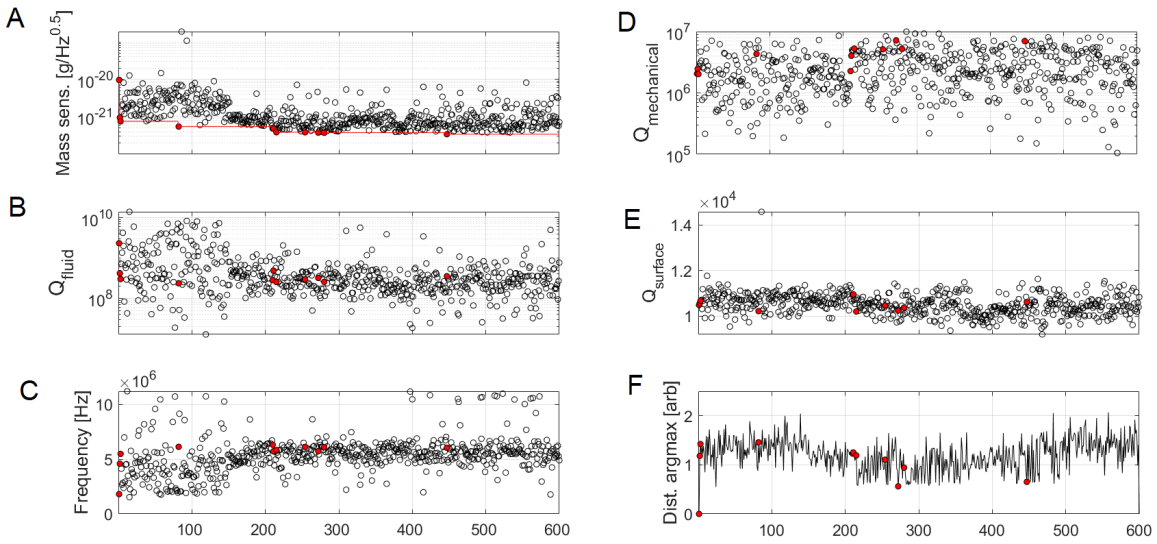

Figure D.4: A figure displaying the cross-sectional view of both the micrometer-sized model and the idealized model. Both models are tapered and the corresponding dimensions are included in the figure.

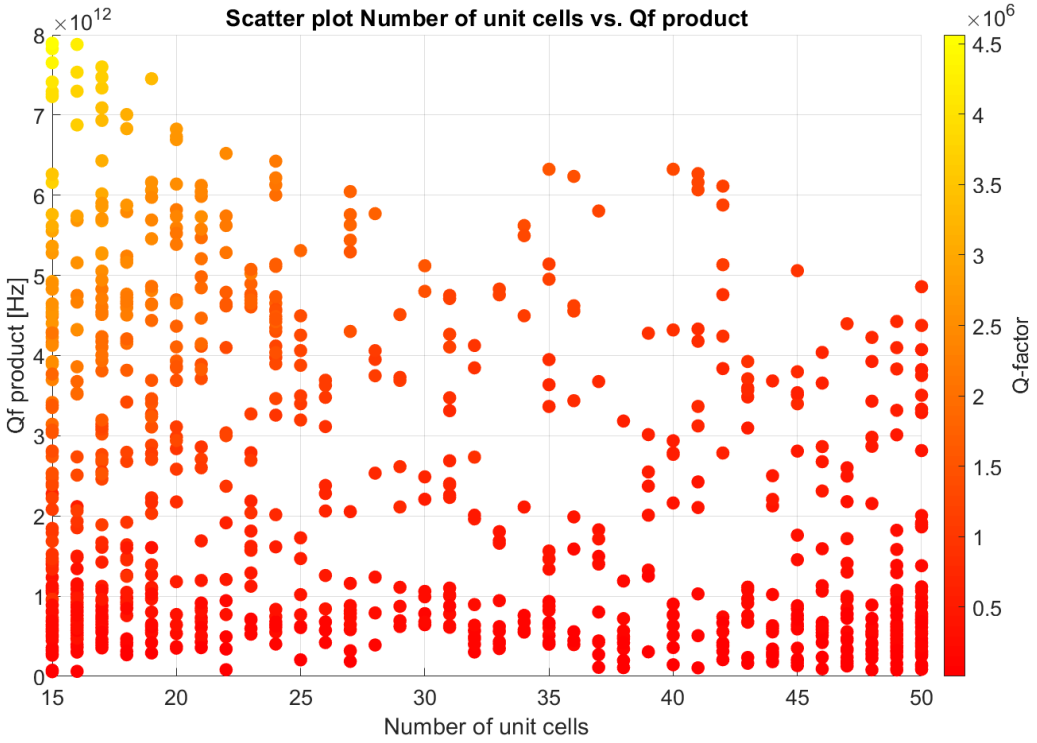

Figure D.5: A scatter plot of the number of unit cell vs. the Qf product. The color bar is the total Q-factor. As can be seen, it appears as if the maximum Qf product is located near the lower boundary with a drop off of Qf-product thereafter. The Q-factor also clearly tops here and drops to sub-million values for higher number of unit cells. It should be mentioned that these points are taken from the optimization results which could mean that in reality the drop off in Qf product could be less severe.

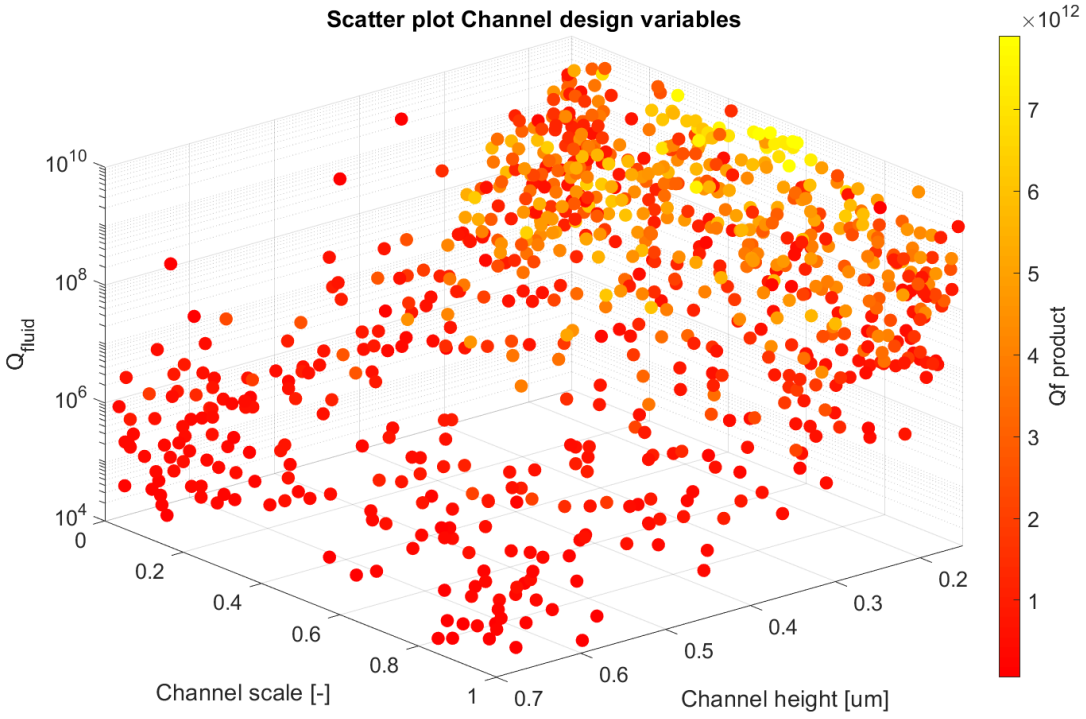

Figure D.6: A scatter plot of the design variables that impact the Qfluid the most. As can be seen there is a strong correlation between channel height and Qfluid.

Bibliography

[1] J. E. Sader, J. Lee, & S. R. Manalis. Energy dissipation in microfluidic beam resonators: Dependence on mode number. *Journal of applied physics*, 108(11):114507, 2010.

[2] J. E. Sader, T. P. Burg, J. Lee, & S. R. Manalis. Energy dissipation in microfluidic beam resonators: Effect of poisson's ratio. *Physical Review E*, 84(2):026304, 2011.

[3] R. A. Barton, B. Ilic, S. S. Verbridge, B. R. Cipriany, J. M. Parpia, & H. G. Craighead. Fabrication of a nanomechanical mass sensor containing a nanofluidic channel. *Nano letters*, 10(6):2058–2063, 2010.

[4] A. De Pastina & L. G. Villanueva. Suspended micro/nano channel resonators: a review. *Journal of Micromechanics and Microengineering*, 30(4), 2020.

[5] A. H. Ghadimi, S. A. Fedorov, N. J. Engelsen, M. J. Bereyhi, R. Schilling, D. J. Wilson & T. J. Kippenberg. Elastic strain engineering for ultralow mechanical dissipation. *Science*, 360(6390): 764–768, 2018.

[6] A. K. Naik, M. S.Hanay, W. K. Hiebert, X. L. Feng, & M. L. Roukes. Towards single-molecule nanomechanical mass spectrometry. *Nature nanotechnology*, 4(7):445–450, 2009.

[7] The GPyOpt authors. GPyOpt: A bayesian optimization framework in python. `http://github.com/SheffieldML/GPyOpt`, 2016.

[8] B. D. Hauer, C. Doolin, K. S. D. Beach, & J. P. Davis. A general procedure for thermomechanical calibration of nano/micro-mechanical resonators. *Annals of Physics*, 339:181–207, 2013.

[9] B. Shahriari, K. Swersky, Z. Wang, R. P. Adams & N. De Freitas. Taking the human out of the loop: A review of bayesian optimization. *Proceedings of the IEEE*, 104(1):148–175, 2015.

[10] B.N. Johnson, R. Mutharasan. Biosensing using dynamic-mode cantilever sensors: A review. *Biosensors and Bioelectronics*, 32:1–18, 2012.

[11] Encyclopædia Britannica. classes of antibodies, (accessed: July 27, 2021). URL `https://www.britannica.com/science/IgM#/media/1/282281/17661`.

[12] C. Reetz, R. Fischer, G.G.T. Assumpção, D.P. McNally, P.S. Burns, J.C. Sankey, & C.A. Regal. High quality factor resonance at room temperature with nanostrings under high tensile stress. *Journal of Applied Physics*, 99:124304, 2006.

[13] C. Reetz, R. Fischer, G.G.T. Assumpção, D.P. McNally, P.S. Burns, J.C. Sankey, & C.A. Regal. Analysis of membrane phononic crystals with wide band gaps and low-mass defects. *Physical Review Applied*, 12(4):044027, 2019.

[14] Wikipedia contributors. Hemoglobin, (accessed: July 27, 2021). URL `https://en.wikipedia.org/wiki/Hemoglobin`.

[15] Wikipedia contributors. Indiana vesiculovirus, (accessed: July 27, 2021). URL `https://en.wikipedia.org/wiki/Indiana_vesiculovirus`.

[16] E. Ventsel, T. Krauthammer, & E. J. A. M. R. Carrera . Thin plates and shells: theory, analysis, and applications. *Appl. Mech. Rev.*, 55(4):B72–B73, 2002.

[17] S. A. Fedorov, N. J. Engelsen, A. H. Ghadimi, M. J. Bereyhi, R. Schilling, D. J. Wilson, and T. J. Kippenberg. Generalized dissipation dilution in strained mechanical resonators. *Physical Review B*, 99(5):054107, 2019.

[18] P. I. Frazier. A tutorial on bayesian optimization. *arXiv preprint arXiv:1807.02811*, 2018.

[19] J. E. Sader, T. P. Burg & S. R. Manalis. Energy dissipation in microfluidic beam resonators. *Journal of Fluid Mechanics*, 650:215–250, 2010.

[20] J. Kim, J. Song, K. Kim, S. Kim, J. Song, N. Kim, M. F. Khan, L. Zhang, J. E. Sader, K. Park, D. Kim, T. Thundat, & J. Lee. Hollow microtube resonators via silicon self-assembly toward subattogram mass sensing applications. *Nano Letters*, 16(3):1537–1545, 2016.

[21] J. Lee, W. Shen, K. Payer, T. P. Burg & S. R. Manalis. Toward attogram mass measurements in solution with suspended nanochannel resonators. *Nano Letters*, 10(7):2537–2542, 2010.

[22] J. Snoek, H. Larochelle, & R. P. Adams. Practical bayesian optimization of machine learning algorithms. *Advances in neural information processing systems*, 25, 2012.

[23] J. Zhang, H. P. Lang, F. Huber, A. Bietsch, W. Grange, U. Certa, R. Mckendry, H. J. Güntherodt, M. Hegner & Ch. Gerber. Rapid and label-free nanomechanical detection of biomarker transcripts in human rna. *Nature Nanotechnology*, 1:214–220, 2006.

[24] K. L. Ekinci, Y. T. Yang, & M. L. Roukes. Ultimate limits to inertial mass sensing based upon nanoelectromechanical systems. *Journal of applied physics*, 95(5):2682–2689, 2004.

[25] K. Y. Yasumura, T. D. Stowe, E. M. Chow, T. Pfafman, T. W. Kenny, B. C. Stipe, & D. Rugar. Quality factors in micron-and submicron-thick cantilevers. *Journal of microelectromechanical systems*, 9 (1):117–125, 2000.

[26] L. G. Villanueva & S. Schmid. Evidence of surface loss as ubiquitous limiting damping mechanism in sin micro- and nanomechanical resonators. *Physical Review Letters*, 113(22):227201, 2014.

[27] J Lee, G Chen, W Shen, K Payer, TP Burg, W Rodriguez, M Toner, and SR Manalis. Weighing nanoparticles and viruses using suspended nanochannel resonators. In *2011 IEEE 24th International Conference on Micro Electro Mechanical Systems*, pages 992–994. IEEE, 2011.

[28] M. A. Stockslager, S. Olcum, S. M. Knudsen, R. J. Kimmerling, N. Cermak, K. R. Payer, V. Agache & S. R. Manalis. Rapid and high-precision sizing of single particles using parallel suspended microchannel resonator arrays and deconvolution. *Review of Scientific Instruments*, 90:085004, 2019.

[29] M. Aspelmeyer, T. J. Kippenberg & F. Marquardt. Cavity optomechanics. *Reviews of Modern Physics*, 86:1391–1452, 2014.

[30] M. Li, H. X. Tang & M. L. Roukes. Ultra-sensitive nems-based cantilevers for sensing, scanned probe and very high-frequency applications. *Nature Nanotechnology*, 2:114—120, 2007.

[31] M. Maldovan. Sound and heat revolutions in phononics. *Nature*, 503:209—217, 2013.

[32] M. S. Hanay, S. Kelber, A. K. Naik, D. Chi, S. Hentz, E. C. Bullard, & M. L Roukes. Single-protein nanomechanical mass spectrometry in real time. *Nature nanotechnology*, 7(9):602–608, 2012.

[33] P-L. Yu, T. P. Purdy, & C. A. Regal. Control of material damping in high-q membrane microresonators. *Physical review letters*, 108(8):083603, 2012.

[34] Q. P. Unterreithmeier, T. Faust & J. P. Kotthaus. Damping of nanomechanical resonators. *Physical Review Letters*, 105:1079–7114, 2010.

[35] C. E. Rasmussen. Gaussian processes in machine learning. In *Summer school on machine learning*, pages 63–71. Springer, 2003.

[36] S. E. Cross, Y. Jin, J. Rao & J. K. Gimzewski. Nanomechanical analysis of cells from cancer patients. *Nature Nanotechnology*, 2:780—783, 2007.

[37] S. Olcum, N. Cermak, S. C. Wasserman, K. Payer, W. Shen, J. Lee, & S. R. Manalis. Suspended nanochannel resonators at attogram precision. *2014 IEEE 27th International Conference on Micro Electro Mechanical Systems (MEMS)*, pages 116–119, 2014.

[38] L. G. Villanueva & M. L. Roukes S. Schmid. *Fundamentals of Nanomechanical Resonators*. Springer, 2016. 1st. ed.

[39] S. Schmid, K. D. Jensen, K. H. Nielsen & A. Boisen. Damping mechanisms in high-q micro and nanomechanical string resonators. *Physical Review B*, 84:165307, 2011.

[40] S. Surinova, R. Schiess, R. Hüttenhain, F. Cerciello, B. Wollscheid & R. Aebersold. On the development of plasma protein biomarkers. *Journal of proteome research*, 10(1):5–16, 2011.

[41] Pedram Sadeghi. *Study of High-Q Nanomechanical Silicon Nitride Resonators*. PhD thesis, Wien, 2021.

[42] D. Sarid. *Scanning Force Microscopy: With Applications to Electric, Magnetic, and Atomic Forces*. Oxford University Press, 1994. Revised edition.

[43] T. P. Burg, J. E. Sader & S. R. Manalis. Nonmonotonic energy dissipation in microfluidic resonators. *Physical Review Letters*, 102(22):228103, 2009.

[44] T. P. Burg, M. Godin, S. M. Knudsen, W. Shen, G. Carlson, J. S. Foster, K. Babcock & S. R. Manalis. Weighing of biomolecules, single cells and single nanoparticles in fluid. *Nature*, 446: 1066—1069, 2007.

[45] Y. Tsaturyan, A. Barg, E. S. Polzik & A. Schliesser. Ultracoherent nanomechanical resonators via soft clamping and dissipation dilution. *Nature Nanotechnology*, 12:776—783, 2017.